공학박사 학위논문

Synthesis of Copper-Based Nanomaterial for Conductive Electrode and Lithium Ion Battery Anodes

전도성 전극과 리튬이온 배터리용

구리 기반 나노 물질의 합성

2017년 8월

서울대학교 융합과학기술대학원

융합과학부 나노융합전공

조 상 훈

Synthesis of Copper-Based Nanomaterial for Conductive Electrode and Lithium Ion Battery Anodes

지도 교수 김 연 상

이 논문을 공학박사 학위논문으로 제출함
2017년 8월

서울대학교 융합과학기술대학원
융합과학부 나노융합전공
조 상 훈

조상훈의 공학박사 학위논문을 인준함
2017년 8월

위 원 장 박 원 철 (인)

부위원장 김 연 상 (인)

위 원 김 기 재 (인)

위 원 한 철 종 (인)

위 원 유 지 영 (인)

Abstract

Synthesis of Copper-Based Nanomaterial for Conductive Electrode and Lithium Ion Battery Anodes

Sanghun Cho
Program in Nano Science and Technology
Graduate School of Convergence Science & Technology
Seoul National University

Cu-based nanomaterial synthesis has been considered as the major issue due to its remarkable electrical, optical, catalytic, and electrochemical property. Over the past decade, various synthetic methods of Cu-based nanomaterial have been investigated for suitable applications. In particular, the synthesized copper-based nanomaterial has been widely applied to the use of conductive electrodes and lithium ion batteries, because of inherent

high conductivity, low cost, and high theoretical capacity. However, several limitations, such as complex manufacturing process, storage oxidation problem, and cracking problem during charge/discharge process, have hindered in the synthesis and application of Cu-based nanomaterial.

In this work, the study has primarily focused on a new simple synthetic method of Cu-based nanomaterial for enhanced application performance. Firstly, the Cu_3Sn alloy nanoparticles were introduced as good oxidation-resistance materials and conductive electrode using pressure-assisted fabrication method at room temperature. The Cu_3Sn nanoparticles showed the promising electrode properties such as oxidation-resistivity, low-cost materials, simple process-ability, and room temperature electrode fabrication-ability, as an electrode material. The electrical resistivity of the pressed Cu_3Sn nanoparticles electrode exhibited 19.8 μΩ·cm at 131.3 MPa. Secondly, novel self-reducible Cu-inks, composed by formate, alkanol amine groups and poly alcohols, were introduced for the air sinter-able fabrication of Cu electrode films. The proposed Cu-ink had a good self-reducible activity induced by the decomposition of Cu-ink ligand and the reduction assistance effect of the polyol solvents. This self-reducible ability of Cu-ink ensured the sintering of conductive Cu electrode film under air condition. The optimized properties of the sintered Cu electrode film made

using 3 wt% gCu-ink showed a resistivity of 17 μΩ • cm at a 350 ^{o}C air sintering temperature. Finally, synthesis of expanded graphite/Cu oxide nanoparticle composite (GCuO) was introduced to increase energy density and stability of lithium-ion batteries. GCuO was prepared by thermal treat treatment of a Cu ion complex and graphite. In this process, gasses (H_2 and CO_2) generated from the thermal decomposition of the Cu ion complex decomposition, which induced Cu oxide nanoparticle formation and graphite interlayer expansion (from 0.34 to 0.40 nm). The GCuO has good potential for effective Li ion intercalation into anodes for next generation batteries. The electrochemical properties of GCuO were determined using Li ion cells. GCuO cells exhibited a high energy density (263 Wh kg^{-1}), discharging capacity (532 mA h g^{-1} at 0.2 C), rate retention capability (from 0.2 to 10 C), and stable long-term cycle-ability (83% capacity retention after 250 cycles).

Keywords: Copper based nanomaterial, Cu alloy, Cu oxide, Nanomaterial synthesis, Conductive electrode, Lithium ion battery anode.

Student Number: 2012-22452

Contents

List of figures

nanoparticles. (e) Vis−NIR (near-infrared) extinction spectra of the Cu NPs dissolved in toluene (inset). (Reprinted with permission from Ref. [14] of Chapter 1,2)

Figure 2.2 Cu_2O nanocrystal SEM image of (a) cubic, (b) octahedral, and (c) rhombic dodecahedral. The scale bars indicate 1μm. Crystal structure models of Cu_2O, showing the (d) {100}, (e) {111}, and (f) {110} surfaces. The oxygen atoms are dark gray sphere and Cu atoms are shown in white sphere. (Reprinted with permission from Ref. [18] of Chapter 1,2)

Figure 2.3 Various approaches for the synthesis of Cu-based nanomaterial. These methods are divided by electrochemical, photochemical, thermal treatment, sonochemical, and chemical treatment. (abbreviations : MW = microwave, CVD = chemical vapor deposition, ALD = atomic layer deposition, IL = ionic liquid, and DBD = dielectric battery discharge) (Reprinted with permission from Ref. [6],[7],[10],[11] of Chapter 1,2)

Figure 2.4 (a) SEM image of the Cu nanoparticles, (b) Powder XRD spectra using PVP capping agents, (c) TEM image and (d)

selected area electron diffraction (SAED) pattern of Cu nanoparticle in the presence of dodecylamine/oleic acid as surfactant (Reprinted with permission from Ref. [31],[32] of Chapter 1,2)

Figure 2.5 Cu_2O nanostructure syntheses (a) SEM image and (b) XRD results of different shape nanocrystals (plate, wire, particles, etc,.) (Reprinted with permission from Ref. [33] of Chapter 1,2)

Figure 2.6 Schematic illustration of the synthetic procedure for the Cu_2O nanoparticles using heat decomposition method. After formation of Cu nanoparticles, subsequent oxidation makes Cu_2O nanoparticles under air at room temperature. (Reprinted with permission from Ref. [34] of Chapter 1,2)

Figure 2.7 Synthesis of CuO nanoparticles using water in oil reverse micelles. (a) XRD patterns of CuO nanoparticles, (b), (c) TEM images and size distribution of nanoparticles depending on molar ration of water to surfactant. (Reprinted with permission from Ref. [35] of Chapter 1,2)

Figure 2.8 (a) TEM and (b) High Resolution TEM images of 15 nm Cu_2O

Figure 2.12 (a) Schematic illustration for the formation mechanism of triangular and hexgonal Ni-Cu alloy nanoparticles. TEM image of synthesized Ni-Cu alloy nanoparticles at different temperatures (b) 220 ^{o}C, and (c) 240 ^{o}C. Scanning TEM – energy dispersive X-ray spectroscopy (EDS) image for (d) Ni and (e) Cu. (Reprinted with permission from Ref. [45] of Chapter 1,2)

Figure 2.13 (a) Growth mechanism of Ag@Cu using polyol methods. Ag-Cu bimetallic particles prepared from Ag precursor ($AgNO_3$) and $Cu(OAc)_2$ in presense of PVP and EG mixture. In molar ratio of 0.25 [Ag]/[Cu], the bimetallic particles are investigated by (b) TEM, and EDS elemetnal maps for (c) overall, (d) Ag, and (d) Cu. (Reprinted with permission from Ref. [46] of Chapter 1,2)

Figure 2.14 Characteristics of alloy nanoparticles. (a) TEM image of $AuCu_3$ nanoparticles with average size of 11.2 nm, (b) XRD results of Au-Cu alloy nanoparticles by atomic composition, (c) UV-vis spectra of Au-Cu alloy nanoparticles, (d) Pd-Cu nanoparticles (ratio of Cu/Pd 1:5)TEM images, and (e) XRD patterns of Pd-Cu alloy nanoparticles by composition. (Reprinted with permission from Ref. [47],[48] of Chapter 1,2)

Figure 2.15 (a) Schematic illustration of the Cu@Ag nanoparticles synthetic method. (b) Elemental profile and (c) STEM image of Cu@Ag nanoparticles, (d) The resistivity by sintered Cu@Ag nanoparticles. (Reprinted with permission from Ref. [57] of Chapter 1,2)

Figure 2.16 Photograph of (a) the Cu ion complex ink, (b) the letter of before and after sintering, (c) Electrical resistivity of Cu conductive film using Cu ion complex ink. (Reprinted with permission from Ref. [59] of Chapter 1,2)

Figure 2.17 (a) Schematic representation of the Cu nanoparticles ink synthetic method and IPL sintering process for conductive film fabrication, (b), (c), and (d) SEM topographical image of IPL treated film with energy input increasing from 576 J cm^{-2} to 1723 J cm^{-2}. (Reprinted with permission from Ref. [60] of Chapter 1,2)

Figure 2.18 Schematic illustration of lithium ion battery charge/discharge principle. (Reprinted with permission from Ref. [66] of Chapter 1,2)

Figure 2.19 Classification of oxide anode material; Intercalation-deintercalation, alloying-dealloying, and conversion reaction.

(Reprinted with permission from Ref. [68] of Chapter 1,2)

Figure 2.20 (a) SEM image of 150 nm size Cu_2O particles, (b) Voltage profile of Cu_2O/Li cell, and (c) long term cycling stability. (Sample A is 150 nm and Sample B is 1 μ m) [73] (d) CuO hollow nanospheres SEM image, (e) Charge-discharge curves and (f) Cyclic voltammogram of CuO/Li cell in range of 0.01 – 3.0 V. The inset is the cycling performance. (Reprinted with permission from Ref. [72],[74] of Chapter 1,2)

Figure 2.21 TEM image of (a) CuO nanoparticles (b) CuO/CNT nanocomposite using porous $Cu(OH)_2$ chemical transformation and CNT blending, (c) Voltage profile of the CuO/CNT nanocomposite, (d) Long term cycling stability, comparing with CuO/CNT and CuO/C blending electrode. (Reprinted with permission from Ref. [77] of Chapter 1,2)

Figure 3.1 (a) TEM image of the synthesized Cu_3Sn nanoparticles with an average size of 60nm (b) XRD data of synthesized Cu_3Sn nanoparticles compared with Cu_3Sn reference peak (JCPDS 03-1010) (c) EDS spectrum of Cu_3Sn nanoparticles with Cu:Sn at

76.67 : 23.33 (d) The HAADF-STEM image and EDS mapping images of the Cu-Sn alloy (Cu_3Sn) nanoparticles.

Figure 3.2 (a) Schematic of pressure-assisted Cu_3Sn nanoparticle electrodes fabrication. (b) I-V curve of Cu_3Sn nanoparticles electrodes at a 131.3 MPa pressure condition, which correspond with conventional ohmic contact electron transport (c) Cross-sectional TEM images of pressed Cu_3Sn nanoparticle electrodes at 131.3 MPa pressure condition. (d) The enlarged cross-sectional TEM view of pressed Cu_3Sn nanoparticles. (e) TEM-EELS elemental mapping that show the carbon (white) elements.

Figure 3.3 A typical EELS spectrum (a) carbon reference, (b) carbon spectrum of the pressed Cu_3Sn alloy nanoparticles, corresponding TEM-EELS elemental map (Figure 3.2e)

Figure 3.4 (a) Electrical resistivity of the pressed Cu_3Sn nanoparticles electrode as a function of pressure. The Cu_3Sn nanoparticles electrodes were fabricated at various pressures ranging from 39.4 MPa to 170.7 MPa. (b) Electrical resistivity of the pressed Cu_3Sn nanoparticles electrodes with varying bend radius, and a bending

measurement image (inset). Optical images of the Cu_3Sn nanoparticles electrode pattern in a (c) flat state and (d) bent state.

Figure 3.5 (a) Plane view SEM and (b) cross section SEM images of the pressed Cu_3Sn nanoparticles. The thickness of the pressed Cu_3Sn nanoparticles electrode is ~ 89 μm in 65.6 MPa.

Figure 3.6 (a) XRD patterns of the synthesized Cu_3Sn alloy nanoparticles; just fabricated and stored in ambient air conditions (RH 50%, 25 ^oC) for 4 weeks (b) The resistivity variation of the electrodes fabricated by pressured Cu_3Sn alloy nanoparticles corresponding to the stored time in ambient air conditions

Figure 3.7 HR-TEM image of Cu_3Sn alloy nanoparticles and the red line indicate the oxide layer and the oxide layer thickness is measured to 1.5nm

Figure 3.8 EDS analysis of (a) just synthesized Cu_3Sn alloy nanoparticles and (b) stored in ambient air condition (RH 50%, 25 ^oC) for 4 weeks The SAED pattern analysis of the Cu_3Sn alloy

List of schemes

List of tables

Chapter 1. Introduction

1.1 Background on the nanomaterial

The typical definition of nanomaterials is size range of 1 -100 nm and dimension number from zero dimension (0-D) to three dimensions (3D). As the effect of a small size and type of dimension, the nanomaterials exhibit unique property, like chemical, mechanical, biological, electronic, and optical, that is different from bulk property.[1] These remarkable properties of nanomaterials make it possible to apply interesting applications. In particular, among various nanomaterials, the noble metal nanomaterials (Au, Ag, Pt, etc.) have emerged as attractive nanomaterials due to their facile synthetic method, shape control availability, well-known crystal structure, and highly stable property. From the unique characteristics, the noble metal nanomaterials have been developed for multi-functional applications in the field of sensor, catalyst, imaging, and optics.[2],[3],[4],[5] (Figure 1.1)

The initial stage of nanomaterial studies has focused on these noble metal

application and synthetic method for uniform size, shape control. However, the researchers gradually realize that the noble metal nanoparticles do not satisfy the increasing new requirement of the complex application. For this reason, various types of nanomaterial, such as metallic nanoparticle (Cu, Fe, Ni, Co, etc.) and multi-composition (intermetallic alloy, core-shell, hetero-structure), are investigated for better performance.[6],[7] (Figure 1.2) For example, the core-shell structure of CdSe-ZnS and the metal oxide nanoparticles of Fe_3O_4 are proposed for stable luminescence and efficient magnetic property, respectively.[8],[9]

Especially, the research of Cu-based nanomaterial synthesis and application is fascinating, because of high natural abundance, low cost, and practical usefulness (e.g. catalyst, optics, electronics, etc.) of Cu-based nanomaterial.[10] (Figure 1.2) In addition, Cu nanomaterial can create the wide range of oxidation states (e.g., Cu, CuO, or Cu_2O) and Cu alloy phase with variety transition metal (e.g., Cu-Sn, Cu-Ni, and Cu-Zn).[11] These Cu-based nanomaterials have some advantages; (1) the new functionalities of alloy or oxide components, (2) complementation of individual material disadvantage, and (3) the maximization of material characteristics. However, despite these many advantages of Cu-based nanomaterials, the synthetic method complexity and intrinsic property of Cu, like as unintended

oxidation under atmospheric conditions, make it difficult to use practical application.[12]

In this dissertation, I focus on the newly designed Cu-based nanomaterial synthetic method and application. It will be effectively addressed for high conductive electrode and high capacity and stable Lithium-ion battery (LIB) anode. To begin with, the next chapter provides the general introduction to the Cu-based nanomaterial characteristic, synthetic method, application, and the research themes.

1.2 Dissertation overview

This dissertation composes seven chapters; the characteristics, synthetic approach, and related application introduction of Cu-based nanomaterials are offered in chapter 2. It offers an insight into the crystal structure, materials property, and synthetic method of pure Cu metal, Cu-based alloy, and Cu Oxide nanomaterial. In addition, as related application introduction, the conductive electrode and LIB anode will be covered with advantages, research issue, and aiming behind this thesis. In the chapter 3, synthesis of Cu_3Sn alloy nanoparticles using pressure assisted electrode fabrication method, which was proposed as alternative Cu electrode oxidation

limitation. To identify structure and property of synthesized Cu_3Sn alloy nanoparticles, the High-Resolution Transmission Electron Microscopy (HR-TEM), energy dispersive spectrometer (EDS) and X-ray diffraction (XRD) were conducted. The electrical resistivity of the pressed Cu_3Sn nanoparticle electrode was 19.8 μΩ cm at 131.3 MPa. In addition, the synthesized Cu_3Sn alloy nanoparticles did not change the electric resistivity during 4 weeks under ambient conditions.

In chapter 4, self-reducible copper ion complex ink (Cu-ink) is proposed for air sinter-able Cu conductive electrodes. The self-reducible Cu-ink, composed by formate, alkanolamine groups and poly alcohols, was fabricated for the air sinter-able, low-cost, and high conducvtive Cu electrodes. As reduction assistant-material, glycerol was found to be the most suitable materials because of its relatively abundant hydroxyl groups, good evaporation properties. As a result, the prepared Cu electrode films showed a low resistivity of 17 μΩ cm at 350 °C under air sintering conditions.

In chapter 5, expanded graphite with Cu oxide nanoparticles was introduced for high stable and capacity LIB anode. Novel expanded graphite with copper oxide (GCuO) was made by thermal decomposition of Cu ion complex and graphite composites. The carbon layer expanding of

graphite was induced by the self-generated gas (H_2 and CO_2) of the Cu ion complex decomposition. In addition, the Cu oxide nanoparticles were formed by reduction property of the Cu ion complex. Through investigations of materials analysis and electrochemical test, graphite carbon layer expanding phenomenon (from 0.34 nm to 0.40 nm) and outstanding LIB half-cell performance (high capacity of 532 mAh g^{-1} at 0.2 C and retention property of 83 % after 250 cycles) was founded.

Finally, the overall research results related to Cu-based nanomaterials synthesis and application are summarized in chapter 6. Moreover, new designed Cu-based nanomaterials synthesis for improved application is described.

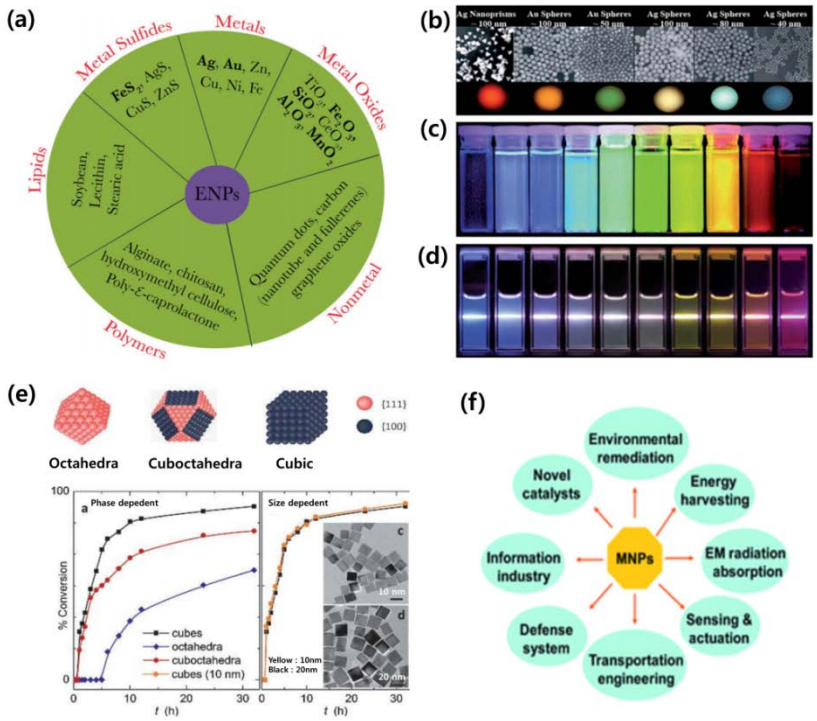

Figure 1.1 (a) Representative types of Nanomaterials [2] Multicolor tuned nanomaterial; (b) Noble metal nanoparticles with different size and shape[3], (c) Size-dependent emission of ZnS-CdSe nanoparticles [3], (d) Upconversion emission of lanthanide doped $NaYF_4$ nanoparticles[3], (e) Catalytic reaction (Suzuki - Miyaura reaction) of Pd nanocrystal depending phase and size[4], and (f) Application of nanoparticles with various fields.[5] (Reprinted with permission from Ref. [3],[4],[5] of Chapter 1,2)

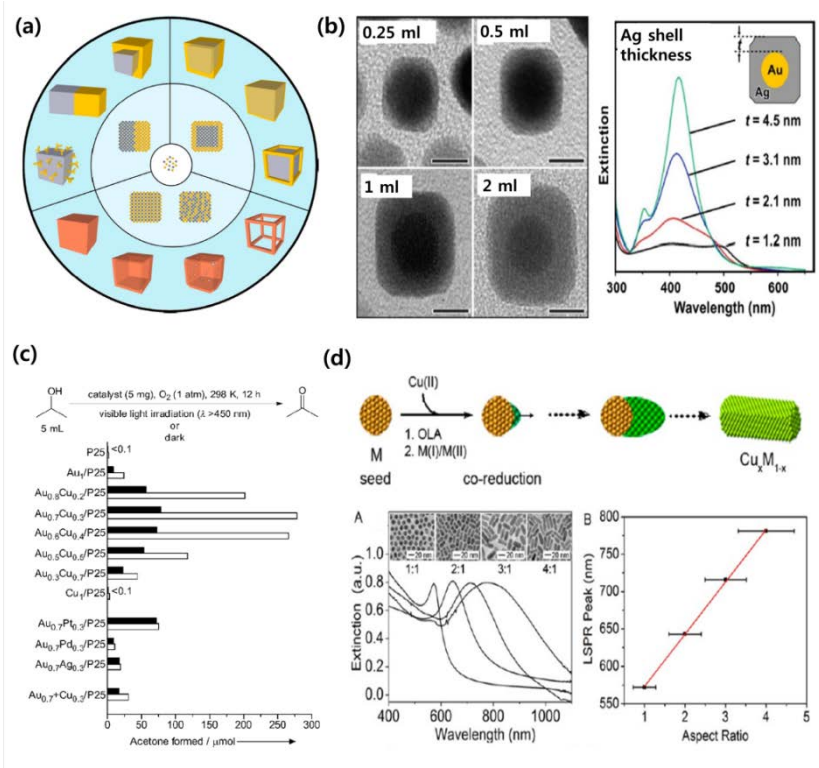

Figure 1.2 (a) Many different possible types or morphologies of the hybrid nanoparticle.[6] (b) Catalytic reaction of Au@Ag core-shell by injecting a different volume of $AgNO_3$.[7] The example of Cu-based nanomaterial; (c) Acetone forming catalytic reaction of Au_xCu_y[10], and (d) Schematic illustration of bimetallic Cu-based nanorods, NIR spectra, and LSPR peak plot as the function of Cu-Au nanorods aspect ratio. [11] (Reprinted with permission from Ref. [6],[7],[10],[11] of Chapter 1,2)

Chapter 2 Fundamentals and Literature Review

2.1 Cu and Cu oxide nanomaterials

2.1.1 Characteristics of pure Cu and Cu oxide nanomaterials

From ancient times, copper (Cu) is considerable attractive materials, due to easy moldability and formation to alloy with another metal. Cu is basically a reddish-brown element with bright glossy metallic materials. The intrinsic property of Cu is soft, malleable and high ductile. In chemically, it slowly reacts with atmospheric oxygen to form a copper oxide layer. In terms of electron configuration ($[Ar].3d^{10}.\ 4s^{1}$), it has one free electron in the outermost shell, which induce the high conductivity. The structure of copper is face centered cubic (FCC) system, with possible crystal morphologies of cubic {100}, octahedral {111}, dodecahedral {110}, tetrahexahedral {530}. In addition, it is inexpensive materials as 26^{th} most abundant element. (Figure 2.1)

Recently, according to nano science development, Cu nanomaterial, including Cu nanoparticle, nanowire, has focused on various fields with similar to bulk Cu application.[13],[14] The Cu nanomaterial has unique property by their different size and shape. First, the Cu nanomaterial has localized surface plasmon resonance (LSPR), which occurs in the visible range for copper metal nanoparticles. This unique optical property has a possibility for disease diagnostic and biological sensing.[15] Second, the catalytic reactions of Cu nanomaterial exhibit remarkable property for diverse reaction, including photo catalysis, gas-phase reaction, electro-catalysis, and coupling reactions.[16] Finally, high conductivity is shown as the electrical property of Cu nanomaterial. The intrinsic high conductivity has a significant impact for the future printing electronics.[17]

As mentioned above, the Cu nanomaterial chemically reacts with oxygen under the atmosphere, which can promote variety reaction due to its wide range oxidation states (Cu^0, Cu^I, and Cu^{II},). The properties of cuprous oxide (Cu_2O) and cupric oxide (CuO) exhibit considerable different from pure Cu nanomaterial. Most basically, the crystal structures of Cu_2O and CuO are proved as cubic and monoclinic structures, respectively.[18] (Figure 2.2) For this reason, Cu_2O and CuO nanomaterial studies have also been conducted on various fields. As various properties, the electrical characteristics of

Cu_2O and CuO exhibit p-type metal oxide semiconductor, which is a prospective candidate for solar energy conversion and photo-catalysis.[19] Both are semiconductors with band gaps of 2.0 eV and 1.2 eV, respectively. These materials also have electrochemically conversion reaction with hydrogen ion or lithium ion. As electrode materials for lithium ion battery or supercapacitor, it is being actively studied.[20], [21], [22] Furthermore, characteristics of catalysis could be utilized using the specific phases of copper oxide nanomaterial.[23]

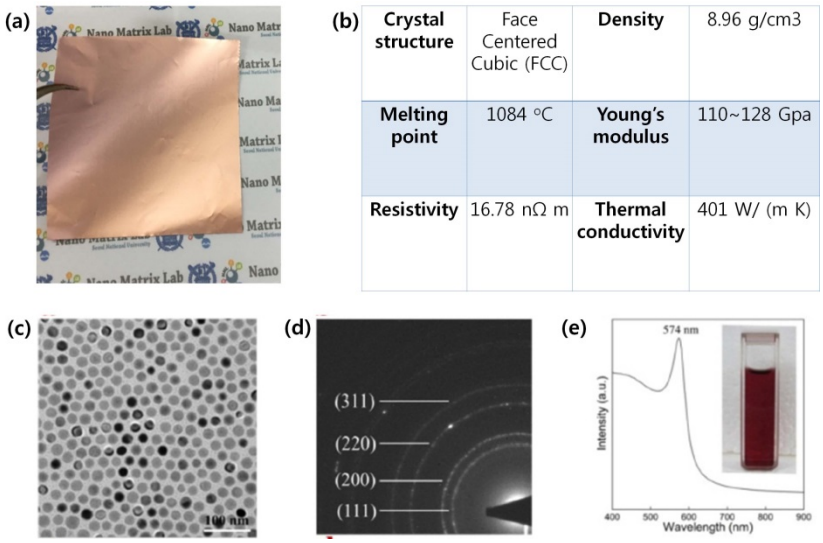

Figure 2.1 (a), (b) Photograph and physical property table of bulk Cu (image from https://ferrebeekeeper.wordpress.com/tag/commodity/) (c) Representative TEM image (d) SAED pattern of synthesized Cu nanoparticles. (e) Vis−NIR (near-infrared) extinction spectra of the Cu NPs dissolved in toluene (inset).[14] (Reprinted with permission from Ref. [14] of Chapter 1,2)

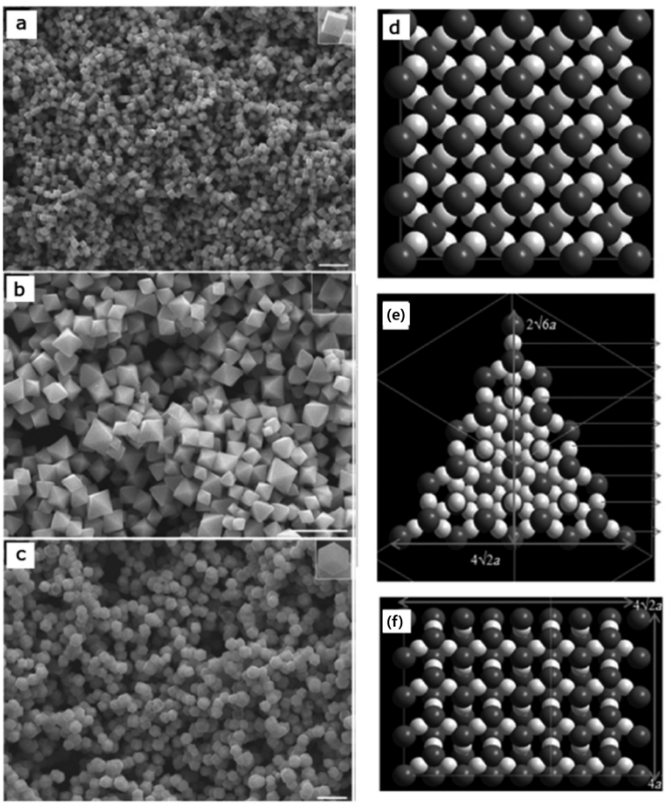

Figure 2.2 Cu_2O nanocrystal SEM image of (a) cubic, (b) octahedral, and (c) rhombic dodecahedral. The scale bars indicate 1 μm. Crystal structure models of Cu_2O, showing the (d) {100}, (e) {111}, and (f) {110} surfaces. The oxygen atoms are dark gray sphere and Cu atoms are shown in the white sphere.[18] (Reprinted with permission from Ref. [18] of Chapter 1,2)

2.1.2 Synthesis method for Cu and Cu oxide nanomaterial

The preparation of pure copper and copper oxide nanomaterial is proposed as several methods such as photochemical, electrochemical, sonochemical, physical deposition, and sputtering.[16],[24] (Figure 2.3) These methods are divided by either “bottom-up” (ionic precursors are reduced to nanosized materials) or “top-down” (bulk solid materials are broken down into smaller size materials). In general, the “bottom-up” approach has become the more preferred method, because it is easy to controls the shape and size of nanomaterial. Among the “bottom-up” methods, wet chemical reduction technique is the most established approach in order to synthesize the metallic Cu nanomaterials and Cu oxide nanomaterial. This method is based on the reduction of the Cu salts, such as Cu (Ⅱ) sulfate, Cu (Ⅱ) chloride, to Cu and Cu oxide nanomaterial. In addition, to stable particle formation and reduction, reduction agents (sodium borohydride ($NaBH_4$), hydrazine (N_2H_2), ascorbic acid, or organic compound with amine group) and various organic capping agents (polyvinylpyrrolidone (PVP), cetrimonium bromide (CTAB), and polyethylene oxide (PEO)) have been used. During the past decades, these wet chemical reduction synthesis has

been proposed due to its facility of synthesis and shape control.

Along the reduction method and capping method, it is classified once again such as polyol reduction method, thermal decomposition method, and reverse micelle synthesis. The polyol reduction method uses the multiple hydroxyl functional groups, possessing reducing ability, such as glycerin, ethylene glycol (EG), and polyethylene glycol.[25], [26] The main points of the polyol method are both role of reduction agents and solvents of polyol solvents. Additionally, the polyol stabilizes the particles surface, which induces the particle aggregation and unexpected crystal growth. As another method, the thermal decomposition method is proposed for various nanomaterial synthesis.[27],[28] It is based on organometallic compounds and metal – functional group complex. The organometallic complex acts a capping agent and reduction agents by functional group (such as amine, carboxylic acid, etc.). This multifunction of organometallic compound assists facile shape and size control of nanomaterial. In addition, the high temperature, which is applied to decompose the organometallic compound, makes it possible to form the high crystallinity and mono-dispersed nanoparticles. Finally, the reverse micelle method involves the formation of oil in water (O/W) microemulsion.[29],[30] The adding of surfactant, composed by immiscible polar and nonpolar reaction group, makes the

microemulsion (micelle) in the solvent. Such reverse micelles support the uniform size nanoreactors for nanomaterial production that enable to control shape and size. In this chapter, Cu and Cu oxide nanomaterial synthesis research using these wet chemical reduction method and issue will be introduced.

The wet chemical reduction method is the most common method for producing Cu and Cu oxide nanoparticles. In principle, this approach is based on the reduction of Cu ion salts. However, it is difficult to synthesis the pure Cu nanomaterial by the Cu ions reduction because Cu nanomaterial can be easily oxidized to Cu_2O or CuO. As a result, the synthesis of pure copper nanomaterial usually requires specific air condition, which is vacuum, reducing environment (H_2, formic acid), or ambient gas condition (N_2). Park *et al.* reported the synthesis of pure Cu nanoparticles using PVP as the capping agent and oxidation stabilizer.[31] (Figure 2.4) As another example, Aissa *et al.* presented copper chloride reduction process for the synthesis of copper nanoparticles through the reduction reaction of tert-butylamine borane in the presence of dodecylamine/oleic acid as surfactant. [32] (Figure 2.4) These Cu nanoparticles are equally prepared in ambient condition, strong reduction agents, and oxidation preventing capping agents, which made it possible to make oxidation stable Cu nanomaterial.

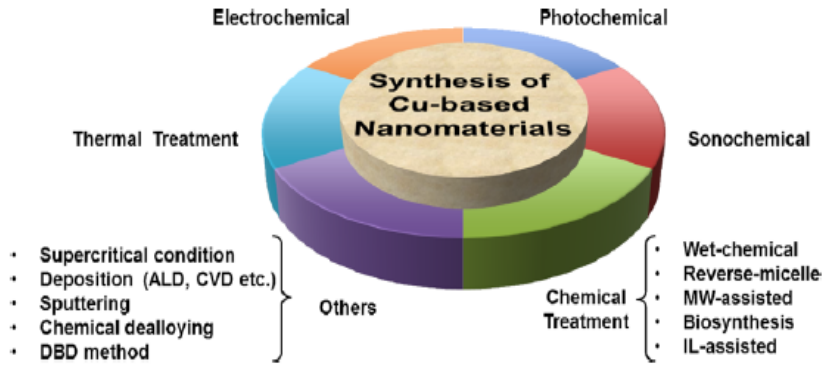

Figure 2.3 Various approaches for the synthesis of Cu-based nanomaterial. These methods are divided by electrochemical, photochemical, thermal treatment, sonochemical, and chemical treatment. (Abbreviations: MW = microwave, CVD = chemical vapor deposition, ALD = atomic layer deposition, IL = ionic liquid, and DBD = dielectric battery discharge)[16]

(Reprinted with permission from Ref. [6],[7],[10],[11] of Chapter 1,2)

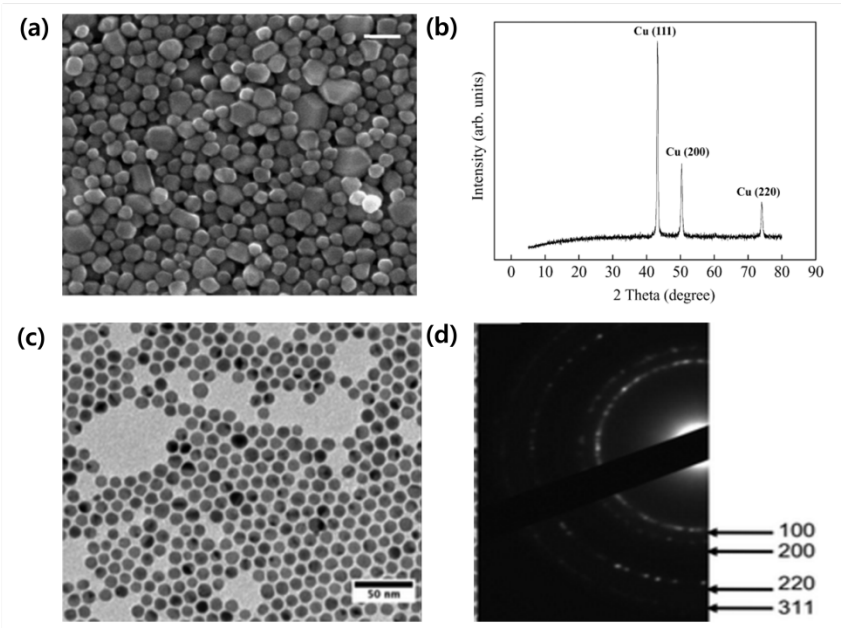

Figure 2.4 (a) SEM image of the Cu nanoparticles, (b) Powder XRD spectra using PVP capping agents [31] (c) TEM image and (d) selected area electron diffraction (SAED) pattern of Cu nanoparticle in the presence of dodecylamine/oleic acid as surfactant [32] (Reprinted with permission from Ref. [31],[32] of Chapter 1,2)

On the other hand, the Cu oxide nanomaterial demands the mild condition for synthesis. For example, low temperature treatment, oxygen exposed reaction, and mild reduction agent (ascorbic acid, glucose, oleylamine) were studied using wet chemical reduction method. In addition, characteristics of intrinsic Cu oxide crystal growth enable it to form the different morphology, which induces the enhanced performance of its application. Sabbaghan, M. *et al.* reported the different morphology of Cu_2O by glucose with mild reduction. The particles shape, such as octahedral, nanorod, and nanoparticle, is adjusted by a concentration of glucose and this method also obtained small size (18-32 nm) product.[33] (Figure 2.5) As another example, O'Brien *et al.* developed a method by the thermal decomposition of copper salt - amine complex to control the nano size between 3.6 and 10.7 nm and synthesize monodispersed Cu_2O spheres. The pure Cu nanoparticles were formed by heat treatment and decomposition of copper (I) acetate, trioctylamine, and oleic acid at 270 ^{o}C. After the formation of Cu nanoparticles, subsequent oxidation of these pure Cu nanoparticles obtained Cu_2O nanoparticles under air at room temperature.[34] (Figure 2.6) Another efficient method to prepare Cu oxide nanomaterials is reverse micelle method. D. Han *et al.* showed the preparation of CuO nanoparticles *via* TritonX-100 based water-in-oil

reverse micelles. In this report, the water-in-oil reverse micelles are strongly connected to a molar ratio of water to surfactant. These reverse micelles methods provide a useful route to the synthesis of CuO nanoparticle different morphologies and size distribution. (Figure 2.7) [35]

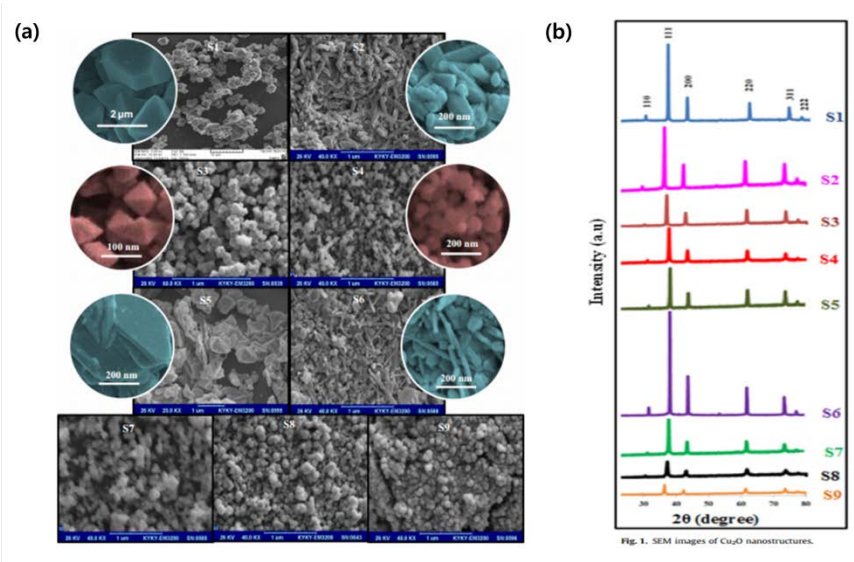

Figure 2.5 Cu_2O nanostructure syntheses (a) SEM image and (b) XRD results of different shape nanocrystals (plate, wire, particles, etc,.) [33]

(Reprinted with permission from Ref. [33] of Chapter 1,2)

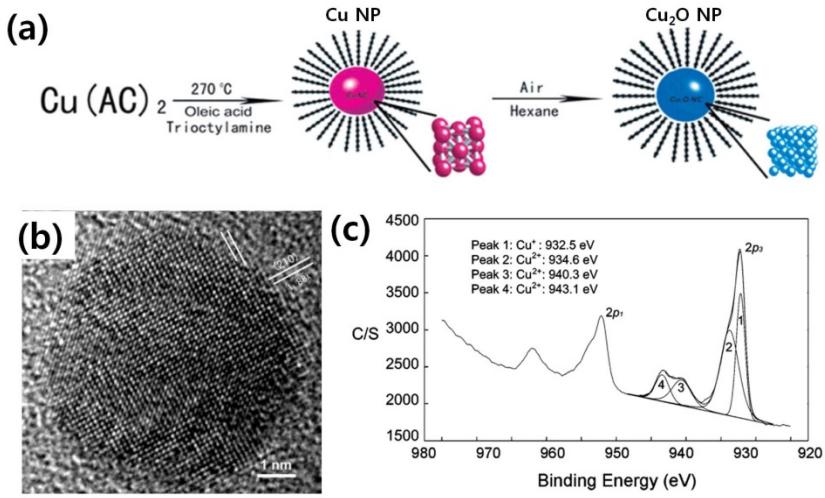

Figure 2.6 Schematic illustration of the synthetic procedure for the Cu_2O nanoparticles using heat decomposition method. After formation of Cu nanoparticles, subsequent oxidation makes Cu_2O nanoparticles under air at room temperature. [34] (Reprinted with permission from Ref. [34] of Chapter 1,2)

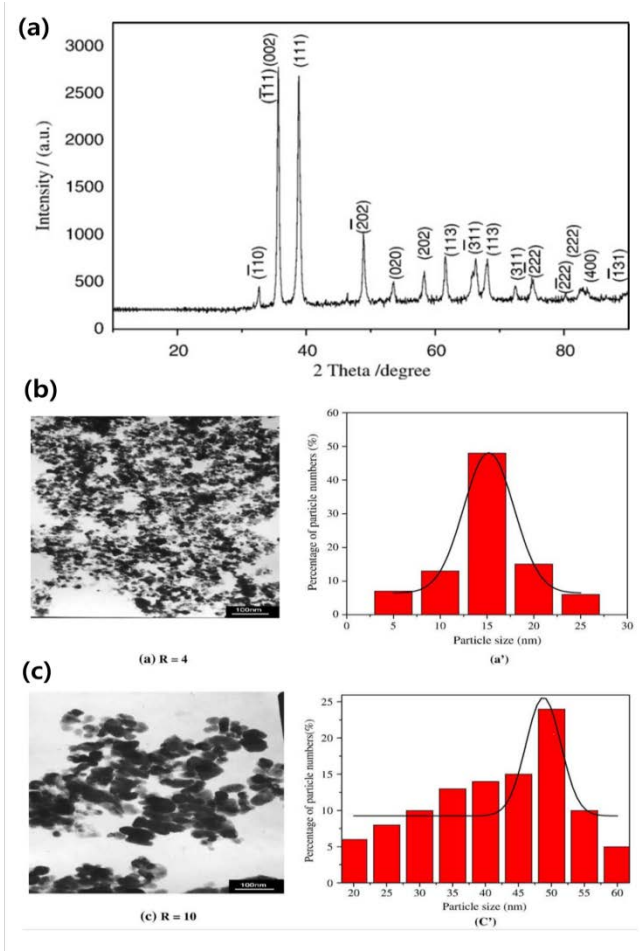

Figure 2.7 Synthesis of CuO nanoparticles using water in oil reverse micelles. (a) XRD patterns of CuO nanoparticles, (b), (c) TEM images and size distribution of nanoparticles depending on a molar ratio of water to surfactant.[35] (Reprinted with permission from Ref. [35] of Chapter 1,2)

These synthesized Cu oxide nanomaterials were used for various applications. Ananth *et al.* deal with the polyol synthesis method (using PEG) of CuO nanomaterials, which exhibited different morphology such as rice grain-like, needle-like, and plate-like structure. The different morphology of CuO nanomaterial shows the effective performance as bacterial activity inhibitor.[36] Also, Son *et al.* synthesized uniform Cu_2O nanoparticles by thermal decomposition of copper acetylacetonate. The nanoparticles existed small size of 15nm and were successfully demonstrated for the catalyst to Ullmann type amination coupling reaction of aryl chlorides.[37] (Figure 2.8) Currently, most synthetic approaches to developing pure Cu and Cu oxide utilize complex synthetic condition, which requires proper reduction agent, ambient air condition, or vacuum condition. Moreover, the inappropriate synthetic condition design of the Cu and Cu oxide particles produces unintended oxide phase or other materials. Thus, an easy, controllable, reliable, and effective approach to synthesize Cu and Cu oxide are still a great challenge.

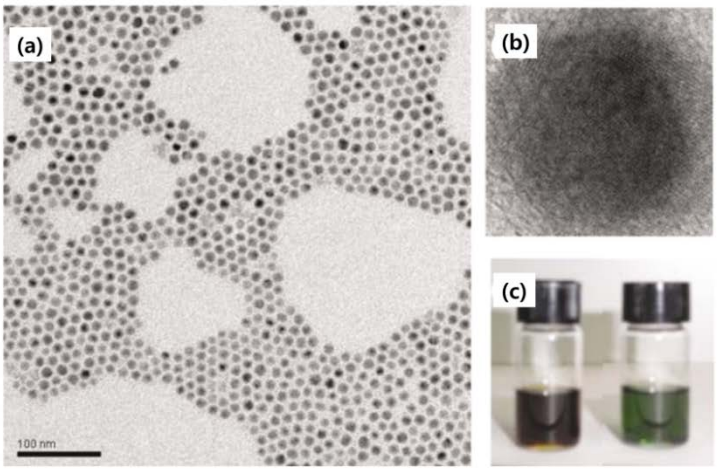

(d)

Entry	Reactant	Product	Yield(%)[b]
1	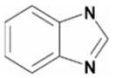	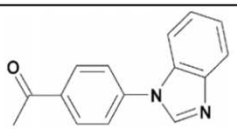	84
2			86
3		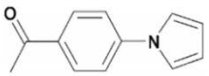	63

[a] 5 mol% Cu_2O coated Cu nanoparticles used, Cs_2CO_3, DMSO, 150°C, 18 h. [b] Isolated yield.

Figure 2.8 (a) TEM and (b) High Resolution TEM images of 15 nm Cu_2O nanoparticles. (c) Image of the just prepared Cu nanoparticles (left) and Cu_2O coated Cu nanoparticles (right). (d) Catalytic reaction for Ullmann coupling of 4-chloroacetophenone with different amines. [37] (Reprinted with permission from Ref. [37] of Chapter 1,2)

2.2 Cu-alloy nanomaterial

2.2.1 Various types of multi-component nanomaterial and Cu-alloy nanomaterial properties

Multi-component nanomaterials are basically composed of two different metal elements. The architecture of multi-component nanomaterials classifies in terms of crystal structure, internal structure (with a different number of twin defects, stacking faults), configuration (core-shell), and shape. Simply, it can be divided by spatial distribution of their corresponding element. Especially, this chapter handles the alloys, core-shell, and hetero structure. [38] (Figure 2.9) The alloy structures are the two metals that randomly and thoroughly mixed. Contrastively, the core-shell and hetero structure refer to a system that has long range atomic order. The hetero structures consist the two different clusters and share the interface of them. In addition, the core-shell structure composes the core of specific metal atoms and surrounds another metal atom as the shell. These structures tend to have distinctly different characteristics even same elemental composition.[39] The newly obtained properties give the synergistic effects for advanced application.

Among these structures, the alloy structures are widely considered for application, because Metal − Metal alloys show unique physical, chemical, electrical properties and often superior to nanocrystals made of the individual metals. Especially, Cu is the most often received attention as alloy nanomaterial candidates due to its various metal alloys. For example, magnetic bimetallic Cu - iron (Fe) core-shell nanoparticles have a catalytic reaction; aqueous azide-alkyne click reaction.[40] Cu_2ZnSnS_4 alloy nanocrystals are promising for use as thin film solar cells due to their low cost, relatively low toxicity and appropriate optical properties (band-gap energy of ~1.5 eV).[41] Gold–Copper (Au_xCu_y) alloy nanoparticles also show tunable and stable near infrared (NIR) emissions, which can be readily applied to the biological analysis.[42] (Figure 2.10)

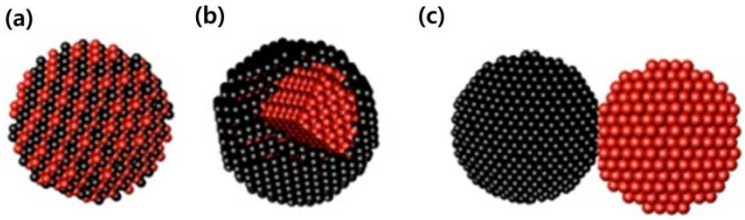

Figure 2.9 Illustration of bimetallic nanoparticles types; (a) alloyed nanostructures, (b) core-shell structures, and (c) hetero structures. [38]

(Reprinted with permission from Ref. [38] of Chapter 1,2)

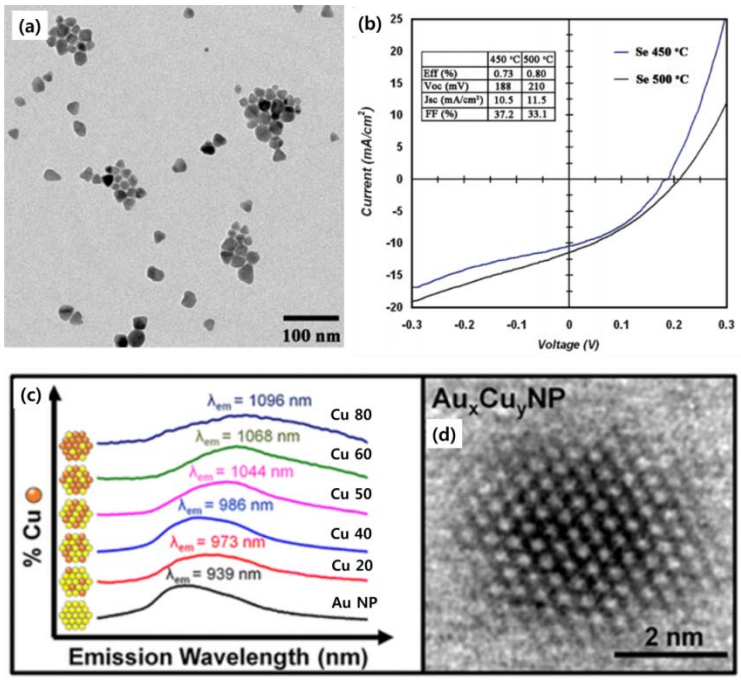

Figure 2.10 Synthesized Cu_2ZnSnS_4 alloy nanocrystals. (a) TEM image and (b) I-V characteristics of photovoltaic devices using Cu_2ZnSnS_4 nanocrystal (The efficiencies are measured under AM 1.5G illumination). [41] (c) Normalized and offset emission spectra of Au_xCu_y nanoparticles (d) HR-TEM image of Au_4Cu_6 nanoparticles.[42] (Reprinted with permission from Ref. [41],[42] of Chapter 1,2)

2.2.2 Synthesis method for copper alloy nanomaterials

The synthesis of Cu-based alloy nanomaterial is usually more complicated than mono-element (Cu, CuO, or Cu_2O) nanomaterial synthesis. As a reason, the synthesis of Cu-based alloy nanomaterial requires that various factor, comparative strengths between different elements, surface energies, relative atomic sizes, a crystal structure of each component, a strength of binding to surface ligands, should be considered.[43] Nevertheless, the Cu-based alloy nanomaterial synthesis method has evolved in different ways over the last decade. Co-reduction, thermal decomposition, seed-mediated growth, and galvanic replacement are representative examples of producing alloy nanomaterial. Among these methods, co-reduction is actually the most facile method for generating Cu-based alloy nanocrystal. The main strategy of this method is based on the simultaneous reduction from metal salt of precursors to zero-valent atoms.[44] (Figure 2.11) The co-reduction method looks simple, but it has to consider many parameters such as the reduction potentials of the metal ions, the potential of the reduction agent, the kind of coordination ligand, the surfactant, and the reaction temperature. Especially, the nucleation, growth, and structure of the alloy nanomaterial are critically affected by the

reduction rate of the metal precursor. The reduction rate of metal ion can be expressed as standard reduction potential in Table of Figure 2.11.[6] The metal ion of more positive reduction potential has faster reduction rate as compared to metal ion of lower potential. In general, metal ions with similar potentials, like Cu^{2+} ion (0.34 V) and Ni^{2+} ion (-0.25 V), should be considered for generating alloy nanocrystals using co-reduction method. As a result, selection of precursor and reduction agent is a very important factor, because it can directly influence the metal ion reduction, the reaction kinetics, and the alloy structure. For example, Guo *et al.* reported the one pot synthesis of hexagonal and triangular bimetallic nickel - copper alloy nanoplates using reduction strength control and galvanic replacement, which can simultaneously reduce the precursors of Ni and Cu.[45] (Figure 2.12) For the preparation of diverse kind of alloy Ag/Cu particles, Tsuji *et al.* proposed polyol method through co-reduction of $AgNO_3$ and $Cu(OAc)_2$ by ethylene glycol (EG) in the presence of poly vinylpyrrolidone (PVP) as a surfactant. In this study, the alloy structure, such as core-shell and bimetallic, could be controlled by reaction time, molar ratio, and standard potential of each metal.[46] (Figure 2.13) As in the previous examples, the co-reduction method has several advantages such as easy process and unnecessary to complex equipment.

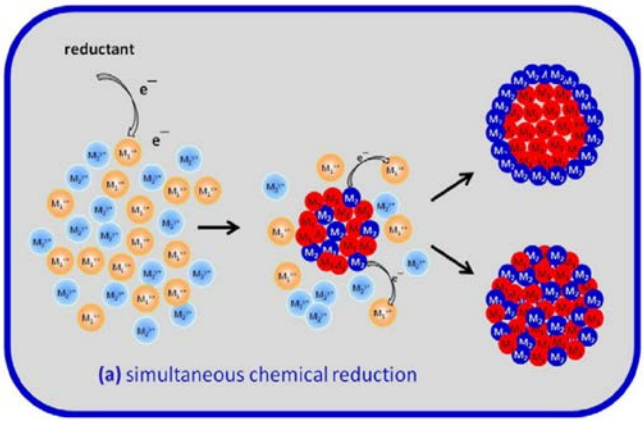

reduction reaction	E_o (V vs SHE)[a]
$Au^{3+} + 3e^- \rightarrow Au$	1.50
$Pt^{2+} + 2e^- \rightarrow Pt$	1.18
$Ir^{3+} + 3e^- \rightarrow Ir$	1.16
$Pd^{2+} + 2e^- \rightarrow Pd$	0.95
$Ag^{+} + e^- \rightarrow Ag$	0.80
$Rh^{3+} + 3e^- \rightarrow Rh$	0.76
$Ru^{3+} + 3e^- \rightarrow Ru$	0.45
$Cu^{2+} + 2e^- \rightarrow Cu$	0.34
$Ni^{2+} + 2e^- \rightarrow Ni$	−0.25
$Co^{2+} + 2e^- \rightarrow Co$	−0.28
$Fe^{2+} + 2e^- \rightarrow Fe$	−0.44

[a]Standard conditions: 25 °C and 1 atm. SHE: standard hydrogen electrode.

Figure 2.11 Mechanism of the chemical co-reduction method. [44] The simultaneous reduction of two different metal precursor makes various type of structure by reduction potentials (table) [6] (Reprinted with permission from Ref. [44],[6] of Chapter 1,2)

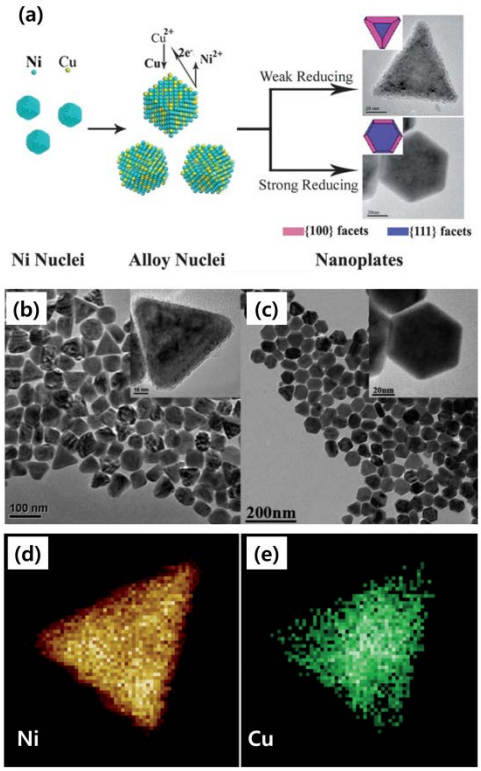

Figure 2.12 (a) Schematic illustration of triangular and hexagonal Ni-Cu alloy nanoparticles formation mechanism. TEM image of synthesized Ni-Cu alloy nanoparticles at different temperatures (b) 220 ^{o}C, and (c) 240 ^{o}C. Scanning TEM – energy dispersive X-ray spectroscopy (EDS) image for (d) Ni and (e) Cu. [45] (Reprinted with permission from Ref. [45] of Chapter 1,2)

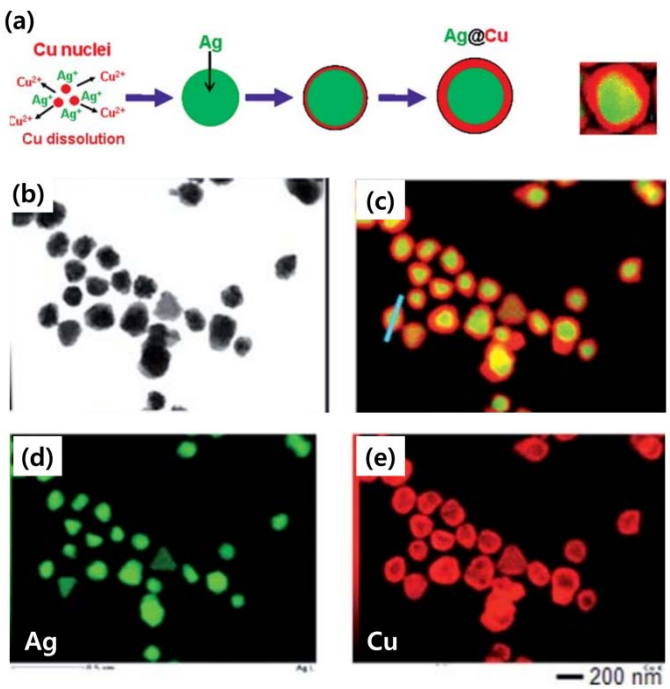

Figure 2.13 (a) Growth mechanism of Ag@Cu using polyol methods. Ag-Cu bimetallic particles prepared from Ag precursor ($AgNO_3$) and $Cu(OAc)_2$ in presence of PVP and EG mixture. In molar ratio of 0.25 [Ag]/[Cu], the bimetallic particles are investigated by (b) TEM, and EDS elemental maps for (c) overall, (d) Ag, and (d) Cu.[46] (Reprinted with permission from Ref. [46] of Chapter 1,2)

Cu-based alloy NPs can also be prepared by thermal decomposition of organometallic compounds, which composes the functional group of the carbon chain and two kinds of metal ion. The heating process simultaneously induces ion reduction and formation of alloy nanomaterial. The synthesis is usually conducted in organic solution under inert atmosphere (N_2, He gas). Similar to co-reduction, the key point of this method is a difference of decomposition rate between two metal precursors. Kim *et al.* reported the synthesis of the monodisperse bimetallic Au_xCu_y nanoparticle using oleylamine as the reducing agent and organometallic compound with the metal ion, which can gradually reduce the Au and Cu ion.[47] (Figure 2.14) In addition, monodispersed CuPd nanoparticles are synthesized by decomposition of oleylamine and oleic acid with Cu and Pd ion organometallic compound. Yin *et al.* demonstrated that CuPd bimetallic nanoparticles are prepared simply by reaction of $Cu(CH_3COO)_2$ and $Pd(CH_3COO)_2$ in oleylamine and oleic acid, which acts the solvent, surfactant. The size and composition of the CuPd nanoparticles can be precisely controlled by molar ratios tuning of Cu and Pd precursors.[48] (Figure 2.14) As described above, compared to the co-reduction method, this method is useful for preparing alloy nanoparticles with narrow size distribution and high crystallinity by high reaction temperature.

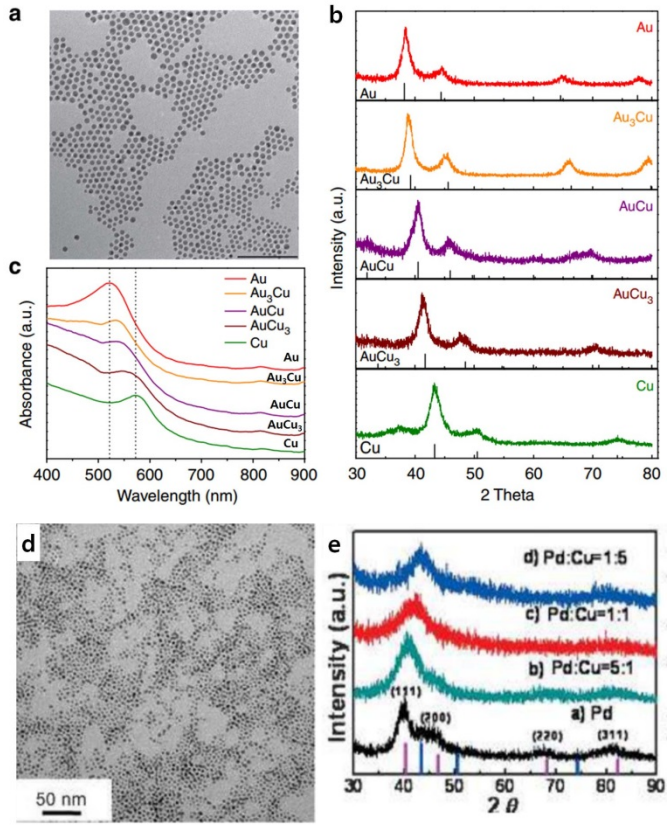

Figure 2.14 Characteristics of alloy nanoparticles. (a) TEM image of $AuCu_3$ nanoparticles with average size of 11.2 nm, (b) XRD results of Au-Cu alloy nanoparticles by atomic composition, (c) UV-vis spectra of Au-Cu alloy nanoparticles,[47](d) Pd-Cu nanoparticles (ratio of Cu/Pd 1:5)TEM images, and (e) XRD patterns of Pd-Cu alloy nanoparticles by composition. [48] (Reprinted with permission from Ref. [47],[48] of Chapter 1,2)

2.3 Application of Cu-based nanomaterial

2.3.1 Conductive electrode

2.3.1.1 Research Background

Development of electrical devices, such as smart packaging, RFID tags, flexible TFT, and PCB, demands the various techniques for fabrication of the microelectronic device. As a conventional method, the photolithography has been used for micro conductive line or electrode in electronic devices.[49] However, the multiple fabrication steps of photolithography induce the high cost, expensive equipment, and environment pollution. The needs for fabrication step simplicity have emerged to solution process fabrication such as inkjet printing, offset printing, and gravure printing. As solution process material, nanomaterials are considered to be useful for solution process electrode fabrication due to the size-dependent mesoscopic properties (melting point depression, enhanced dispersibility). For the past 10 years, various nanomaterials for solution process have intensively studied such as silver-based nanomaterial, nickel-based nanomaterial, and carbon nanomaterial (CNT, graphene).[50],[51] Mainly, the silver

nanoparticles and organosilver compound have been utilized for solution process. They have the lowest resistivity among all materials (1.59 μΩ • cm) and high redox potential, which makes them easy handle-ability and oxidation stability. However, silver, as micro size conductive electrode, has problems such as ion migration property at high temperature and humidity condition and high intrinsic cost.[52] In addition, the carbon nanomaterial is also inadequate for the conductive line, because of relatively high resistivity, the cumbersome manufacturing methods by the use of strong acids or bases, the long processing times, and their limited compatibility with conventional electronic devices. For this reason, Cu of low-cost, excellent low resistivity (1.72 μΩ • cm), and higher electro-migration resistance has obtained significant research interest in the solution process electrode fabrication field. Despite these advantages of Cu nanomaterials as solution process electrode, its practical utilization is difficult due to the inevitable oxidation of copper.[53] Therefore, overcoming of this problem is a considerable important challenge.

2.3.1.2 Issue of Cu- based electrode and Research Trend

In general, the Cu nanomaterial oxidation process is affected by two main steps: nanoparticle preparation (including synthesis, storage, washing), and sintering process for particle necking. First, to protect the nanoparticle preparation oxidation, the various strategies are proposed such as coating with inert material shell or dense layer of capping agents. Ang *et al.* proposed alkanethiol coated Cu nanoparticles. The research demonstrated that the presence of surfactant layer, composed by alkanethiol (from C_8 to C_{12}), has good oxidation barrier property of Cu nanoparticles for least six months.[54] More stable dispersion and oxidation stable properties are obtained by polymer capping agents, poly (N-vinlpyrrolidone) (PVP). Engels, V *et al.* and Jeong, S. *et al.* evaluates the oxidation property of Cu nanoparticle depending on PVP molecular weights from 10,000 to 40,000 g/mol.[55], [56] However, these high density and molecular weight of capping agents induce high sintering temperature for particle necking, and high resistivity by remaining of organic residue. As an alternative, core-shell structure, Cu (core) – Ag (shell), has been explored for oxidation protection and achievement of low resistivity. Grouchko, M *et al.* reported the synthesis of Cu nanoparticles in the first step, which was prepared by

reducing $Cu(NO_3)_2$ in the presence of hydrazine as reducing agents, and polyacrylic acid as a stabilizer. In the second step, the Ag ions are reduced by galvanic reaction with Cu metal. After the reaction, the silver coated copper nanoparticles are synthesized and show the low resistivity.[57] (Figure 2.15) In addition, Luechinger, N.A. *et al.* proposed graphene coated Cu nanoparticles for full protection of Cu metal core under humid air condition. This found stable oxidation property up to 165 ^{o}C and simple process as one pot.[58] However, these methods have also critical disadvantages, which are high temperature stability by silver aggregation and atomic separation and high resistivity by the intrinsic carbon resistivity property.

Recently, the metal ion complex is also proposed. The main advantage of ion complex ink is low temperature decomposition and highly stable storage property, because they maintain monovalent, or divalent ion states of Cu in the ion complex. Choi *et al.* offered novel Cu ion complex ink with Cu formate precursor. The ion complex ink was sintered *via* low temperature sintering and reduction, which showed the low electrical resistivity of 8 μΩ cm. [59] (Figure 2.16) In addition, Cu- based alloy nanoparticles are proposed for electrode fabrication and highly oxidation stable property. Kim *et al.* developed Au-Cu bimetallic nanoparticles by oleylamine based

thermal decomposition process. The Ag-Cu nanoparticles of narrow size distribution were obtained by controlling of reaction time and precursor injection time. Through theoretical study, the author demonstrates that bimetallic nanoparticles are less affected by oxidation.

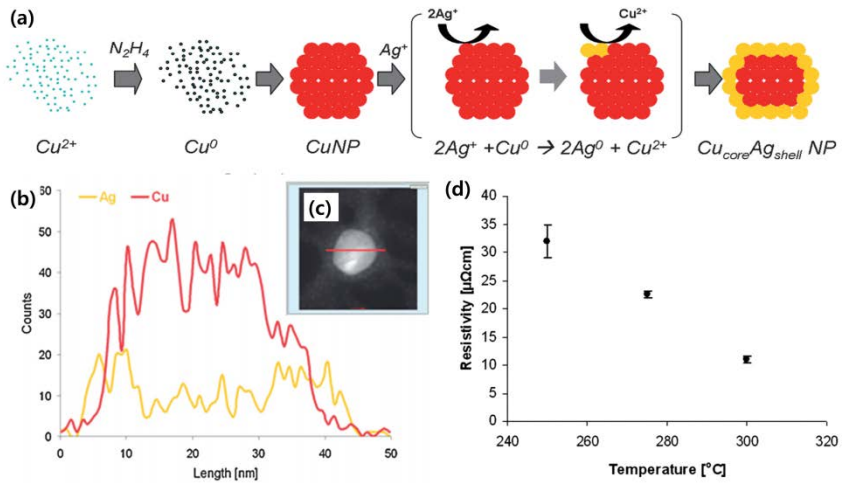

Figure 2.15 (a) Schematic illustration of the Cu@Ag nanoparticles synthetic method. (b) Elemental profile and (c) STEM image of Cu@Ag nanoparticles, (d) The resistivity by sintered Cu@Ag nanoparticles.[57]

(Reprinted with permission from Ref. [57] of Chapter 1,2)

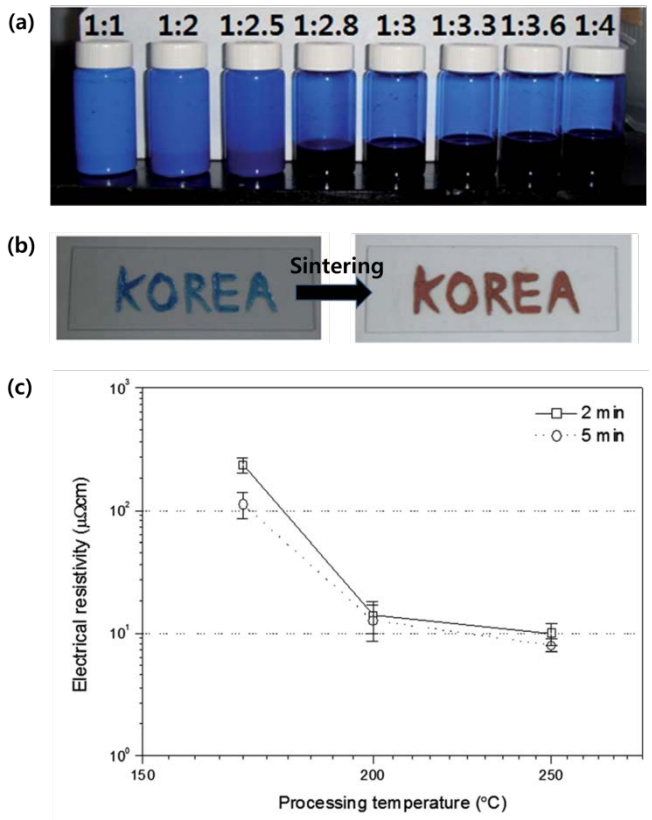

Figure 2.16 Photograph of (a) the Cu ion complex ink, (b) the letter of before and after sintering, (c) Electrical resistivity of Cu conductive film using Cu ion complex ink .[59] (Reprinted with permission from Ref. [59] of Chapter 1,2)

For oxidation protection of sintering process, various alternative sintering techniques are emerged such as intensive pulse laser (IPL) or chemical etching. The laser sintering method generates pulse, employing a xenon lamp, of incoherent light with various wavelengths from 190 nm to 1000 nm. The light absorbed Cu nanoparticles rise temperature in localized surface, resulting in sintering between neighboring particles. Dharmadasa *et al.* reported the Cu conducting film formation using Cu nanoparticles with IPL sintering method. In this research, Cu nanoparticles showed simply Cu reduction, IPL parameter optimization for conductive Cu film fabrication, and a low sheet resistance of 0.12 Ω/□.[60] (Figure 2.17) The chemical etching method is particle necking by chemically melting the Cu particle surface. Wu *et al.* demonstrated the sintering of Cu particles at room temperature. The authors successfully accomplished the ascorbic acid assisted reduction process, which showed outstanding electrical resistivity. In addition, this method can form the conductive line on the flexible substrate, polyethylene terephthalate (PET), polycarbonate (PC), and polyimide (PI), due to room temperature sintering.[61] Despite these recent efforts for oxidation protection, the adequate electrode fabrication methods are not proposed, so it is an important challenge for high performance and low cost electrode fabrication.

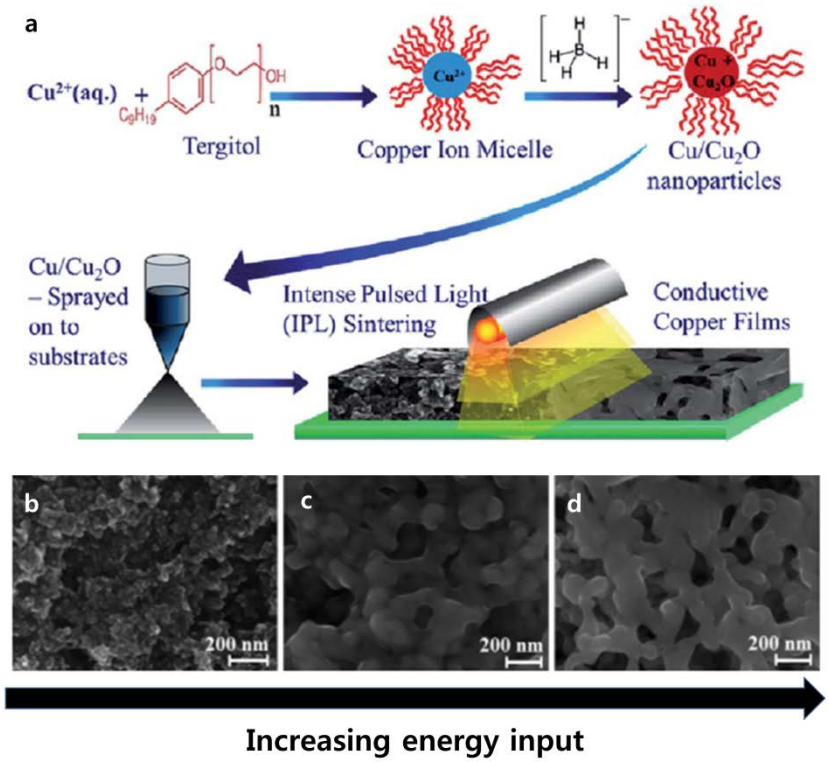

Figure 2.17 (a) Schematic representation of the Cu nanoparticles ink synthetic method and IPL sintering process for conductive film fabrication, (b), (c), and (d) SEM topographical image of IPL treated film with energy input increasing from 576 J cm^{-2} to 1723 J cm^{-2}.[60] (Reprinted with permission from Ref. [60] of Chapter 1,2)

2.3.2 Lithium ion battery

2.3.2.1 Research Background

The importance of effective energy storage is emerged for replacement of conventional fossil fuel. The lithium ion batteries (LIB) are considered as renewable and sustainable energy source, because it is operated without environmental pollution.[62],[63] Especially, the LIB has important property, high energy density, high power density, low self-discharge property, and long cycle stability. These properties make it possible to consider them to wide range application from portable devices to electric vehicles.[64] However, for huge electric vehicles, the LIB technology needs to provide 2~5 times more energy density than current cell performance (current energy density: 150 wh kg^{-1}).[65] For this reason, the studies are being carried out to high energy density of LIB through the development of high capacity anode and cathode materials. In next chapter, the previous researches of the high capacity anode and cathode materials, LIB basic structure, and the mechanism will be introduced.

2.3.2.2 Basic structure and mechanism of LIBs

As you can see in Figure 2.18, the typical LIB consists four main part; cathode, anode, electrolyte, and separator.[66] The cathode is a positive electrode where reduction reaction occurs during discharging process. Next, the anode, as negative electrode, has oxidation process in discharging step. The electrolytes conduct the Li^+ transport media, and the separator acts preventing of direct electrical contact between cathode and anode. As reaction mechanism, the fundamental reaction of LIB is based on intercalation/de-intercalation, which is reversible insertion of Li ion into each electrode. The detailed electrochemical reactions of charging/discharging are represented as follow;

Anode:

$C + xLi + xe^- \leftrightarrow LixC_6$

Cathode:

$LiCoO_2 \leftrightarrow Li_{1-x}CoO_2 + xLi + xe^-$

These intercalation/de-intercalation processes are described as the “rocking-chair system”, which induces LIB rechargeable property, occurring indefinitely reversible reaction during the cell operation.

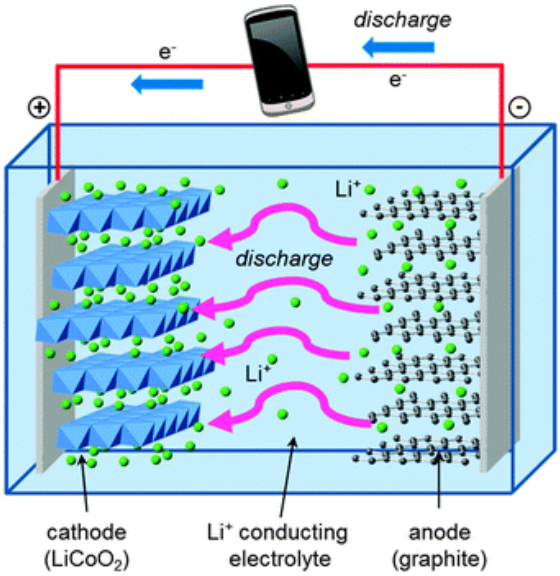

Figure 2.18 Schematic illustration of lithium ion battery charge/discharge principle.[66] (Reprinted with permission from Ref. [66] of Chapter 1,2)

With regard to materials, the main part of LIB are composed as transition metal oxide or phosphates (cathode), graphite (anode), PE or PP (separator), and lithium salts in alkyl organic carbonates (electrolyte). Among these components, the active materials are very important, because its capacity has a direct effect on energy density. The conventional cathode, $LiCoO_2$, of 140 mAh g^{-1} and anode, graphite, of 372 mAh g^{-1} are utilized in practice, but insufficient energy density for recent huge application has led to finding new electrode material. To satisfy the criteria, research of cathode is being carried out worldwide to find alternative material based on eco-friendly and low cost. As a result, various prospective cathode materials, such as $LiMn_2O_4$ and $LiFePO_4$, are proposed in practical cell system.[62],[63] However, the studies of anode materials have not been sufficiently conducted. Thus, research related to the anode is very necessary and will be introduced in the next chapter.

2.3.2.3 Issue of Anode materials for LIB

The Li metal is the most fascinating anode materials due to low electrochemical potential and light weight for high energy density.[67] Unfortunately, the Li metal has critical disadvantages such as safety issue

by Li dendrite, and poor cycling property. As alternative of the Li metal, graphitic carbon, graphitizable carbon (soft carbon), and non-graphitized glassy carbon (hard carbon) are proposed in practical LIB system. It accommodates the Li ion in those crystalline structures (intercalation), resulting to show stable charge/discharge cycle property. However, graphite contain the intercalation of one Li ion *vs* six carbon atoms (stoichiometry of LiC_6), which makes low reversible capacity of 372 mAh g^{-1}. The low capacity of graphite is not appropriate for huge application, like EV. Thus, the various next generation anode materials are reported and it is classified as different reaction mechanism, such as alloying reaction and conversion reaction. [68] (Figure 2.19)

Lithium alloys, Li_xM_y, have been great interest as high capacity anode materials in LIB. This active material of alloy reaction with Li is called alloy/de-alloy mechanism as below;

$$Li_xM \leftrightarrow xLi^+ + xe^- + M$$

The examples of typical alloy metals are silicon, tin oxide, and germanium, which show the higher capacity rather than intrinsic graphite capacity. Capacities of these anodes have wide ranges from 783 of tin oxide to 4200 of silicon. Unfortunately, the alloying/de U alloying reactions accompany the large volume expansion after cycling test, resulting in rapid

degradation of the electrode and capacity fading. Significant research has been proposed to solve the pulverization problem. Structure design of Si nanowire reduces the alloying stress from volume expansion during the charge/discharge cycling.[69] In addition, hollow tin dioxide microsphere has been reported as stable cycling structure, because the hollow space has a role of expansion stress releasing. [70] As the latter, the conversion reaction materials for high capacity have been proposed using transition metal compounds, such as metal oxide, nitrides, phosphides, and sulfides. The conversion reaction of metal oxide is described as below;

$$Li_xM \leftrightarrow xLi^+ + xe^- + M$$

(M = Fe, Co, Cu, Mn, Ni, etc.)

The full reduction of oxide induces composite materials, including nano-sized metal particles from 2 to 8 nm, dispersed in a Li_2O matrix.[71] These transitions provide high reversible capacities (2~5 times) due to high number of reaction per unit atom with Li ion. For the same reason, the metal compounds, including nitrides, phosphides, and sulfides, have also high capacity and reaction mechanism as follow;

$$M_xN_y + zLi^+ + ze^- \leftrightarrow xM + Li_zN_y$$

(N = O, P, S, N)

The example of conversion reaction is reported by P. Poizot *et al.*. [72] In

this research, the nano-sized transition metal oxides, such as CoO, NiO, Cu_2O, and FeO, react with Li ion in the solid state and investigate the reaction mechanism and optimization for nano-size distribution. As another report, Reddy *et al.* described the electrochemical performance of micro sized Co_3O_4 crystal using molten salt synthesis. The synthesis by several Cobalt salts (sulphate, hydroxide, and acetate) reveals the various crystal morphology and different electrochemical properties. [73]

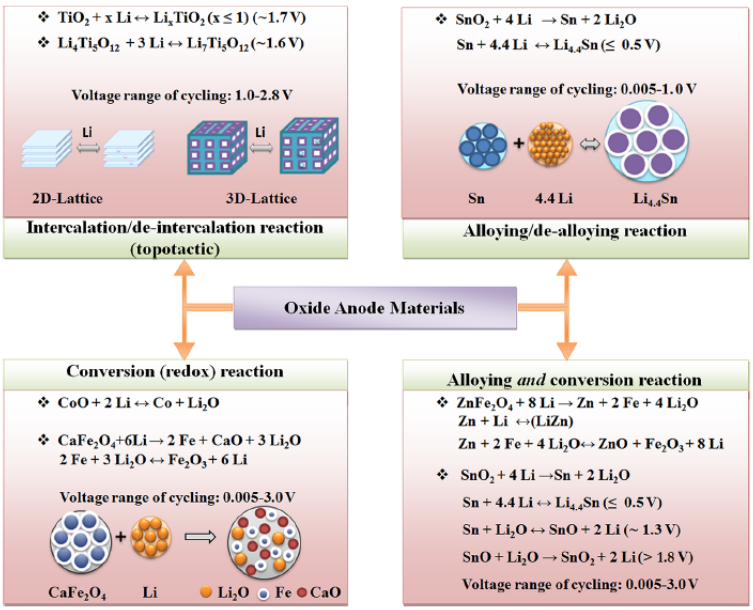

Figure 2.19 Classification of oxide anode material; Intercalation-deintercalation, alloying-dealloying, and conversion reaction. [68] (Reprinted with permission from Ref. [68] of Chapter 1,2)

2.3.2.4 Research trend of Cu oxide anode

The Cu-based nanomaterial anode has also been applied as the attractive alternative anode. The acceptable theoretical capacity, Cu_2O (375 mAh g^{-1}) and CuO (674 mAh g^{-1}), leads to focus the nanomaterial anode research by Cu oxide crystals. For example, Tarascon group has first developed these two oxides crystal, which found particle size has the effect on capacity reversibility. It shows the stable capacity of 400 mAh g^{-1} up to 70 cycles at the voltage range of 0.02 – 3.0 V.[74] (Figure 2.20) In subsequent studies, studies of various shape CuO, nanowires, nanoribbon array, leaf-like nanoplates, and hierarchical nanostructures, have been established. The CuO nanowire shows the stable capacity of 650 up to 100 cycles at 0.5 C-rate. The enhanced cycling property is affected on outstanding electronic conductivity by Cu nanoparticle formation of conversion reaction, and effective contact between nanowires.[75] In addition, for protecting of capacity fading phenomenon, CuO hierarchical hollow nanospheres are reported by Kong *et al.*. [76] (Figure 2.20) The synthesis of CuO hollow nanospheres with diameters of about 400 nm is demonstrated. The unique structure could release the strain energy associated with lithium insertion/removal and offer a suitable electrode/electrolyte contact area.

Recently, the research of Cu oxide composite materials is rapidly increasing in order to compensate the capacity fading and intrinsic conductivity. The typical example is the carbon based material (CNT, graphene, carbon shell) and Cu oxide composite. Ko *et al.* proposed a facile method for CuO/ MWCNT nanocomposite for high porosity, enhanced electronic conductivity, and long term cycling stability. The synergic effect of high capacity by CuO nanoparticles and high conductivity by CNT make significant advances as lithium ion battery anode.[77] (Figure 2.21) Consequently, these unique Cu based nanomaterial structure design and composite methods have been developed for high stability, capacity, and high energy density. However, it's difficult to apply the practical LIB of advanced application due to the complexity of the process and unstable electrochemical characteristics. For this reason, the facile Cu based nanomaterial composite synthesis and effective structure design for high capacity and cycling stable remain a significant challenge.

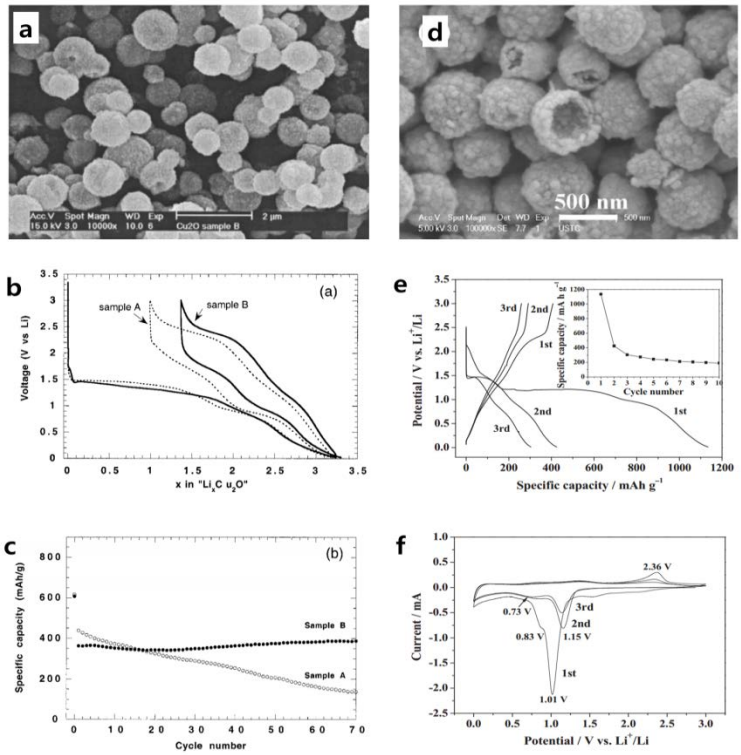

Figure 2.20 (a) SEM image of 150 nm size Cu_2O particles, (b) Voltage profile of Cu_2O/Li cell, and (c) long term cycling stability. (Sample A is 150 nm and Sample B is 1 μ m) [72] (d) CuO hollow nanospheres SEM image, (e) Charge-discharge curves and (f) Cyclic voltammogram of CuO/Li cell in range of 0.01 – 3.0 V. The inset is the cycling performance.[74] (Reprinted with permission from Ref. [72],[74] of Chapter 1,2)

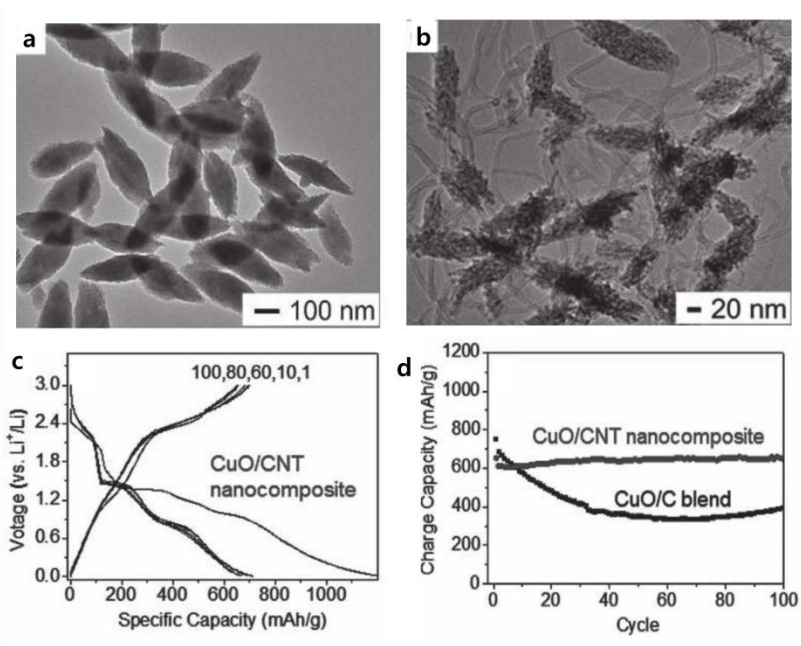

Figure 2.21 TEM image of (a) CuO nanoparticles (b) CuO/CNT nanocomposite using porous $Cu(OH)_2$ chemical transformation and CNT blending, (c) Voltage profile of the CuO/CNT nanocomposite, (d) Long term cycling stability, comparing with CuO/CNT and CuO/C blending electrode.[77] (Reprinted with permission from Ref. [77] of Chapter 1,2)

References

[1] J. Park, J. Joo, S. G. Kwon, Y. Jang and T. Hyeon, *Angew. Chem. Int. Edit.*, 2007, **46**, 4630.

[2] V. K. Sharma, J. Filip, R. Zboril and R. S. Varma, *Chem. Soc. Rev.*, 2015, **44**, 8410.

[3] X. J. Xue, F. Wang and X. G. Liu, *J. Mater. Chem.*, 2011, **21**, 13107.

[4] G. Collins, M. Schmidt, C. O. Dwyer, J. D. Holmes and G. P. McGlacken, *Angew. Chem. Int. Edit.*, 2014, **53**, 4142.

[5] S. Y. Wei, Q. Wang, J. H. Zhu, L. Y. Sun, H. F. Lin and Z. H. Guo, *Nanoscale*, 2011, **3**, 4474.

[6] K. D. Gilroy, A. Ruditskiy, H. C. Peng, D. Qin and Y. N. Xia, *Chem. Rev.*, 2016, **116**, 10414.

[7] Y. Y. Ma, W. Y. Li, E. C. Cho, Z. Y. Li, T. K. Yu, J. Zeng, Z. X. Xie and Y. N. Xia, *Acs Nano*, 2010, **4**, 6725.

[8] D. V. Talapin, A. L. Rogach, A. Kornowski, M. Haase and H. Weller, *Nano Lett.*, 2001, **1**, 207.

[9] S. H. Sun and H. Zeng, *J. Am. Chem. Soc.*, 2002, **124**, 8204.

[10] Y. Sugano, Y. Shiraishi, D. Tsukamoto, S. Ichikawa, S. Tanaka and T. Hirai, *Angew. Chem. Int. Edit.*, 2013, **52**, 5295.

[11] S. T. Chen, S. V. Jenkins, J. Tao, Y. M. Zhu and J. Y. Chen, *J. Phys. Chem. C*, 2013, **117**, 8924.

[12] S. Norita, D. Kumaki, Y. Kobayashi, T. Sato, K. Fukuda and S. Tokito, *Org. Electron.*, 2015, **25**, 131.

[13] P. Lignier, R. Bellabarba and R. P. Tooze, *Chem. Soc. Rev.*, 2012, **41**, 1708.

[14] H. Z. Guo, X. Liu, Q. S. Xie, L. S. Wang, D. L. Peng, P. S. Branco and M. B. Gawande, *Rsc Adv.*, 2013, **3**, 19812.

[15] A. Bansal, J. S. Sekhon and S. S. Verma, *Plasmonics*, 2014, **9**, 143.

[16] M. B. Gawande, A. Goswami, F. X. Felpin, T. Asefa, X. X. Huang, R. Silva, X. X. Zou, R. Zboril and R. S. Varma, *Chem. Rev.*, 2016, **116**, 3722.

[17] S. Jeong, H. C. Song, W. W. Lee, S. S. Lee, Y. Choi, W. Son, E. D. Kim, C. H. Paik, S. H. Oh and B. H. Ryu, *Langmuir*, 2011, **27**, 3144.

[18] K. Chanda, S. Rej and M. H. Huang, *Chem-Eur. J.*, 2013, **19**, 16036.

[19] S. D. Sun, *Nanoscale*, 2015, **7**, 10850.

[20] D. Q. Liu, Z. B. Yang, P. Wang, F. Li, D. S. Wang and D. Y. He, *Nanoscale*, 2013, **5**, 1917.

[21] J. Y. Xiang, J. P. Tu, X. H. Huang and Y. Z. Yang, *J. Solid State Electr.*, 2008, **12**, 941.

[22] L. T. Yu, Y. Y. Jin, L. L. Li, J. Ma, G. F. Wang, B. Y. Geng and X. J. Zhang, *Crystengcomm.*, 2013, **15**, 7657.

[23] S. Pande, S. Jana, S. Basu, A. K. Sinha, A. Datta and T. Pal, *J. Phys. Chem. C*, 2008, **112**, 3619.

[24] A. S. Zoolfakar, R. A. Rani, A. J. Morfa, A. P. O'Mullane and K. Kalantar-Zadeh, *J. Mater. Chem. C*, 2014, **2**, 5247.

[25] T. Herricks, J. Y. Chen and Y. N. Xia, *Nano Lett.*, 2004, **4**, 2367.

[26] M. H. Kim, B. Lim, E. P. Lee and Y. N. Xia, *J. Mater. Chem.*, 2008, **18**, 4069.

[27] J. Park, K. J. An, Y. S. Hwang, J. G. Park, H. J. Noh, J. Y. Kim, J. H. Park, N. M. Hwang and T. Hyeon, *Nat. Mater.*, 2004, **3**, 891.

[28] M. Salavati-Niasari and F. Davar, *Mater. Lett.*, 2009, **63**, 441.

[29] J. N. Solanki, R. Sengupta and Z. V. P. Murthy, *Solid State Sci.*, 2010, **12**, 1560.

[30] C. Vazquez-Vazquez, M. Banobre-Lopez, A. Mitra, M. A. Lopez-Quintela and J. Rivas, *Langmuir*, 2009, **25**, 8208.

[31] B. K. Park, S. Jeong, D. Kim, J. Moon, S. Lim and J. S. Kim, *J. Colloid. Interf. Sci.*, 2007, **311**, 417.

[32] M. A. Ben Aissa, B. Tremblay, A. Andrieux-Ledier, E. Maisonhaute, N.

Raouafi and A. Courty, *Nanoscale*, 2015, **7**, 3189.

[33] M. Sabbaghan, J. Beheshtian and R. N. Liarjdame, *Mater. Lett.*, 2015, **153**, 1.

[34] M. Yin, C. K. Wu, Y. B. Lou, C. Burda, J. T. Koberstein, Y. M. Zhu and S. O'Brien, *J. Am. Chem. Soc.*, 2005, **127**, 9506.

[35] D. Y. Han, H. Y. Yang, C. Y. Zhu and F. H. Wang, *Powder Technol.*, 2008, **185**, 286.

[36] A. Ananth, S. Dharaneedharan, M. S. Heo and Y. S. Mok, *Chem. Eng. J.*, 2015, **262**, 179.

[37] S. U. Son, I. K. Park, J. Park and T. Hyeon, *Chem. Commun.*, 2004, **7**, 778.

[38] S. Alayoglu, A. U. Nilekar, M. Mavrikakis and B. Eichhorn, *Nat. Mater.*, 2008, **7**, 333.

[39] Z. J. Zhang, L. M. Wang, J. Wang, X. M. Jiang, X. H. Li, Z. J. Hu, Y. H. Ji, X. C. Wu and C. Y. Chen, *Adv. Mater.*, 2012, **24**, 1418.

[40] R. Hudson, C. J. Li and A. Moores, *Green Chem.*, 2012, **14**, 622.

[41] Q. J. Guo, H. W. Hillhouse and R. Agrawal, *J. Am. Chem. Soc.*, 2009, **131**, 11672.

[42] C. M. Andolina, A. C. Dewar, A. M. Smith, L. E. Marbella, M. J. Hartmann and J. E. Millstone, *J. Am. Chem. Soc.*, 2013, **135**, 5266.

[43] R. Ferrando, J. Jellinek and R. L. Johnston, *Chem. Rev.*, 2008, **108**, 845.

[44] A. Zaleska-Medynska, M. Marchelek, M. Diak and E. Grabowska, *Adv. Colloid Interfac.*, 2016, **229**, 80.

[45] H. Z. Guo, Y. Z. Chen, H. M. Ping, L. S. Wang and D. L. Peng, *J. Mater. Chem.*, 2012, **22**, 8336.

[46] M. Tsuji, S. Hikino, R. Tanabe, M. Matsunaga and Y. Sano, *Crystengcomm.*, 2010, **12**, 3900.

[47] D. Kim, J. Resasco, Y. Yu, A. M. Asiri and P. D. Yang, *Nat. Commun.*, 2014, **5**, 4948.

[48] Z. Yin, W. Zhou, Y. J. Gao, D. Ma, C. J. Kiely and X. H. Bao, *Chem-*

Eur. J., 2012, **18**, 4887.

[49] Y. Lee, J. R. Choi, K. J. Lee, N. E. Stott and D. Kim, *Nanotechnology*, 2008, **19,** 415604.

[50] K. Kordas, T. Mustonen, G. Toth, H. Jantunen, M. Lajunen, C. Soldano, S. Talapatra, S. Kar, R. Vajtai and P. M. Ajayan, *Small*, 2006, **2**, 1021.

[51] D. Kong, L. T. Le, Y. Li, J. L. Zunino and W. Lee, *Langmuir*, 2012, **28**, 13467.

[52] M. Hosel and F. C. Krebs, *J. Mater. Chem.*, 2012, **22**, 15683.

[53] K. V. Abhinav, R. V. K. Rao, P. S. Karthik and S. P. Singh, *Rsc Adv.*, 2015, **5**, 63985.

[54] T. P. Ang, T. S. A. Wee and W. S. Chin, *J. Phys. Chem. B*, 2004, **108**, 11001.

[55] S. Jeong, K. Woo, D. Kim, S. Lim, J. S. Kim, H. Shin, Y. N. Xia and J. Moon, *Adv. Funct. Mater.*, 2008, **18**, 679.

[56] V. Engels, F. Benaskar, D. A. Jefferson, B. F. G. Johnson and A. E. H. Wheatley, *Dalton T.*, 2010, **39**, 6496.

[57] M. Grouchko, A. Kamyshny and S. Magdassi, *J. Mater. Chem.*, 2009, **19**, 3057.

[58] N. A. Luechinger, E. K. Athanassiou and W. J. Stark, *Nanotechnology*, 2008, **19**, 445201.

[59] Y. H. Choi, J. Lee, S. J. Kim, D. H. Yeon and Y. Byun, *J. Mater. Chem.*, 2012, **22**, 3624.

[60] R. Dharmadasa, M. Jha, D. A. Amos and T. Druffel, *Acs. Appl. Mater. Inter.*, 2013, **5**, 13227.

[61] C. J. Wu, Y. J. Sheng and H. K. Tsao, *J. Mater. Chem. C*, 2016, **4**, 3274.

[62] J. M. Tarascon and M. Armand, *Nature*, 2001, **414**, 359.

[63] B. Scrosati, J. Hassoun and Y. K. Sun, *Energ. Environ. Sci.*, 2011, **4**, 3287.

[64] M. Winter and R. J. Brodd, *Chem. Rev.*, 2004, **104**, 4245.

[65] M. M. Thackeray, C. Wolverton and E. D. Isaacs, *Energ. Environ. Sci.*,

2012, **5**, 7854.

[66] M. Saiful Islam, Craig A. J. Fisher, *Chem. Soc. Rev.*, 2014, 43, 185.

[67] S. Goriparti, E. Miele, F. De Angelis, E. Di Fabrizio, R. P. Zaccaria and C. Capiglia, *J. Power Sources*, 2014, **257**, 421.

[68] M. V. Reddy, G. V. S. Rao and B. V. R. Chowdari, *Chem. Rev.*, 2013, **113**, 5364.

[69] C. K. Chan, H. L. Peng, G. Liu, K. McIlwrath, X. F. Zhang, R. A. Huggins and Y. Cui, *Nat. Nanotechnol.*, 2008, **3**, 31.

[70] S. J. Han, B. C. Jang, T. Kim, S. M. Oh and T. Hyeon, *Adv Funct Mater*, 2005, **15**, 1845.

[71] M. Armand and J. M. Tarascon, *Nature*, 2008, **451**, 652.

[72] P. Poizot, S. Laruelle, S. Grugeon, L. Dupont and J. M. Tarascon, *Nature*, 2000, **407**, 496.

[73] M. V. Reddy, Z. Beichen, L. J. Nicholette, Z. Kaimeng and B. V. R. Chowdari, *Electrochem. Solid St.*, 2011, **14**, A79.

[74] S. Grugeon, S. Laruelle, R. Herrera-Urbina, L. Dupont, P. Poizot and J. M. Tarascon, *J Electrochem. Soc.*, 2001, **148**, A285.

[75] L. B. Chen, N. Lu, C. M. Xu, H. C. Yu and T. H. Wang, *Electrochim Acta*, 2009, **54**, 4198.

[76] M. Kong, W. X. Zhang, Z. H. Yang, S. Y. Weng and Z. X. Chen, *Appl. Surf. Sci.*, 2011, **258**, 1317.

[77] S. Ko, J. I. Lee, H. S. Yang, S. Park and U. Jeong, *Adv. Mater.*, 2012, **24**, 4451.

Chapter 3. Pressure-assisted electrode fabrication using simply synthesized Cu_3Sn alloy nanoparticles

3.1 Introduction

Alloy nanoparticles have recently emerged as new attractive materials due to their advanced electrical, optical, magnetic, and catalytic properties when compared to the intrinsic properties of each of the elements.[1,2] Over the past several years, many researchers have been drawn to the synthesis method and noble-transition bimetallic or trimetallic alloy nanoparticles application due to their high catalytic performance or electrical properties.[3] Of these, silver or silver alloy nanoparticles have drawn interest because of their unique optical property, good oxidation-resistivity, low electron resistivity, etc. However, the high cost of silver or silver alloy nanostructures makes it difficult for utilization in various industrial applications.[4,5] On the other hand, as copper is abundant and has a relatively low cost, copper alloy nanoparticles have been introduced as an alternative to silver. For example, Cu_2ZnSnS_4 nanocrystals are promising

for use as thin film solar cells due to the low cost, relatively low toxicity and appropriate optical properties (band-gap energy of ~1.5 eV).[6] Gold-Copper (Au_xCu_y) alloy nanoparticles also show stability and are tunable near infrared (NIR) emissions, which can be readily applied to biological analysis.[7]

Among various applications, the advanced electrode fabrication based on copper (Cu) nanoparticles has received a significant amount of attention due to the potential for use in ink jet printing or offset printing.[8,9] In particular, the Cu conductive nanoparticles have drawn interest due to the size effect of the melting point depression, which facilitates low temperature sintering for flexible electronics.[10] In addition, the nano-size electrode fabrication using conductive nanoparticles has a strong advantage; the simple printing process, which is better than conventional electrode fabrication like photolithography.[11] Cu nanoparticle ink has also good merits for repairing of disconnected electric wiring in electronic devices. Electrode fabrication using Cu nanoparticle ink is feasible for various applications, such as field effect transistor, solar cells, sensors, light emitting diodes, etc.[12,13] However, pure Cu nanoparticles have high reactivity that inevitably produce oxide layer during the purification process, storage in air condition, and sintering process for electrode fabrication.[14] The oxide layer of Cu

nanoparticles has a negative effect on electrical resistivity, so cumbersome additional processes are needed to prevent its growth. For example, the sintering and storage of Cu nanoparticles require specific inert conditions, such as vacuum condition or nitrogen gas.[15] Additionally, the stabilizers for oxidation-resistivity, which are generally composed of organic materials, act as insulating layers on Cu nanoparticles. Therefore, they need a high decomposition temperature for use in conductive electrode fabrication, which limits the flexible substrates choices due to the thermal deformation of plastic materials.[16,17] In spite of the advantages of a simple electrode fabrication process using conductive ink based on Cu nanoparticles, these restrictions strongly inhibit applications in future flexible or wearable devices. Thus, alternative materials or processes for a low cost, high oxidation-resistivity, and low temperature fabrication are required.

To address these issues, the novel Cu_3Sn alloy nanoparticles synthesis with good oxidation-resistance and the application for a pressure-assisted room temperature electrode fabrication are introduced. The highly oxidation stable Cu_3Sn alloy nanoparticles (60 nm average size) are synthesized using simple one-pot synthetic process. In the Cu_3Sn alloy nanoparticles synthesis, copper precursor, tin precursor, oleic acid, and oleylamine were used. The synthesized Cu_3Sn alloy nanoparticles did not change the electron

resistivity during 4 weeks in ambient conditions. The Cu_3Sn alloy nanoparticles showed the low electrical resistivity on flexible substrates via the pressure-assisted electrode fabrication. The pressure on the Cu_3Sn alloy nanoparticles dramatically induced the interconnection between the neighboring Cu_3Sn alloy nanoparticles. As a result, in spite of the room temperature process, the electron resistivity of the Cu_3Sn alloy nanoparticles showed a value which is similar to that of conventional electrodes fabricated using pure copper or silver nanoparticle ink at a high temperature and inert gas sintering process.[18,19,20]

3.2 Experimental section

3.2.1 Cu_3Sn nanoparticles synthesis

Copper(II) acetylacetonate ($Cu(acac)_2$, Aldrich, 0.1 g) and Tin(II) acetylacetonate ($Sn(acac)_2$, Aldrich, 0.028g) dissolved in 10 mL of Oleylamine (Aldrich, 70%) and 1mL Oleic acid (Aldrich, 90%) mixed solution was heated to 120 ^oC for 30 minutes under vacuum conditions. The solution was then heated under nitrogen gas to a temperature of 310 ^oC with stirring. When the solution reached the temperature of 310 ^oC, the solution was left to react for 1 hour. The solution was then cooled to room temperature. Finally, the reacted solution was mixed with ethanol and hexane, and then the synthesized nanoparticles were conducted to centrifugation. The precipitates were washed with ethanol and hexane several times. The precipitated nanooparticles were dried in a vacuum oven (40 ^oC)

3.2.2 Preparation of Cu_3Sn conductive electrodes

The circle punched shielding layer (3M tape) of 5mm diameter attached on the PET substrates. The nanoparticle powder was loaded in the hole of

shielding layer (powder weight: 0.03g) and covered the upper PET layer. Loading powder was applied to the setting pressure using a hydraulic pump press machine. The experiments were continued for 3 minutes at room temperature. The pressed sample was separated into an upper PET layer, a shielding layer on PET substrates and sample. The same process is repeated for fabricate a complex shape of conductive electrode. Then, the 3M tape, as an adhesive layer, attaches the each sample such as round, line and complex shapes.

3.2.3 Resistivity measurements

Resistivity measurements of the sample were carried out in a four-point DC resistivity measurement setup. To make a four-point measurement base electrode tool, the patterned silver electrodes were evaporated on the PET or the glass substrate. The pattern had four electrodes with silver line thickness of 0.8 mm and a space distance of 0.6 mm. The silver pattern was loaded using thermal evaporation. The pressed Cu_3Sn layer samples of diameter of 5 mm were mounted onto a silver patterned PET substrate. And then 1kg weight was laid on the samples for uniform contact. A constant current of 10 mA was applied using a Keithley 224 current source and

voltage was measured for each experimental condition. In addition, the line patterned sample was measured to semiconductor parameter analyzer (Agilent 4155B) for the current-voltage characteristics.

3.2.4 Instrumentation and Measurements

HR-TEM images were captured using a JEOL JEM-3010 with an accelerating voltage of 100 kV. The HAADF-STEM, EELS analysis and EDS mapping images were obtained using a JEOL JEM 2100F. To make a the cross-sectional TEM sample, Focused Ion Beam (FIB) is used by NOVA 600 Nanolab(FEI). And then, the pressed sample was coated with a platinum-sputtering in order to protect the sample. The Pt coated cross-sectional TEM sample was loaded onto molybden TEM grid and conducted the TEM analysis. The XRD measurements were performed on the Bruker D8 DISCOVER diffractometer using a Cu Kα radiation source.

3.3 Results and Discussion

3.3.1 Analysis of synthesized Cu_3Sn alloy nanoparticles

The high resolution transmission electron microscopy (HRTEM) image in Figure 3.1a shows the round shapes of the Cu_3Sn alloy nanoparticles. The HRTEM image reveals that they have an average size of 60 nm. The X-ray diffraction (XRD) in Figure 3.1b shows that the Cu_3Sn alloy nanoparticles have a typical Cu_3Sn pattern (JCPDS 03-1010) in a dry powder sample. The major diffraction peaks at 2θ scattering angles agree with the hexagonal phase Cu_3Sn crystal. In addition, the Cu and Sn atoms ratio in the Cu_3Sn alloy nanoparticles is shown in Figure 3.1c through the energy dispersive spectrometer (EDS) diagram. The Cu and Sn peaks are clearly observed in the spectrum except for the sputtering materials Pt and Mo signals in the TEM grid. To verify the molar ratio of Cu and Sn, scanning transmission electron microscopy (STEM)-EDS point spectra analysis was performed on the Cu_3Sn nanoparticle. It showed that the molar ratio of Cu and Sn was 76.7:23.3. The analysis also conducted elemental distribution in the Cu-Sn alloy nanoparticles by carrying out an EDS elemental spectrum analysis with high angle annular dark-field scanning TEM (HAADF-STEM). Figure

3.1d and e show the high resolution EDS mapping of the Cu_3Sn nanoparticles, which are provided in the Cu (yellow) and Sn (red) distribution in each Cu_3Sn nanoparticle. These images confirm the well-distributed alloy state of the Cu_3Sn nanoparticles and show that there is no core-shell or uneven bimetallic structures in the Cu_3Sn nanoparticles. All images in Fig. 3.1 strongly confirm the homogeneous Cu_3Sn alloy nanoparticle formations.

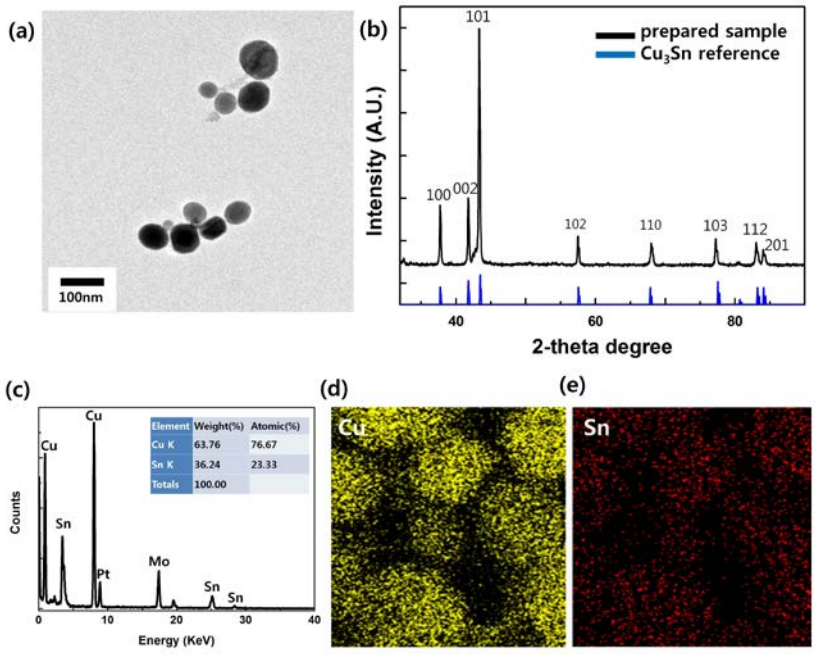

Figure 3.1 (a) TEM image of the synthesized Cu_3Sn nanoparticles with an average size of 60nm (b) XRD data of synthesized Cu_3Sn nanoparticles compared with Cu_3Sn reference peak (JCPDS 03-1010) (c) EDS spectrum of Cu_3Sn nanoparticles with Cu:Sn at 76.67 : 23.33 (d) The HAADF-STEM image and EDS mapping images of the Cu-Sn alloy (Cu_3Sn) nanoparticles.

3.3.2 Fabrication and Mechanism analysis of Cu_3Sn electrodes

Generally, the electrical resistivity of electrodes fabricated using nanoparticles is governed by two factors: the intrinsic metal resistivity and the residual surface layers induced by the capping agents. These affect the electron hopping and tunnelling, respectively.[21] The conductive metal nanoparticle core has many free electrons and act like bulk metal, which has a low electrical resistivity. Therefore, the residual surface layer induced by the capping agents is the most dominant factor in electron transport, so the electron transport mostly depends on the tunnelling phenomenon. Meanwhile, Shaowei Chen et. al. reported that the electrical characteristics of metal nanoparticle layers dramatically change in the “metallic ohmic contact” state by controlling the neighboring particle distance.[22,23] In that study, the simple linear I-V behaviour was observed when the neighboring particle distance was sufficiently small. This phenomenon implies that a small gap between adjacent nanoparticles can lead to electron hopping like metallic ohmic contact in electron transport between nanoparticles.

Based on the previous reports, the conductive electrodes fabrication at room temperature was attempted using the pressure-assisted method with Cu_3Sn alloy nanoparticles. The small gap between Cu_3Sn alloy

nanoparticles induced by pressure on a sample could confirm electron hopping as with metallic ohmic contact in electron transport between Cu_3Sn alloy nanoparticles. This would considerably improve the electrical resistivity of the Cu_3Sn alloy nanoparticles layer. The fabrication method is detailed in Figure 3.2a. A patterned shielding layer (3M tape) was first attached to the poly ethylene terephthalate (PET) substrate to prevent Cu_3Sn alloy nanoparticle powder spreading on unwanted space. The Cu_3Sn alloy nanoparticle powders were loaded on the patterned PET substrate and pressed for 3 min with a covered upper layer. After pressing, the shielding layer and upper layer were removed from the PET substrates. The conductive metal electrode pattern was well-developed in the flexible PET substrates.

The resistivity of the pressed Cu_3Sn alloy nanoparticles layers, ~ 19.8 μΩ·cm, is similar to that of the conventional conductive electrodes fabricated using pure copper or silver nanoparticles ink at a high temperature and inert gas sintering process.[18,19,20] Because the neighboring particle distance is small enough to result in metallic ohmic contact between the Cu_3Sn alloy nanoparticles, the pressed Cu_3Sn alloy nanoparticles resistivity is mainly determined by electron hopping. The pressure, which is a controlling factor for neighboring particle distance, induces the sequential

transition by electron hopping and ultimately leads to the low electrical resistivity. To verify this assumption, current–voltage (I-V) characteristic and cross-sectional TEM analysis of the pressed Cu_3Sn nanoparticle layer are conducted. The I-V characteristics of the pressed Cu_3Sn layer at 131.3 MPa are shown in Figure 3.2b. The linear shape indicates that the Cu_3Sn nanoparticle connections are very close enough to result in “metallic ohmic contact”. Figure 3.2c shows the three-dimensional the pressed Cu_3Sn nanoparticles contact in bright and dark field cross-sectional TEM images. In particular, Figure 3.2d shows the very close connections among neighboring Cu3Sn nanoparticles. The residual carbon on the Cu_3Sn nanoparticles surface is traced by TEM-electron energy loss spectroscopy (EELS) element mapping, as shown in Figure 3.2e. To ensure the fidelity of carbon element mapping by EELS, I verified the coincidence between the EELS spectrum of the carbon π^* and σ^* peak in Cu_3Sn nanoparticles and that of reference data. (Fig. 3.3) Elemental analysis of the carbon in Cu_3Sn nanoparticles confirms the carbon stabilizer distribution and shows that the carbon element is almost non-existent in the neighboring Cu_3Sn alloy nanoparticle interface. As a result, the pressure induced numerous three-dimensional close contact points among the Cu_3Sn nanoparticles and developed overall low electrical resistivity via metal ohmic contact.

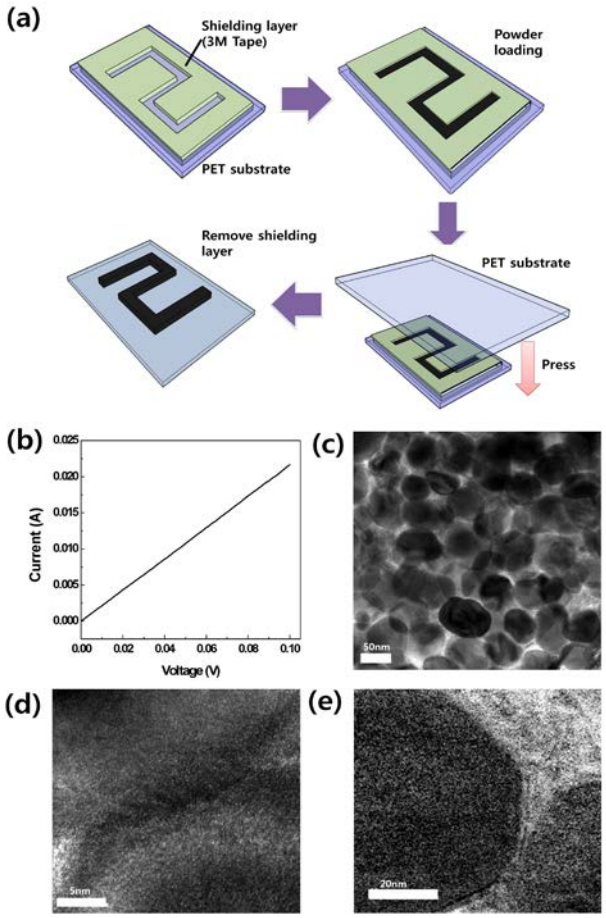

Figure 3.2 (a) Schematic of pressure-assisted Cu_3Sn nanoparticle electrodes fabrication. (b) I-V curve of Cu_3Sn nanoparticles electrodes at a 131.3 MPa pressure condition, which correspond with conventional ohmic contact electron transport (c) Cross-sectional TEM images of pressed Cu_3Sn nanoparticle electrodes at 131.3 MPa pressure condition. (d) The enlarged cross-sectional TEM view of pressed Cu_3Sn nanoparticles. (e) TEM-EELS elemental mapping that show the carbon (white) elements.

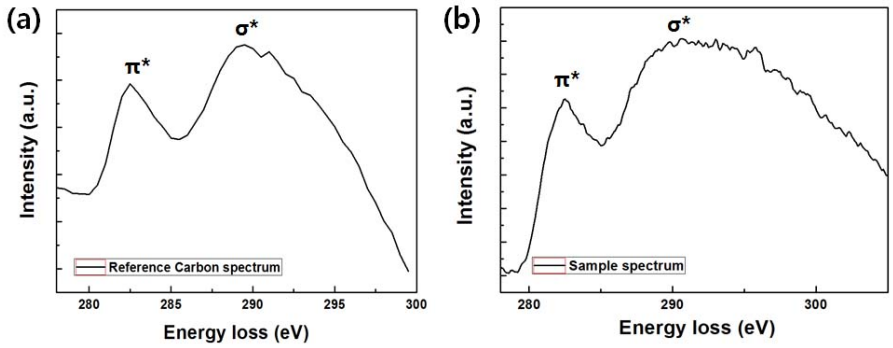

Figure 3.3 A typical EELS spectrum (a) carbon reference, (b) carbon spectrum of the pressed Cu_3Sn alloy nanoparticles, corresponding TEM-EELS elemental map (Figure 3.2e)

3.3.3 Conductive characteristics of Cu_3Sn electrodes

The resistivity of the pressed Cu_3Sn nanoparticles layer is measured using a four-point probe method. Figure 3.4a and Table 3.1 show the electrical resistivity of the pressed Cu_3Sn nanoparticles layers fabricated under various pressure conditions. The resistivity decreases from 25 μΩ·cm at 39.4 MPa to 19.8 μΩ·cm at 131.3 MPa. When the pressure exceeds 131.3MPa, the resistivity is saturated to approximately ~ 20 μΩ·cm, which is 2.2 times greater than the intrinsic resistivity of bulk Cu_3Sn (8.8 μΩ·cm). These results show that the electrical resistivity of the pressed Cu_3Sn nanoparticle layer is sufficiently low enough to behave as an electrical conducting layer (electrode), even though the pressed layer is developed at room temperature. Many ink jet printing studies on Ag and Cu nanoparticles have reported that the resistivity is between 5 ~ 40 μΩ·cm at a sintering temperature from 150 ^{o}C to 400 ^{o}C.[18,19,20] Although the resistivity of bulk Ag (1.47 μΩ·cm) and Cu (1.7 μΩ·cm) is five to six times lower than that of the bulk Cu_3Sn, the resistivity of the conductive pattern fabricated by pure Cu or Ag nanoparticle ink shows that are similar to that of the pressed Cu_3Sn nanoparticle electrode.

In addition, the pressed Cu_3Sn electrode could be formed on flexible

substrates like plastic or paper substrates because the fabrication process only requires a simple pressing process at room temperature. Furthermore, the numerous neighboring particle contacts of pressed Cu_3Sn nanoparticle electrode confirm the low resistivity at various bending states. These close contacts between particles are assumed to be related to the intrinsic property of Sn metal such as outstanding adhesion characteristics with substrate.[24] The resistivity at various bending conditions is measured to show the potential as a flexible electrode. The bending test results in Figure 3.4b reveal that except for the deformed state at 3 mm radius, the flexible test is reliable for the electrodes until 5 mm radius. At 20 mm radius and 15 mm radius, the relative resistivity is twice the flat resistivity. When the radius reaches 10 mm and 5 mm, the relative resistivity becomes three times greater than the flat resistivity. At 3 mm radius, the values abruptly increase to 30 times due to the pressed Cu_3Sn nanoparticle interconnection tearing. Figure 3.4c and Fig. 3.4d show the optical photographs of the Cu_3Sn electrodes fabricated by this pressure-assisted method. The images indicate the presence of well-patterned electrodes on the flexible PET substrate, which are electron-conductive enough to turn on bright LEDs. For the micro-scale phase observation of the pressed Cu_3Sn electrodes, the pressed Cu_3Sn electrodes are analysed using the cross-sectional Scanning Electron

Microscopy (SEM) images (Fig. 3.5). The SEM image shows that the Cu_3Sn electrodes have well-packed layers with densely inter-contacted Cu_3Sn nanoparticles.

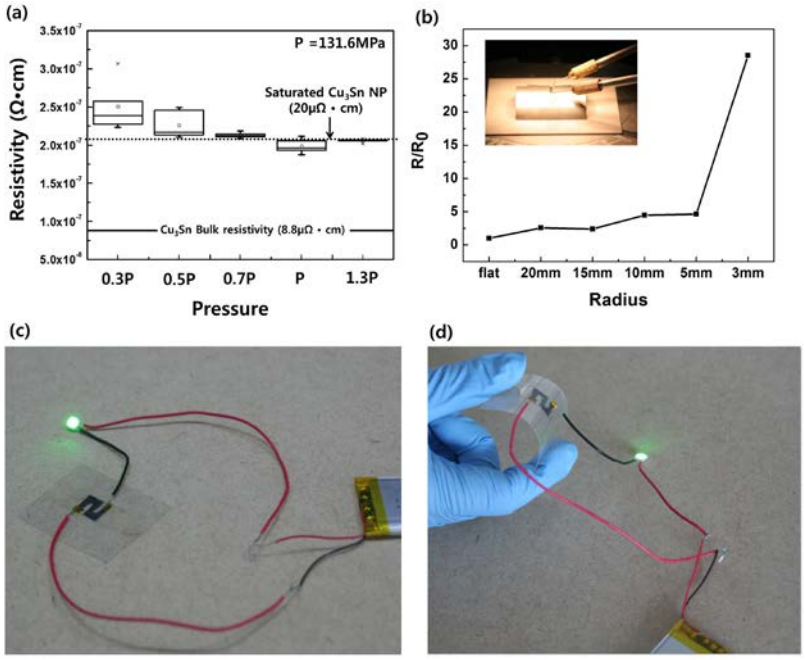

Figure 3.4 (a) Electrical resistivity of the pressed Cu_3Sn nanoparticles electrode as a function of pressure. The Cu_3Sn nanoparticles electrodes were fabricated at various pressures ranging from 39.4 MPa to 170.7 MPa. (b) Electrical resistivity of the pressed Cu_3Sn nanoparticles electrodes with varying bend radius, and a bending measurement image (inset). Optical images of the Cu_3Sn nanoparticles electrode pattern in a (c) flat state and (d) bent state.

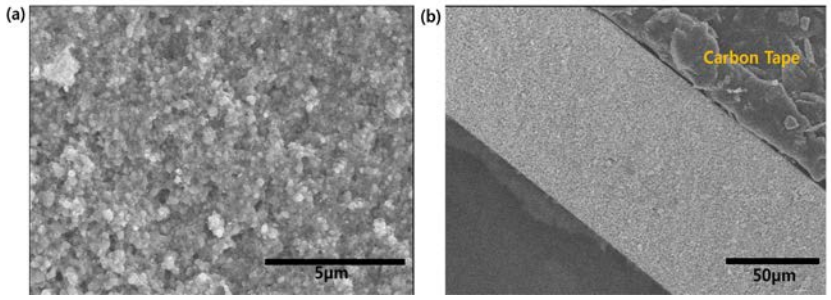

Figure 3.5 (a) Plane view SEM and (b) cross section SEM images of the pressed Cu_3Sn nanoparticles. The thickness of the pressed Cu_3Sn nanoparticles electrode is ~ 89 μm in 65.6 MPa.

3.3.4 Oxidation stability results of Cu_3Sn conductive electrodes

The good oxidation-resistivity of the Cu_3Sn nanoparticles are verified during 4 weeks. The oxidation-resistance of the Cu_3Sn alloy has been reported to be higher than that of Cu in its bulk material state.[25] Although nanostructured materials have somewhat different characteristics from bulk materials, I could easily assume that the oxidation-resistance trend was similar. To show the good oxidation-resistivity of the alloyed Cu_3Sn nanoparticles, the pressed Cu_3Sn nanoparticles electrode resistivity was monitored for 4 weeks under 50% relative humidity at 25 ^{o}C. (Figure 3.6) The XRD analysis in Figure 3.6a indicates that the copper oxide and tin oxide peaks are almost non-existent even after 4 weeks. However, the metal nanoparticle has generally an amorphous oxide layer and the synthesized Cu_3Sn alloy nanoparticles also have a native oxide layer. (Figure 3.7) Although the Cu_3Sn alloy nanoparticles have an oxide layer that is less than a few nanometers, the oxidation characteristics are considerably different when with Cu nanoparticles. The native oxide layers of the Cu nanoparticle diffuse into internal crystal structures. The diffused oxygen in Cu nanoparticles deform the intrinsic crystal structures like copper oxide and

hollow structures.[26,27,28] However, Cu_3Sn alloy nanoparticles shows constant oxygen ratio in EDS analysis (Figure 3.8a, b) and constant crystal structure in the SAED pattern (Figure 3.8c, d) irrespective of storage time for 4 weeks. Furthermore, Fig. 3.6b shows the constant resistivity of the pressed Cu_3Sn nanoparticle electrodes even after 4 weeks. These results reveal that the oxidation-resistance of the Cu_3Sn alloy nanoparticles is superior to that of the pure Cu nanoparticles. [26,27,28]

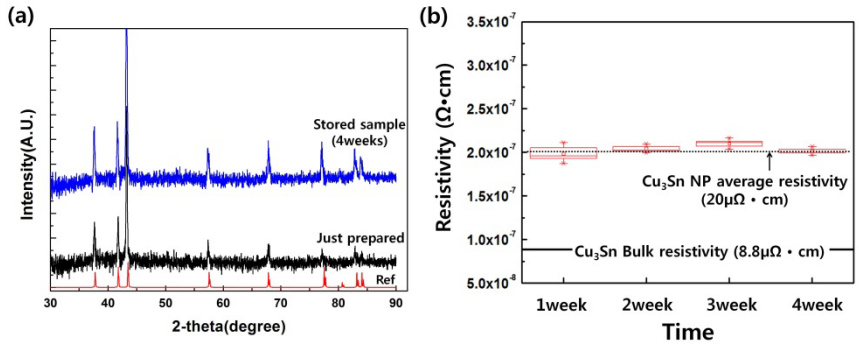

Figure 3.6 (a) XRD patterns of the synthesized Cu_3Sn alloy nanoparticles; just fabricated and stored in ambient air conditions (RH 50%, 25 oC) for 4 weeks (b) The resistivity variation of the electrodes fabricated by pressured Cu_3Sn alloy nanoparticles corresponding to the stored time in ambient air conditions

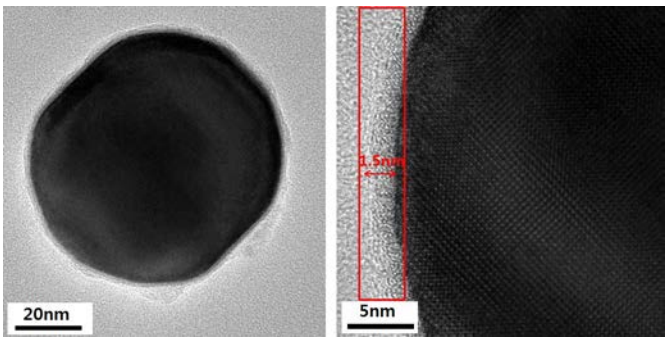

Figure 3.7 HR-TEM image of Cu_3Sn alloy nanoparticles and the red line indicate the oxide layer and the oxide layer thickness is measured to 1.5nm

(a) Just Synthesized

Element	Wt%	Atomic %
O	2.80	11.91
Cu	65.37	69.88
Sn	31.83	18.22
Total:	100.00	100.00

(b) After 4week

Element	Wt%	Atomic %
O	2.82	12.27
Cu	60.30	66.09
Sn	36.88	21.64
Total:	100.00	100.00

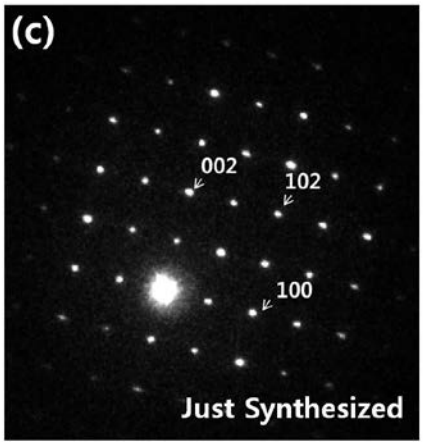

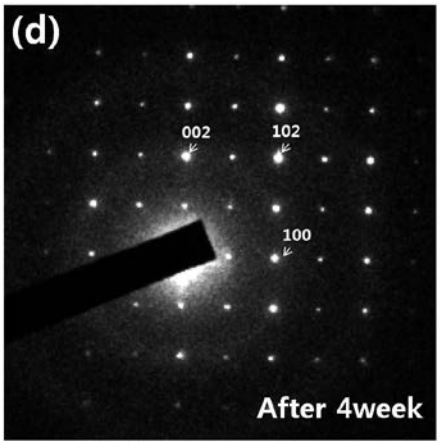

Figure 3.8 EDS analysis of (a) just synthesized Cu_3Sn alloy nanoparticles and (b) stored in ambient air condition (RH 50%, 25 ^{o}C) for 4 weeks The SAED pattern analysis of the Cu_3Sn alloy nanoparticles compared with the stored time in (c) just synthesized nanoparticles and (d) stored in ambient air condition (RH 50%, 25 ^{o}C) for 4 weeks

3.4 Conclusion

In conclusion, a new synthesis of the highly oxidation stable Cu-Sn alloy (Cu_3Sn) nanoparticles is introduced using a simple one-pot reaction. The synthesized Cu_3Sn nanoparticles had an average diameter of 60 nm. Compared to Cu, Ag, and other nanoparticles, the Cu_3Sn nanoparticles had the promising electrode properties such as oxidation-resistivity, low cost materials, simple process-ability, and room temperature electrode fabrication-ability, as an electrode material. In particular, the Cu_3Sn nanoparticles did not show appreciable oxide impurities even when left in contact with air for 4 weeks under ambient conditions (RH 50%, 25 oC). The electrical resistivity of the pressed Cu_3Sn nanoparticles layer also showed little change after 4 weeks. This oxidation-resistance confirmed that the Cu_3Sn nanoparticles could easily be used for electrode materials without needing any cumbersome storage conditions. In addition, a pressure-assisted electrode fabrication method is proposed using Cu_3Sn nanoparticles, which has suitable electrical resistivity for a conductive line. The electrical resistivity of the pressed Cu_3Sn nanoparticles electrode was 19.8 μΩ·cm at 131.3 MPa. Consequently, the pressure considerably helps connect the Cu_3Sn nanoparticles at room temperature and effectively induces low

electrical resistivity in Cu_3Sn nanoparticle electrodes. This pressure-assisted electrode fabrication technique has several advantages over previous printing fabrications. The fabrication does not require any cumbersome processes such as the ink formulations optimization with viscosity, solids content, and solvent type. There are also potential cost advantages due to the use of low cost materials and simple non-vacuum processing conditions. Furthermore, room temperature fabrication enables the use of flexible devices based on plastic substrates. I believe that the high oxidation-resistance of Cu_3Sn alloy nanoparticle synthesis and the pressure-assisted electrode fabrication process induce a leap in conventional electrode fabrication methods and they have good potential for various functional devices on a plastic substrate.

References

[1] S. Alayoglu, A. U. Nilekar, M. Mavrikakis, B. Eichhorn, *Nat. Mater*., 2008, **7**, 333.

[2] S. H. Zhou, B. Varughese, B. Eichhorn, G. Jackson, K. McIlwrath, *Angew. Chem. Int. Edit.*, 2005, **44**, 4539.

[3] D. S. Wang, Y. D. Li, J. Am. Chem. Soc**.**, 2010, **132**, 6280.

[4] S. Link, Z. L. Wang, M. A. El-Sayed, *J. Phys. Chem. B.*, 1999, **103**, 3529.

[5] H. Jiang, K. S. Moon, F. Hua, C. P. Wong, *Chem. Mater*., 2007, **19**, 4482.

[6] Q. J. Guo, H. W. Hillhouse, R. Agrawal, *J. Am. Chem. Soc.*, 2009, **131**, 11672.

[7] C. M. Andolina, A. C. Dewar, A. M. Smith, L. E. Marbella, M. J. Hartmann, J. E. Millstone, *J. Am. Chem. Soc.*, 2013, **135**, 5266.

[8] S. Jeong, H. C. Song, W. W. Lee, S. S. Lee, Y. Choi, W. Son, E. D. Kim, C. H. Paik, S. H. Oh, B. H. Ryu, *Langmuir*, 2011, **27**, 3144.

[9] J. Perelaer, P. J. Smith, D. Mager, D. Soltman, S. K. Volkman, V. Subramanian, J. G. Korvink, U. S. Schubert, *J. Mater. Chem.*, 2010, **20**, 8446.

[10] D. L. Schodek, P. Ferreira, M. F. Ashby, Nanomaterials, nanotechnologies and design: an introduction for engineers and architects, Butterworth-Heinemann, 2009.

[11] J. S. Kang, H. S. Kim, J. Ryu, H. T. Hahn, S. Jang, J. W. Joung, J. Mater. Sci.: *Mater. Electron.*, 2010, **21**, 1213.

[12] S. Gamerith, A. Klug, H. Scheiber, U. Scherf, E. Moderegger, E. J. W. List, *Adv. Funct. Mater.*, 2007, **17**, 3111.

[13] M. Grouchko, A. Kamyshny, S. Magdassi, *J. Mater. Chem.*, 2009, **19**, 3057.

[14] S. Magdassi, M. Grouchko, A. Kamyshny, *Materials*, 2010, **3**, 4626.

[15] C. Kind, A. Weber, C. Feldmann, *J. Mater. Chem.*, 2012, **22**, 987.

[16] Z. C. Xu, C. M. Shen, Y. L. Hou, H. J. Gao, S. S. Sun, *Chem. Mater.*, 2009, **21**, 1778.

[17] V. Zardetto, T. M. Brown, A. Reale, A. Di Carlo, *J. Polym. Sci. Pol. Phys.*, 2011, **49**, 638.

[18] Z. L. Zhang, X. Y. Zhang, Z. Q. Xin, M. M. Deng, Y. Q. Wen, Y. L. Song, *Nanotechnology*, 2011, **22**, 425601.

[19] K. Ankireddy, S. Vunnam, J. Kellar, W. Cross, *J. Mater. Chem. C*, 2013, **1**, 572.

[20] Y. Lee, J. R. Choi, K. J. Lee, N. E. Stott, D. Kim, *Nanotechnology*, 2008, **19**, 415604.

[21] C. P. Collier, T. Vossmeyer, J. R. Heath, *Annu. Rev. Phys. Chem.*, 1998, **49**, 371.

[22] S. W. Chen, *J. Mater. Chem.*, 2007, **17**, 4115.

[23] S. Pradhan, J. Sun, F. J. Deng, S. W. Chen, *Adv. Mater.*, 2006, **18**, 3279.

[24] S. Park, M. Yu, U. Lee, HG Lee, *Ceramist*, 2009, **12**, 85.

[25] H. Liu, K. Wang, K. Aasmundtveit, N. Hoivik, in Electronic Components and Technology Conference (ECTC), *2010 Proceedings 60th, IEEE*, 2010, 853.

[26] M. Yin, C. K. Wu, Y. B. Lou, C. Burda, J. T. Koberstein, Y. M. Zhu, S. O'Brien, *J. Am. Chem. Soc.*, 2005, **127**, 9506.

[27] M. Salavati-Niasari, F. Davar, *Mater. Lett.*, 2009, **63**, 441.

[28] S. U. Son, I. K. Park, J. Park, T. Hyeon, *Chem. Commun.*, 2004, **7**, 778.

Chapter 4. Self-reducible Copper ion complex ink for air sinter-able conductive electrodes

4.1 Introduction

Solution-processable electrode fabrication is a significant technology for electronic devices because it is a simple, low-cost fabrication process, with a reduced output of environmentally noxious chemical wastes.[1,2] Over the past several years, many researches have focused on the development of solution-processable electrode materials for advanced devices such as organic light emitting diode (OLED), solar cell, thin film transistor (TFT), radio-frequency identification (RFID) and printed circuit board (PCB).[3,4,5] In general, conductive polymers (e.g. poly(3,4-ethylenedioxythiophene):polystyrene sulfonate (PEDOT:PSS) and polyaniline) and carbon nanomaterials (e.g. single walled carbon nanotube (SWCNT), and reduced graphene oxide (RGO)) have been developed as solution-processable electrode material.[6,7,8,9] These materials have several advantages such as a high mechanical flexibility and adjustable electrical

properties. Nevertheless, carbon nanomaterials and conductive polymers as solution-processable electrodes have some crucial weakness such as their relatively high resistivity, the cumbersome manufacturing methods by the use of strong acids or bases, the long processing times and their limited compatibility with conventional electronic devices.[9,10] Besides, some drawbacks to electronic devices remain, such as the unnecessary energy consumption by a high resistivity, and the degradation of their thermal effects. Therefore, metal-based inks have recently attracted attention as low resistivity solution-processable electrodes.

Metal based inks, such as silver, copper, and nickel, have been widely researched as alternatives for carbon based materials.[11,12,13] Among the metal-based inks, research on silver (Ag) inks has flourished due to their low intrinsic resistivity (1.59 $\mu\Omega$ • cm) and high redox potential (high oxidation stability).[11,14] However, the high cost and a low electro-migration resistance of Ag are critical limitations for the use of Ag inks in various electronic applications. In this respect, copper (Cu) inks are fascinating materials for solution process materials, because of their low cost, high migration resistance, and excellent intrinsic electronic resistivity (1.7 $\mu\Omega$ • cm).[13,15] Unfortunately, one critical drawback of Cu inks is their low oxidation stability, which induces the inevitable oxidation of Cu and a high

film resistivity.[16] In general, Cu oxidation under electrode fabrication processes is affected by two main steps: storage and sintering.

In storage processes, to overcome oxidation, diverse approaches such as synthesis of alloy nanoparticles, core-shell (Cu-inert material) structure nanoparticles, and Cu ion complex inks (Cu-ink) have been attempted.[17,18,19] Through these efforts, Cu-inks have been verified to be highly stable storage materials, because they can maintain the monovalent, or divalent ion states of Cu in the ink.[20] However, in sintering process, they face harsh conditions for both the prevention of oxidation and reduction of the Cu ion. Conventional thermal sintering methods for the fabrication of conductive electrode using Cu-inks utilize dangerous gases (H_2, vaporized formic acid), inert gases (N_2) or vacuum conditions, which are dangerous, cumbersome, and make the electrode fabrication process time-consuming.[21,22] In addition, sintering processes that use dangerous gases and vacuum conditions negatively affect the environment. For example, vaporized gas can cause damage to humans, and increases the risk of an explosion in the sintering chamber. For this reason, a sintering process carried out in an air atmosphere is a critical issue for the solution-processable fabrication of Cu electrodes. For sintering methods under an air atmosphere, photonic, microwave, and chemical sintering techniques have

been recently studied; however, these sintering approaches require expensive equipment and complicated processes.[23,24] Recently, as an alternative, self-reducible inks have been proposed as ambient condition thermal sintering inks.[25,26,27] However, the general self-reducible ink produces Cu oxide films or still shows too high resistivity (~ > 300 μΩ • cm) for practical devices. This high resistivity is attributed to the weak reduction potential during air condition sintering. Consequently, although Cu-inks have air-sintering capabilities, there still remains a considerable challenge in the field of self-reducible Cu-inks.

To address these issues, a novel self-reducible Cu-ink, composed by formate, alkanolamine groups and poly alcohols, is introduced with a sufficient reduction potential to be sintered in air conditions. The co-reduction, induced by decomposition of the Cu-ink ligand and the hydroxyl group of polyol solvent acting as reduction assistance materials, gives the reduction process of the Cu-ink enough self-reducible activity. The decomposition of the Cu-ink ligands induces the formation of reducible hydrogen gas and the electron transfer of amine groups. In addition, the mild reduction potential by the hydroxyl group of the polyol solvents enables the Cu-ink to form metallic Cu even in ambient sintering conditions. The characteristics of the sintered Cu electrode films were analysed with

various sintering temperatures and polyol solvent contents. The Cu electrode film, fabricated using Cu-ink with 3 wt% glycerol, exhibited the lowest resistivity value of 17 μΩ • cm. The flexible property of the Cu electrode films retained a stable resistivity (R/R_0 <1.2, bending radius of 20 mm) even up to 2000 bending times. Also, the proposed Cu-ink showed good storage stabilities up to 4 weeks.

4.2 Experimental section

4.2.1 Chemicals & materials

Cu (II) formate tetrahydrate (98 %) was purchased from Alfa Aesar. Ethylene glycol (EG; 99.8 %), glycerol (99 %), triethylene glycol (TEG; 99 %), 2-amino-2-methyl-1-propanol (AMP; 95 %), 3-aminopropyl triethoxysilane (APTES; 98 %), octylamine (99 %), hydrazine (98 %) and sodium borohydride ($NaBH_4$; 99 %) were obtained from Aldrich. Methyl alcohol (99.5 %), isopropyl alcohol (99.5 %), diethylene glycol (DEG; 99 %) and polyethylene glycol 200 (PEG 200) were purchased from Daejung Chemicals. All reagents were used as received without any further purification.

4.2.2 Preparation and formulation of Cu-inks

The Cu-inks were synthesized as follows. First, 8.98 g of AMP and 11.45 g of octylamine were magnetically stirred for 30 min in a 250 mL round bottom flask. Thereafter, 20 mL of methyl alcohol and 20 g of Cu (II) formate tetrahydrate were poured into the 250 mL round bottom flask of containing the AMP and octylamine mixture. When the Cu (II) formate tetrahydrate was poured into the solution, the color of the solution immediately changed to a transparent blue. To obtain a well-dissolved solution, magnetic stirring was carried out for 1h. After the complete formation of the Cu ion complex, the obtained solution was dried with a rotary evaporator under reduced pressure, and then it was continuously dried in a vacuum chamber for 8 h at 50 ^{o}C. In this process, methyl alcohol and water were extracted from the Cu ion complex solution, and as a result, a dark blue colored, highly viscous complex was formed. To control of the viscosity, the Cu-ink and isopropyl alcohol (8:2 weight ratio) were mixed by sonication and vortex. The polyol solvent, (EG, glycerol, DEG, TEG, or PEG 200) was mixed with the intrinsic Cu-ink at concentrations ranging from 1 wt% to 15 wt%. To investigate the effect the polyol solvent had on Cu-ink, Cu-ink with polyol solvents (named as pCu-ink), and Cu-ink

without polyol solvents (named as intrinsic Cu-ink) are prepared. In particular, the Cu-ink with glycerol was named as gCu-ink. To test the adhesive enhancement effects, various contents of APTES were applied to the 3 wt % gCu-ink. Finally, for chemical affinity tests, a mixture of the intrinsic Cu-ink with different kinds of reduction assistance materials, such as hydrazine (N_2H_2) and sodium borohydride ($NaBH_4$), was formulated. All mixing processes were conducted for 1h using magnetic stirring.

4.2.3 Fabrication and mechanical reliability tests of conductive Cu electrode films made with Cu-ink

To fabricate the conductive Cu electrode films, the substrates were first heated on a hot plate and then the Cu-ink was added (as a droplet) onto the heated substrates. The Cu-ink droplet spread on the entire substrate, and the ink was sintered until completely evaporated. The electrode film was then sintered at a 200-350 ^{o}C temperature range in an air atmosphere. To make a line-shaped Cu film, the Cu-ink with 3 wt% glycerol was loaded onto the PEN substrate, and sintered at 200 ^{o}C. The ink loading using micro pipette was carefully conducted. The fabricated Cu electrode film on the PEN film substrate was used for mechanical reliability test (flexible test), which were

carried out by repeated bending of the sample using a 20 mm bending radius. After bending experiment, the linear resistance was measured with every 500 cycles for 2000 cycles. In addition, the adhesive strength of the film was evaluated by 3M Tape (#810) peel-off test. The experiment was repeated 10 times.

4.2.4 Characterization

The X-ray diffraction (XRD) patterns of the sintered Cu powder were measured with a New D8 Advance diffract meter (Bruker), in reflection geometry mode using Cu Kα radiation (1.5406 Å). The surfaces of the samples after sintering of the Cu-ink were investigated by X-ray photoelectron spectroscopy (XPS; AXIS-HSi, KRATOS). The surface morphology of the films was analyzed by scanning electron microscopy (SEM; Hitachi S- 4800). The sheet resistance was measured using the van der Pauw method (Keithley 617 system as source meter with a four point probe configuration), and its thickness was confirmed with a surface profiler (Alpha-Step IQ, KLA Tencor). The specific resistivity was calculated from the measured thickness and sheet resistance. This step was repeated five times, and the average values are reported in this paper.

4.3 Results and discussion

4.3.1 Polyol assisted air sinter-able Cu electrode formation

Scheme 4.1 shows the Cu-ink chemical structure and reduction mechanism, and photograph image of Cu electrode films on glass substrates. In sintering process, the Cu-ink with polyol solvents (pCu-ink) was reduced to a metallic Cu film by the co-reduction of the polyol solvent and the self-reducible Cu-ink. During the sintering process, the intrinsic self-reducible Cu-ink produces the reducible hydrogen gas (H_2) through the decomposition of the Cu (II) formate group. The amine groups of Cu-ink also have a mild reduction potential because of the amine's electron transfer ability.[26,27] The self-generated H_2 gas and amine groups act as reduction agents, and facilitate the self-reduction of the Cu-ink. However, this self-reducible property is not enough to ensure sintering under air condition, and thus inert N_2 gas is needed to prevent the oxidation of the intrinsic Cu-ink during sintering process. As displayed in Scheme 4.1, it was easily confirmed that the intrinsic Cu-ink was able to form the Cu oxide film under ambient sintering conditions by the gray color of the film. For this

reason, polyol solvents are added to intrinsic Cu-ink, which is pCu-ink, for providing a further reduction assistant-ability. The sintered Cu electrode film by pCu-ink showed a typical Cu metal color, as can be observed in Scheme 4.1(a). In these phenomena, the pCu-ink successfully reduced the Cu electrode film under air sintering conditions due to the hydroxyl groups of the polyol solvents, which provide a mild reduction potential during the process. (Scheme 4.1(b)) This reduction property of polyol solvents is well known in the synthesis of nanoparticles.[28] On basis of this phenomenon, the air sinter-able Cu ink with polyol solvents (pCu-ink) is newly designed using the self-reducible property of ion complex decomposition.

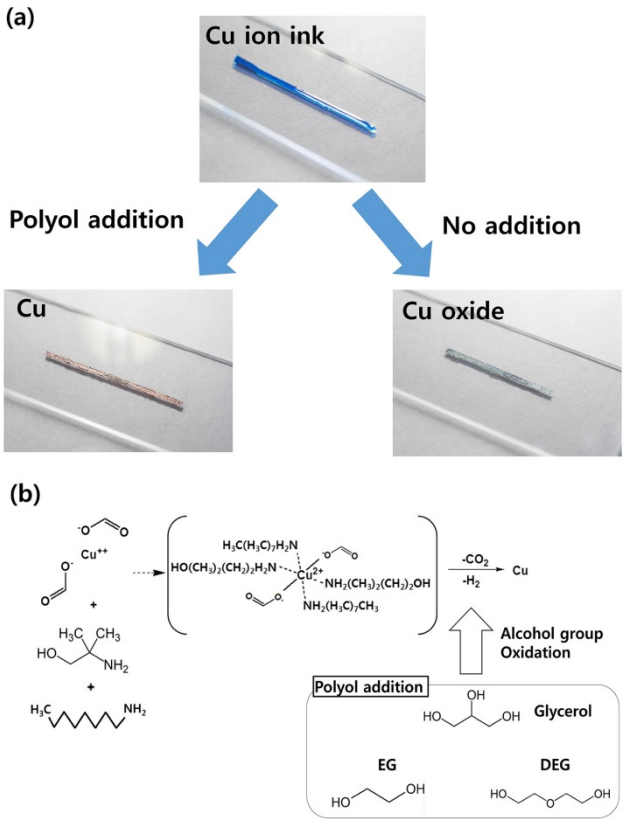

Scheme 4.1 (a) Photograph image of the formation of Cu electrode films on glass substrates. (b) Schematic illustration of Cu-ink chemical structure and pCu-ink reduction mechanism. The pCu-ink was reduced to a metallic Cu film by the co-reduction of polyol solvents and the self-reducible properties of the Cu-ink.

As mentioned above, the polyol solvents efficiently assisted the reduction of the Cu-ink under an air atmosphere, and minimized the formation of Cu oxide. Figure 4.1a shows X-ray diffraction (XRD) results of sintered Cu electrode films by pCu- ink at 300 ^{o}C. These pCu-inks contained different polyol solvents, at a 3 wt% concentration, such as ethylene glycol (EG), diethylene glycol (DEG) and glycerol. The sintered Cu electrode films made with the pCu-ink showed a typical Cu reflection pattern (JCPDS 03-1018). The three major 2θ peaks were 43.5^{o}, 50.7^{o} and 74.4^{o}, which were assigned to the {111}, {200}, {220} planes of face-centered cubic (fcc) structures, respectively. In the sintered Cu electrode film, only metallic Cu was existed, and oxidized substances, such as Cu (I) oxide or Cu (II) oxide, were not detected. Likewise, sintered Cu electrode films made using pCu-ink with EG, DEG and glycerol showed the stable reduction assistance effect by polyol solvents. However, as can be observed in Figure 4.1b, the sintered Cu electrode films made using pCu-ink with 3wt % tetra ethylene glycol (TEG) and poly ethylene glycol 200 (PEG 200) showed, in addition to the Cu peak, the slight appearance of Cu_2O (2θ = 36.4^{o}). The slight Cu_2O peak could possibly be explained by the weak reduction potential induced by the low number of hydroxyl groups in the molecular structures of TEG and PEG 200, in comparison with the structures of EG, DEG, and glycerol.

Although the slight Cu_2O was formed by the weak reduction potential of TEG and PEG 200, the results of the well-reduced Cu electrode film using EG, DEG and glycerol shows the good evidence of their reduction assistance effect under air sintering conditions.

In general, Cu films inevitably form a native oxide layer on their surface because of their high reactivity with oxygen. To detect, in-detail, the existence of this native oxide structure, the sintered Cu electrode films made using the 3 wt% EG pCu-ink were analysed by X-ray photoelectron spectroscopy (XPS). Figure 4.1c shows the peak fitted Cu $2p_{3/2}$ and Cu $2p_{1/2}$ spectra of the Cu electrode films, which confirm the presence of pure Cu and the slight Cu_2O surface layer. The fitted Cu $2p_{3/2}$ binding energies of pure Cu and Cu_2O were 932.1 eV and 933.0 eV, respectively.[29,30] From these analyses, it was concluded that, while the core of the film was well reduced to metallic Cu, the surface of the Cu film had an amorphous native Cu_2O layer. Although the native oxide layer generally increases the resistivity of the films, the sintered Cu electrode film made using pCu-ink showed a low resistivity due to the amorphous native oxide layers having formed after the Cu inter-particles had been fully connected.[29]

Depending on the kind of polyol solvents, the resistivity tendency of the sintered Cu electrode films was investigated at 300 ^{o}C (Figure 4.1d). The

measured specific resistivity of sintered Cu electrode films made using pCu-inks with 3 wt % EG, glycerol, DEG, and TEG were 37.9, 29.9, 34.1, and 36.5 μΩ • cm, respectively. At 300 ^{o}C sintering temperature, the sintered Cu electrode film made using pCu-ink with EG and DEG exhibited the lower resistivity than the sintered Cu electrode film made using pCu-ink with TEG. During the sintering process, TEG leaves unnecessary organic residues at their high evaporation temperatures (> 300 ^{o}C) and induces a low reduction potential by a low number of hydroxyl groups in their molecular structures. (Figure 4.1d) These effects induced a high resistivity in the Cu electrode film. On the other hand, EG and DEG have a high reduction potential because of the abundant hydroxyl groups in their molecular structures, and show an easy removal of residues by proper evaporation temperature (<~300 ^{o}C). Particularly, the sintered Cu electrode film made using Cu-ink with glycerol (gCu-ink) showed the lowest resistivity value. This result is due to glycerol having the most optimum characteristics among the proposed polyol solvents, such as a reasonable evaporation temperature (<~300 ^{o}C), and a relatively high reduction potential. Therefore, the characteristics of sintered Cu electrode film made using gCu-ink are investigated as the optimized sintering condition.

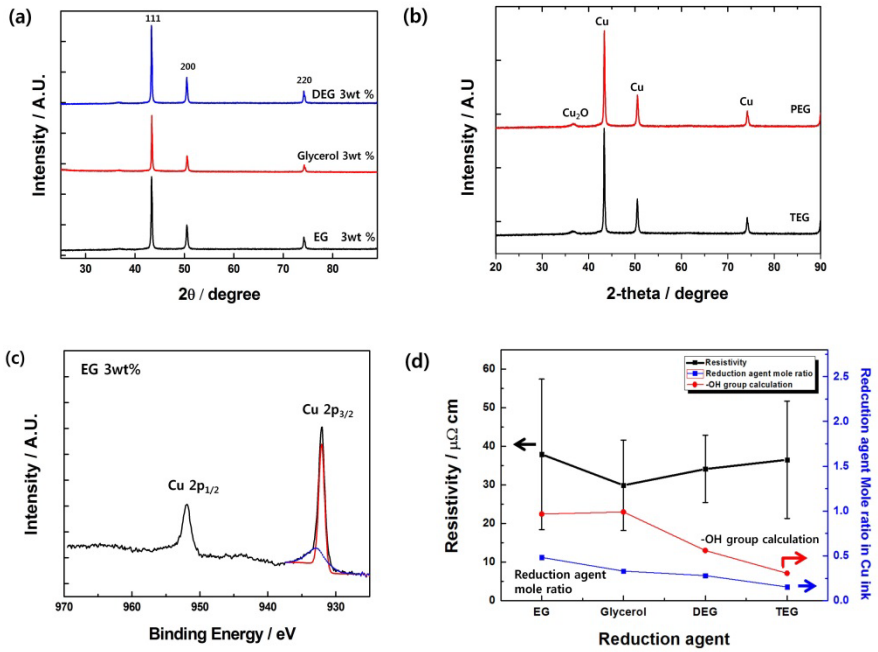

Figure 4.1 Characteristics of sintered Cu electrode film made using different 3 wt% pCu-ink at 300 ^{o}C; (a),(b) XRD pattern of sintered Cu film by various kinds of pCu-ink, (c) XPS spectra of the sintered Cu electrode film made using 3 wt% EG pCu-ink, and (d) Comparison of the reduction assistant solvent mole ratio and specific resistivity of sintered Cu electrode films by pCu-ink

4.3.2 Cu film properties by sintering temperature difference

Fig. 4.2a shows the specific resistivity of the sintered Cu electrode film made using the gCu-ink as a function of temperature. In air sintering conditions, the specific resistivity of the Cu electrode film were 475, 76.6, 29.9, 17 μΩ • cm at 200, 250, 300 and 350 ^{o}C, respectively. At temperatures above 350 ^{o}C, Cu oxide was formed by fast evaporation of the glycerol, and the resistivity measurements of the Cu electrode film were not conducted. Also, for stable decomposition of the Cu-ink, the sintering process proceeded within the 200 ^{o}C - 350 ^{o}C.[26] Finally, I achieved the low resistivity with 17 μΩ • cm of Cu electrode film made using gCu-ink, which is a value similar to the best resistivity obtained for sintered Cu electrode film made using reducing gas conditions, such as H_2 and vaporized formic acid, or vacuum condition.[14,19,22,31,32,33,34,35] Therefore, the resistivity of sintered Cu electrode film made using gCu-ink is very competitive, because the gCu-ink sintering process does not require the use of dangerous gases (H_2), ambient gases (N_2) or high-cost equipment, such as laser sintering and vacuum condition equipment.

According to the results, the specific resistivity showed a noticeable

increasing tendency dependent on decrease in the sintering temperature. This phenomenon could be doubted as the formation of defective Cu crystals or Cu oxide crystals. For this reason, XRD measurements are utilized to confirm the crystal formation on the sintered Cu electrode film at low temperatures. In Figure 4.2b, the XRD peaks of the sintered Cu electrode film at 200 ^{o}C matched with the peak of pure Cu, indicating the formation of reduced Cu electrode films at relatively low temperatures. Therefore, the formation of Cu oxide or defective Cu crystals was not an appropriate reason for the observed resistivity tendency. Scanning electron microscopy (SEM) was conducted to find evidence for the resistivity tendency. Figrue 4.2 c,d,e, and f shows the effect of the ink decomposition temperature on the surface morphologies of sintered Cu electrode films. With increasing temperature, the Cu particles had good coalescence with neighboring particles. The good connectivity of the particles induced the observed decrease in resistivity, which was well consistent with the SEM results.

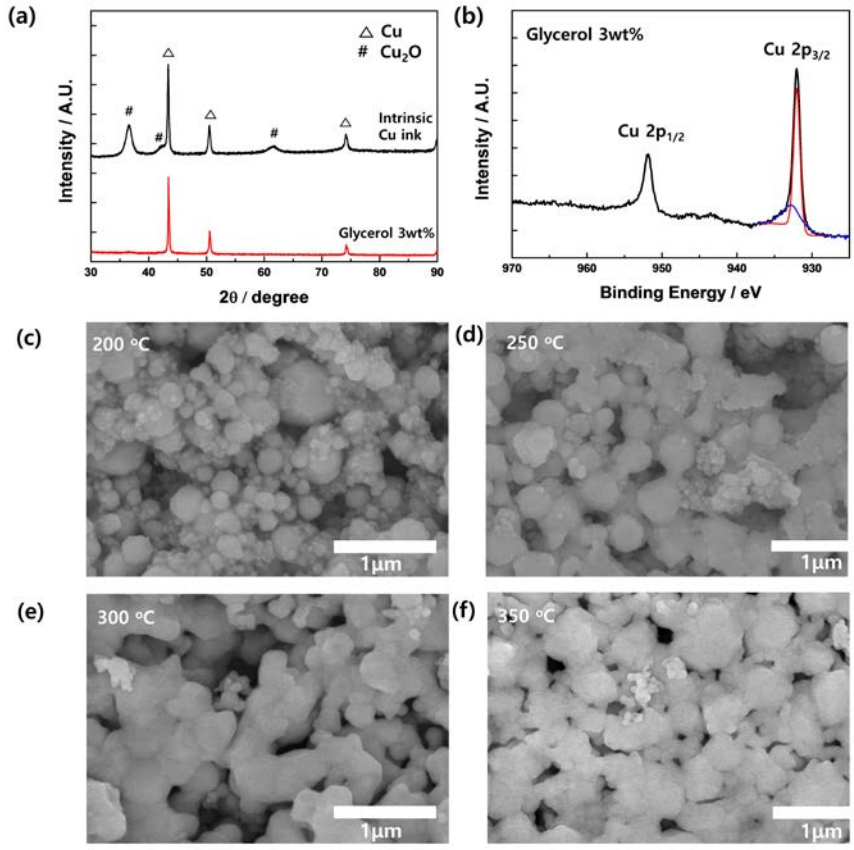

Figure 4.2 Characteristics of the sintered Cu electrode film made using 3 wt% gCu-ink; (a) Temperature dependent of the specific resistivity, (b) XRD spectrum of the film sintered at 200 ^{o}C**.** Surface morphologies of the sintered Cu electrode films made using 3 wt% gCu-ink at (**c**) 200 ^{o}C, (**d**) 250 ^{o}C, (**e**) 300 ^{o}C and (**f**) 350 ^{o}C

Based on the resistivity results, I needed to verify the crystal formation of metallic Cu and the existence of an oxidized substance at 350 ^{o}C. As shown in the XRD data (Figure 4.3a), the sintered Cu electrode film made using 3 wt % gCu-ink showed typical Cu metal fcc structures, indicating its good reduction to a Cu crystal even under air sintering conditions. In addition, through comparisons of sintered Cu electrode film by the intrinsic Cu-ink at 350 ^{o}C, the reduction properties of glycerol were verified. In Figure 4.3a, the sintered Cu electrode film made using the intrinsic Cu-ink showed Cu_2O impurities at36.4^{o}, 42.3^{o} and 61.3^{o} corresponding to the {111}, {200} and {220} crystal planes, respectively. These results were ascertained by XPS analysis of the surface oxidation. Figure 4.3b shows the fitted spectra of the sintered Cu electrode film made using 3wt % gCu-ink, which was matched with the 932.1 eV (Cu $2p_{3/2}$) and 932.9 eV (Cu_2O) binding energies. The identified Cu_2O XPS spectra involved the amorphous native oxide layer of the Cu electrode film surface after the Cu inter-particles were fully connected. Thus, the amorphous native oxide layer at the Cu surface did not significantly affect the resistivity of the Cu films. The Cu spectrum of the sintered Cu electrode film indicates that the gCu-ink was reduced into a Cu electrode film even at the high temperature of 350 ^{o}C under air sintering conditions. Otherwise, in Figure 4.4, the XPS spectra of the sintered Cu

electrode film made using intrinsic Cu-ink showed a noticeable CuO spectra feature, which corresponded to the typical CuO spectra of two strong satellite Cu^{2+} peak: Cu $2p_{3/2}$ (934.1 eV) and Cu $2p_{1/2}$ (954.0 eV).[36] Consequently, these results show that the addition of the polyol solvents, specially glycerol, minimizes the oxidation of Cu during air sintering conditions, and fully assists in the reduction of the Cu-ink even at a high temperature of 350 ^{o}C.

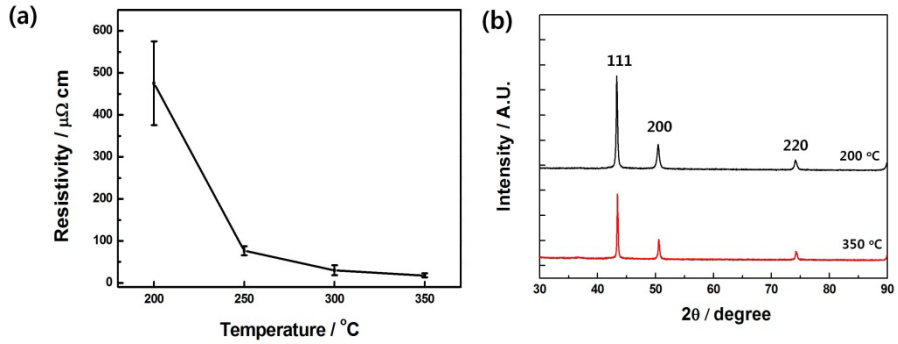

Figure 4.3 (a) XRD spectrum of the film of sintered Cu electrode film made using intrinsic Cu-ink and 3 wt% gCu-ink at 350 ^{o}C, and (b) XPS Cu 2p spectra analysis of the sintered Cu electrode film made using 3 wt% gCu-ink

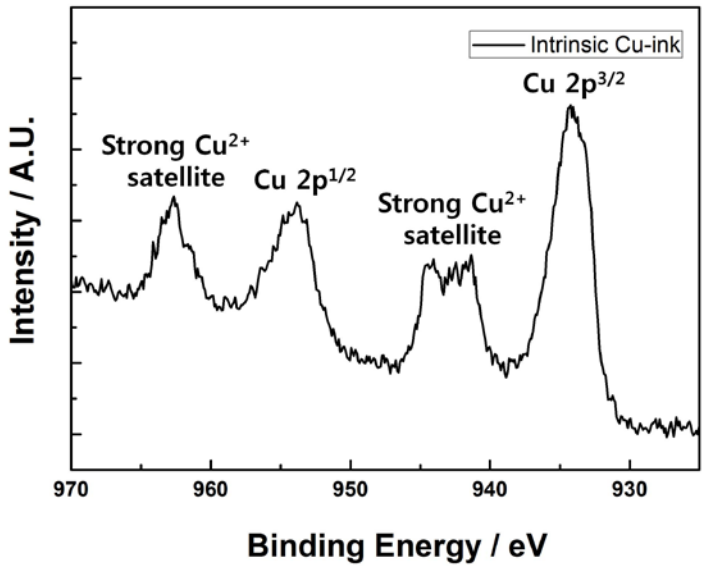

Figure 4.4 XPS Cu 2p spectra of the sintered Cu electrode film at 350 ^{o}C with the intrinsic Cu-ink

4.3.3 Polyol solvent weight dependent characteristics of air-sintered Cu electrode

The polyol solvents used to provide reduction assistance effects were identified by various analytical methods, as seen in Figure 4.1 - 4.4. In these results, the polyol solvents served critical roles during the sintering process, such as reducing the Cu electrode film. Thus, the content of polyol solvents was also related to the characteristics of the conductive electrode films. In Figure 4.5a and b, the effect of the glycerol contents (wt % and mole ratio) was investigated through resistivity tests at 350 ^{o}C. The resistivity of sintered Cu electrode film made using gCu-ink showed a linear increasing tendency depending on the high glycerol content. The tendency of resistivity is basically the same in wt % and mole ratio results. The sintered Cu electrode film made using 3 wt% gCu-ink had the lowest resistivity measured of 17 μΩ • cm; whereas the sintered Cu electrode film made using 15 wt% gCu-ink had a relatively high resistivity of 54.8 μΩ • cm. High glycerol contents, over 3 wt%, induced the incomplete decomposition of organic materials, which acted as insulator of the electron conducting path. For this reason, it was best to add small amounts of glycerol to the Cu-ink. However, small amounts of glycerol content could induce the

formation of Cu oxide crystals, and a high resistivity due to the low reduction potential. That being so, the characteristic of Cu electrode film by relatively low glycerol contents, less than 3 wt%, needs to be investigated.

To verify the existence of Cu oxide in Cu electrode films, XRD measurements were conducted for sintered Cu electrode film made using 1 wt% gCu-ink. As seen in Figure 4.5c, the 36.4^{o} 2θ XRD peak of the before-mentioned films corresponds to {111} Cu_2O crystal planes. Compared with the 3 wt% gCu-ink, the 1 wt% gCu-ink had a weak reduction potential, which induced the incomplete Cu crystal, and the high resistivity of the electrode film. An in-depth analysis of the crystals was conducted XPS analysis of Cu electrode film made using 1 wt% gCu-ink at 350 ^{o}C. In Figure 4.5d, the satellite Cu^{2+} peak confirmed the formation of Cu oxide, but this XPS peak was different from the typical CuO peak.[30] Interestingly, the fitted Cu $2p_{3/2}$ spectrum had two major peaks belonging to Cu (932.1 eV) and CuO (933.8 eV). The coexistence of the Cu and CuO peaks could be explained by the deficient reduction potential of the 1 wt% gCu-ink. Conversely, the coexistence of the Cu and CuO spectra was also explained by supporting evidence of the glycerol reduction effect. As a result, the 3 wt% gCu-ink was chosen as optimized Cu-ink formulation, and it was used to produce Cu electrode film with the lowest resistivity even air sintering.

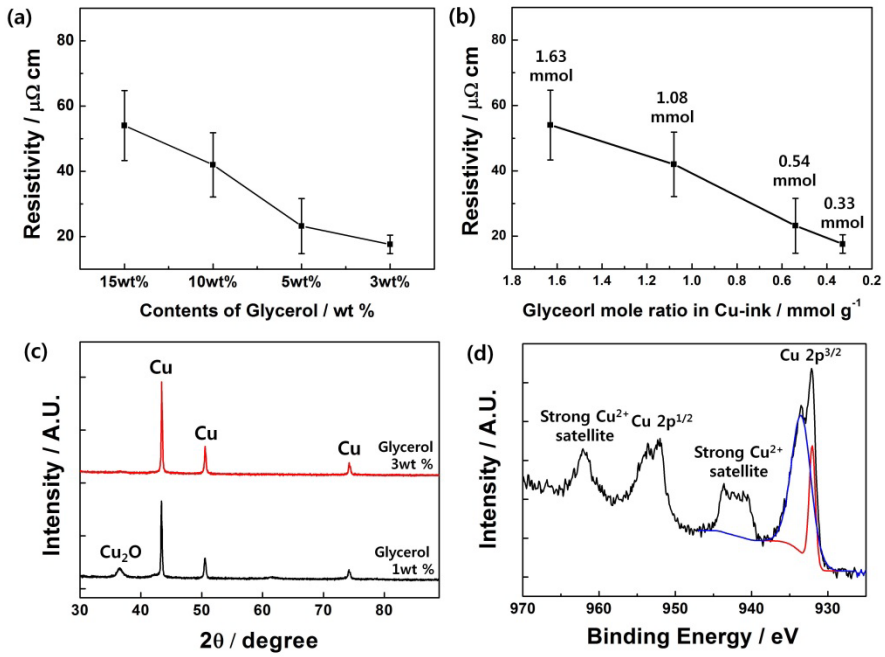

Figure 4.5 (a), (b) Specific resistivity of the sintered Cu electrode film as function of glycerol wt %, and mole ratio at 350 ^{o}C, (c) XRD pattern of the sintered Cu electrode film made using 1 wt% and 3 wt% gCu-ink, (d) XPS Cu 2p spectra of the sintered Cu electrode film made using 1 wt% gCu-ink gCu-ink

4.3.4 Practical utilization test of Cu-ink

The fabricated Cu electrode films meet important prerequisites for their practical application and in future devices, such as good substrate adhesion, long-term storage stability, and the ability to be used in flexible substrates. To promote substrate adhesion, a silane coupling agent (3- aminopropyl triethoxysilane (APTES)) was applied to the 3 wt% gCu-ink. The APTES reaction mechanism is well known.[37,38] Briefly, the hydroxyl groups of the substrate react with the alkoxy groups (ethoxy) of the APTES. Also, the amine groups of the APTES are chemically bonded to the Cu surface.[39] These reactions enhance the adhesion properties between glass substrates and Cu-ink. Through the same mechanism, APTES can be applied to various flexible polymer substrates. As slight oxygen plasma treatment of the polymer substrate, reactive hydroxyl groups are formed that, reacts with the APTES and Cu-ink. In this study, adhesion experiments were conducted using 3 wt% gCu-ink and the effect of APTES content was investigated using tape peel-off tests. Figure 4.6a shows the remaining area of a glass substrate and a tape surface after the peel-off test. The entire area of the sintered Cu electrode films made using gCu-ink was transferred from the glass substrates to the tape, while the sintered Cu electrode film made using

gCu-ink with 0.5 wt% APTES had a relatively good adhesion. As increment of 1 wt% APTES, sintered Cu electrode film exhibited excellent adhesion characteristics. Figure 4.6b shows that this Cu electrode film retained its pristine adhesion even after 10 repetitions of the 3M tape peel-off test. Resistivity of the adhesion enhanced Cu electrode film was measured as a function of APTES content (Figure 4.6c). In addition, the detailed specific resistivity of gCu-ink with no addition, 0.5, and 1 wt% APTES was confirmed in Figure 4.6d. The resistivity values were 17, 36, 65 and 1800 μΩ • cm for intrinsic gCu-ink with 0.5, 1 and 3 wt% APTES, respectively. The resistivity of adhesion enhanced Cu electrode film showed an increasing tendency dependent on the high APTES content. Notably, the sintered Cu electrode film made using gCu-ink with 3 wt% APTES led to an abrupt increase of the resistivity value. This resistivity dependence on the APTES content was associated with increased film porosity and with residual non-conductive materials (e.g. inorganic material, such as Si, of APTES).[37] These results indicated that the most suitable amount of APTES was around 1 wt% for both strong adhesion property, confirmed by 3M tape peel-off test, and low resistivity of 65 μΩ • cm.

Furthermore, the formation of a Cu electrode film on flexible substrates (polyethylene naphthalate (PEN)) was attempted using 3 wt% gCu-ink with

1 wt% APTES, and discovered that Cu electrode film could be well formed on flexible substrates. Figure 4.7a and b reveal that the fabricated electrode film was conductive enough to turn on a LED. In addition, after bending test (R=20mm) of 2000 cycles, it was able to maintain a well-connected state, as shown in Figure 4.7c and d; and a robust mechanical stability with a nearly constant resistivity, as shown in Figure 4.7e. These results indicate that the proposed gCu-ink has the possibility to be used in various practical applications and advanced devices.

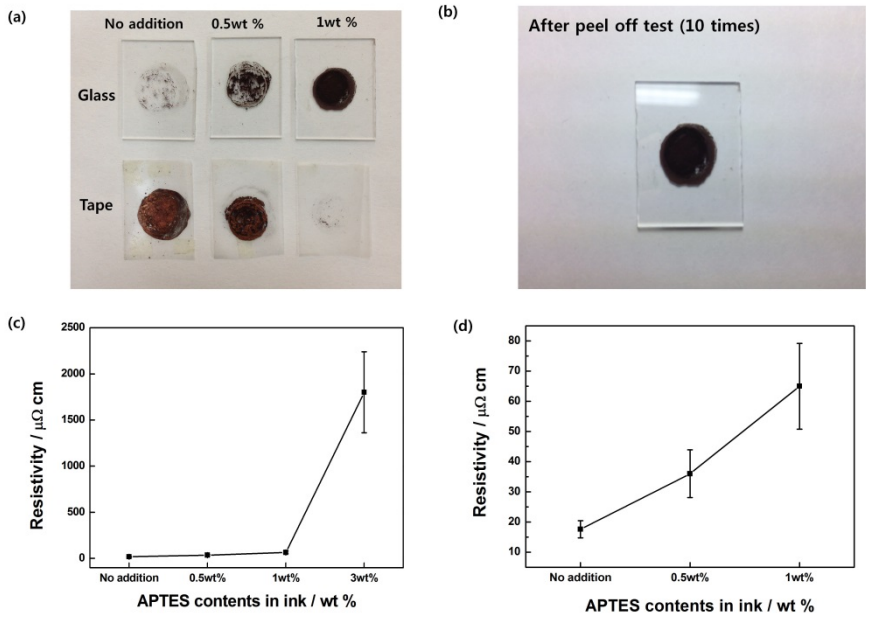

Figure 4.6 Enhanced adhesion characteristics of Cu electrode film made using 3 wt% gCu-ink; (a) Optical photograph image after the tape peel-off test; (b) Specific resistivity as a function of APTES content

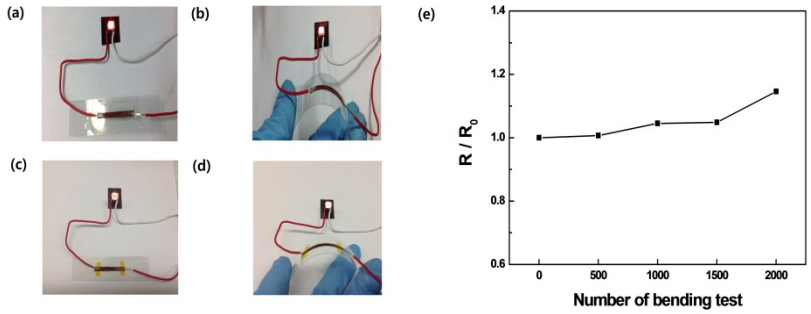

Figure 4.7 The photographs show flexible characteristic of freshly prepared Cu electrode film on PEN substrates at; (c) flat state, (d) bending state; and the Cu electrode film after the bending tests at (e) flat state, (f) bending state; and (g) the change of the resistivity during the bending test.

Finally, long-term storage stability tests were conducted with the gCu-ink, as shown in Figure 4.8a, and b. For 4 weeks, the storage stability of the ink showed excellent characteristics. Even gCu- ink with a significantly large amount of glycerol (10 wt%) had good storage stability. In addition, the chemical affinity was investigated, because it is important factor for stable ink formulation and storage. Low affinity between intrinsic Cu-ink and reduction assistance materials induces unstable storage property, rapid Cu ion reduction, and precipitation. For evaluate the chemical affinity, the mixtures of the intrinsic Cu- ink with different kinds of strong reduction assistance materials, such as N_2H_2 and $NaBH_4$, were investigated in Figure 4.8c, and d. Contrary to the gCu-ink, the strong reduction assistance materials showed unstable storage and solubility properties. The Cu-ink with 3 wt% N_2H_2 was immediately reduced from Cu-ink to brown precipitations due to the high intrinsic reduction potential of N_2H_2. Also, the Cu-ink with 3wt % $NaBH_4$ produced precipitations due to its poor solubility with IPA and $NaBH_4$. These findings indicated that polyol solvents, especially glycerol, were suitable solvent because of their optimum properties regarding both their reduction potential and good solubility with Cu-ink.

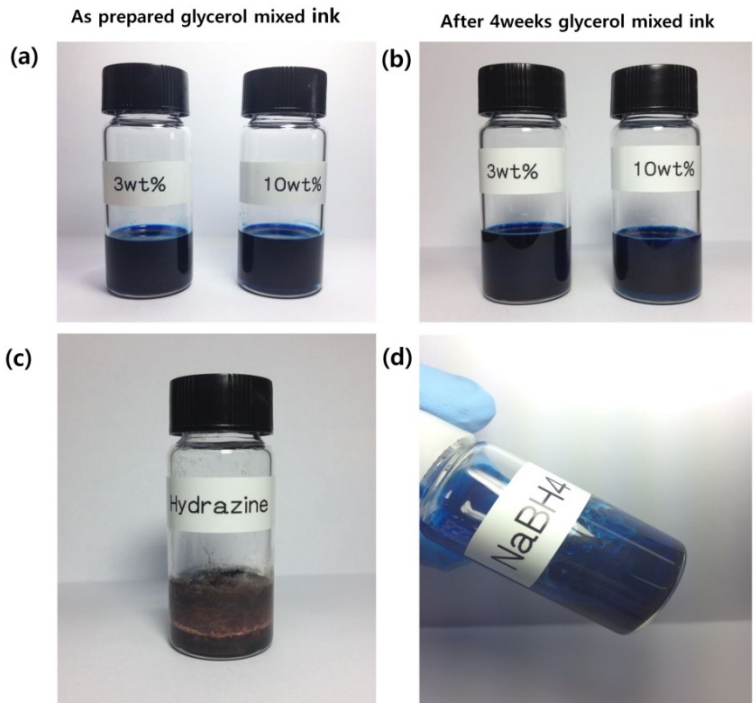

Figure 4.8 (a), (b) Photograph of 3wt % and 10 wt% gCu-ink dissolved in IPA. For 4 weeks, phase separation was not found in gCu-ink mixture. (c),(d) Image of the Cu-ink by addition of 3wt % hydrazine (N_2H_2) and sodium borohydride ($NaBH_4$), respectively

4.4 Conclusion

In conclusion, novel self-reducible Cu-ink, composed by formate, alkanolamine groups and poly alcohols, are introduced for the air sinter-able fabrication of Cu electrode films. The proposed Cu-ink had a good self-reducible activity induced by the decomposition of Cu-ink ligand and the reduction assistance effect of the polyol solvents. This self-reducible ability of Cu-ink ensured the sintering of conductive Cu electrode film under air condition. To verify the reduction assistance effect of the polyol solvents, the reduction characteristics and specific resistivity of the sintered Cu electrode films were investigated using various kinds of pCu-ink. Based on the analysis of the resistivity measurements, glycerol was confirmed to be the most suitable polyol solvent to act as a reduction assistance material, because of its proper evaporation temperature (298 oC) for the removal of organic residues and its appropriate reduction potential attributed to its many hydroxyl groups. These intrinsic glycerol properties in gCu-ink facilitated the formation of air sinter-able Cu electrode films with low resistivity. The sintered Cu electrode films made using gCu-ink were investigated as function of the sintering temperature and glycerol content. The optimized properties of the sintered Cu electrode film made using 3 wt%

gCu-ink showed a resistivity of 17 μΩ • cm at a 350 oC air sintering temperature. In addition, the potential of Cu electrode films in industrial application and for the fabrication of future devices was studied through adhesion, long-term storage and flexibility. The adhesion tests, conducted using 3M tape peel-off, showed that the Cu electrode film made using gCu-ink with 1 wt% APTES had good adhesion properties. In the case of the storage tests, the gCu-ink revealed outstanding storage stabilities for up to 4 weeks. In addition, the flexibility test demonstrated that Cu electrode film made on flexible substrates had robust resistivity retention characteristics (R/R_0 <1.2) after 2000 cycles bending tests conducted using a 20 mm bending radius. On the basis of these results, the proposed novel self-reducible Cu-ink is a promising material for air condition sintering and will be used in practical printing electronics and eco-friendly electrode fabrication processes.

References

[1] M. Singh, H. M. Haverinen, P. Dhagat and G. E. Jabbour, *Adv. Mater.*, 2010, **22**, 673.

[2] Y. N. Li, Y. L. Wu and B. S. Ong, *J. Am. Chem. Soc.*, 2005, **127**, 3266.

[3] S. Gamerith, A. Klug, H. Scheiber, U. Scherf, E. Moderegger and E. J. W. List, *Adv. Funct. Mater.*, 2007, **17**, 3111.

[4] H. Sim, J. Lee, T. Yu, K. Kim, S. J. Lee, J. H. Lee, J. H. Cho and B. Lim, *Rsc Adv.*, 2015, **5**, 2756.

[5] C. M. Zhong, C. H. Duan, F. Huang, H. B. Wu and Y. Cao, *Chem. Mater.*, 2011, **23**, 326.

[6] X. Crispin, F. L. E. Jakobsson, A. Crispin, P. C. M. Grim, P. Andersson, A. Volodin, C. van Haesendonck, M. Van der Auweraer, W. R. Salaneck and M. Berggren, *Chem. Mater.*, 2006, **18**, 4354.

[7] G. H. Gelinck, T. C. T. Geuns and D. M. de Leeuw, *Appl. Phys. Lett.*, 2000, **77**, 1487.

[8] D. H. Zhang, K. Ryu, X. L. Liu, E. Polikarpov, J. Ly, M. E. Tompson and C. W. Zhou, *Nano Letters*, 2006, **6**, 1880.

[9] D. S. Hecht, L. B. Hu and G. Irvin, *Adv. Mater.*, 2011, **23**, 1482.

[10] Y. H. Kim, C. Sachse, M. L. Machala, C. May, L. Muller-Meskamp and K. Leo, *Adv. Funct. Mater.*, 2011, **21**, 1076.

[11] S. F. Jahn, T. Blaudeck, R. R. Baumann, A. Jakob, P. Ecorchard, T. Ruffer, H. Lang and P. Schmidt, *Chem. Mater.*, 2010, **22**, 3067.

[12] D. Lee, D. Paeng, H. K. Park and C. P. Grigoropoulos, *Acs Nano*, 2014, **8**, 9807.

[13] C. Kind, A. Weber and C. Feldmann, *J. Mater. Chem.*, 2012, **22**, 987.

[14] J. Perelaer, A. W. M. de Laat, C. E. Hendriks and U. S. Schubert, *J. Mater. Chem.*, 2008, **18**, 3209.

[15] D. P. Li, D. Sutton, A. Burgess, D. Graham and P. D. Calvert, *J. Mater.*

Chem., 2009, **19**, 3719.

[16] S. Magdassi, M. Grouchko and A. Kamyshny, *Materials*, 2010, **3**, 4626.

[17] S. Cho, K. H. Lim, S. Y. Park, Z. Yin, J. Yoo and Y. S. Kim, *J. Mater. Chem. C*, 2015, **3**, 2773.

[18] M. Grouchko, A. Kamyshny and S. Magdassi, *J. Mater. Chem.*, 2009, **19**, 3057.

[19] Y. H. Choi and S. H. Hong, *Langmuir*, 2015, **31**, 8101.

[20] Y. H. Choi, J. Lee, S. J. Kim, D. H. Yeon and Y. Byun, *J. Mater. Chem.*, 2012, **22**, 3624.

[21] K. Woo, Y. Kim, B. Lee, J. Kim and J. Moon, *Acs Appl. Mater. Inter.*, 2011, **3**, 2377.

[22] A. Yabuki, N. Arriffin and M. Yanase, *Thin Solid Films*, 2011, **519**, 6530.

[23] S. Wunscher, R. Abbel, J. Perelaer and U. S. Schubert, *J. Mater. Chem. C*, 2014, **2**, 10232.

[24] M. S. Rager, T. Aytug, G. M. Veith and P. Joshi, *Acs Appl. Mater. Inter.*, 2016, **8**, 2441.

[25] A. Yabuki, Y. Tachibana and I. W. Fathona, *Mater. Chem. Phys.*, 2014, **148**, 299.

[26] D. H. Shin, S. Woo, H. Yem, M. Cha, S. Cho, M. Kang, S. Jeong, Y. Kim, K. Kang and Y. Piao, *Acs Appl. Mater. Inter.*, 2014, **6**, 3312.

[27] Y. Farraj, M. Grouchko and S. Magdassi, *Chem. Comm.*, 2015, **51**, 1587.

[28] K. J. Carroll, J. U. Reveles, M. D. Shultz, S. N. Khanna and E. E. Carpenter, *J. Phys. Chem. C*, 2011, **115**, 2656.

[29] S. Jeong, K. Woo, D. Kim, S. Lim, J. S. Kim, H. Shin, Y. N. Xia and J. Moon, *Adv. Funct. Mater.*, 2008, **18**, 679.

[30] T. Ghodselahi, M. A. Vesaghi, A. Shafiekhani, A. Baghizadeh and M. Lameii, *Appl. Surf. Sci.*, 2008, **255**, 2730.

[31] M. Huang, Y. X. Zhang, F. Li, Z. C. Wang, Alamusi, N. Hu, Z. Y. Wen

and Q. Liu, *Sci. Rep.*, 2014, **4,** 4518.

[32] M. S. Cho, W. H. Choi, S. G. Kim, I. H. Kim and Y. Lee, *J. Nanosci. Nanotechnol.*, 2010, **10**, 6888.

[33] T. Ishizaki and R. Watanabe, *J. Mater. Chem.*, 2012, **22**, 25198.

[34] Y. Chang, D. Y. Wang, Y. L. Tai and Z. G. Yang, *J. Mater. Chem.*, 2012, **22**, 25296.

[35] A. Maattanen, P. Ihalainen, P. Pulkkinen, S. X. Wang, H. Tenhu and J. Peltonen, *Acs Appl. Mater. Inter.*, 2012, **4**, 955.

[36] M. Huang, Y. X. Zhang, F. Li, Z. C. Wang, Alamusi, N. Hu, Z. Y. Wen and Q. Liu, Sci. Rep., 2014, **4**, 4518.

[37] Y. I. Lee and Y. H. Choa, *J. Mater. Chem.*, 2012, **22**, 12517.

[38] S. Jeong, H. C. Song, W. W. Lee, Y. Choi, S. S. Lee and B. H. Ryu, *J Phys Chem C*, 2010, **114**, 22277.

[39] S. Cho, D. H. Shin, Z. Yin, C. Lee, S. Y. Park, J. Yoo, Y. Piao and Y. S. Kim, *Chem. Euro. J.*, 2015, **21**, 6690.

Chapter 5. One-step simple synthesis of Copper oxide/expanded graphite composite for high performance batteries anodes

5.1 Introduction

The rapid development of electronic devices has resulted in dramatic advancements in lithium ion batteries (LIBs) technology.[1-3] LIBs are used in various equipment, ranging from small portable electronic devices (such as mobile phone, notebook computer, e-book) to large energy storage system (such as industrial equipment, power plants).[4,5] Especially, they are expected to be a core technology in the development of future electric vehicles (EVs). The use of LIBs in EVs is currently limited by their capacity, cost, weight, and their significantly shorter lifespans, compared to combustion engines.[6,7] To improve these properties, research has focused primarily on advanced LIBs, sodium ion batteries (SIBs), redox flow batteries (RFB) as next-generation energy storage devices.[8,9] Though these battery developments, the importance of anode material with high energy density, capacity, and low cost has been raised, because the ion storage

efficiency of anode electrode significantly influences to overall cell performance such as cycling stability, specific capacity, and working voltage. Hence, the studies of various anode materials with high energy densities and capacities have been proposed for advanced LIB and SIB.[10,11]

Graphite has been widely used as a conventional anode material in LIBs due to its operating potential, low-cost and outstanding electrochemical performance. However, the performance of graphite is limited by the narrow interlayer distance and its relatively low theoretical capacity.[12-14] During Li ion intercalation, the structure of graphite is deformed by the resulting change in volume; structural imperfections reduce the cycling stability of graphite.[12] Specifically, during the charging process the solvated Li ions penetrate into the graphite, increasing the interlayer distance and forming LiC_6. Conversely, the discharging process causes de-intercalation of the Li ions from graphite and returns the interlayer distance to its initial value (0.34 nm). Over repeated charge-discharge cycles, stress accumulates in the graphite interlayer, which seriously affects cycling stability.[15] In SIBs, this the small graphite interlayer distance has a greater effect on cycling stability because 0.34 nm is insufficient to accommodate the larger Na ions; generally, an interlayer distance of 0.37 nm is required for stable Na ion intercalation.[13] In addition, the relatively low theoretical capacities

of graphite-based LIBs (372 mAh g^{-1}) and SIBs (35 mAh g^{-1}) are insufficient for demanding applications requiring high energy densities.[16,17] Recently, metal (Sn, Si, Ge etc.) and metal oxide (Fe_3O_4, CoO, NiO, etc.) and carbonaceous materials (graphene, carbon nanotube (CNT)), have been proposed as next generation anode materials because of their high theoretical capacities.[18,19] However, the use of metals or metal oxides can result in large volume expansion due to Li alloying reactions. This process degrades electrode and reduces the cycling stability of batteries.[18] The drawbacks of carbonaceous materials include long processing times, high manufacturing costs, and complex preparation procedures, which limit their application in practical LIBs and SIBs.[20]

Various strategies have been attempted to improve the performance of anodes. To improve energy density and cycling stability, carbon and metal oxide composites have been synthesized, including metal oxide/graphene composites, carbon-coated metal oxide nanoparticles, and metal oxide/CNT composites.[21-23] The modification of commercialized graphite has been recently proposed as an effective method for increasing cycling stability, as a result of the expansion of the graphite interlayer distance.[24,25] Modified graphite has exhibited stable storage capacities during charge-discharge processes. However, the production of these anode materials involves

complex, time-consuming, and hazardous processes, such as strong acid etching. Moreover, as a result of these processes, the fabricated carbon-based materials may exhibit structural distortions and organic residues, which can take part in side reactions during galvanostatic charging/discharging.[26] Thus, the development of a simple manufacturing method for novel graphite would be beneficial for improving the capacity and cycling stability of anode materials for LIBs and SIBs.

Herein, a one-step simple synthesis of a novel Cu oxide/graphite composites (GCuO) *via* the thermal decomposition of a Cu ion complex is proposed, which exhibited highly stable cycle-ability and a high energy density. During thermal decomposition, the annealed Cu ion complex rapidly generates H_2 and CO_2 gases, which induce graphite interlayer expansion (from 0.34 nm to 0.40 nm) and simultaneously produce Cu oxide nanoparticles *via* reduction of the Cu ion complex. The structure of GCuO has several desirable properties. Firstly, the large interlayer distances of the graphite prevent severe volume change of the anode and enable the efficient storage of Li or Na ions during charging/discharging process. Secondly, the redox reactions of the Cu oxide nanoparticles results in high energy densities and capacities. These features overcome the inherent disadvantages of graphite and metal oxide materials. Moreover, GCuO

exhibited a high reversible capacity of 532 mAh g^{-1} at current rate (C-rate) of 0.2 C, and retain 83 % of its capacity after 250 cycles (0~100 cycles at 0.2 C and 100~250 cycles at 1 C). Additionally, the electrochemical analysis of a $LiFePO_4$/GCuO cell demonstrated stable cycling performance (30 cycles) and high coulombic efficiency (99%), which indicated the suitability of GCuO for practical applications.

5.2 Experimental section

5.2.1 Chemicals & materials

Graphite powders (artificial graphite) were obtained from MTI Korea. Copper (II) formate tetrahydrate (98 %) was purchased from Alfa Aesar. 2-amino-2-methyl-1-propanol (AMP; 95 %) and octylamine (99 %) were obtained from Aldrich. Methyl alcohol (MeOH; 99.5 %) and isopropyl alcohol (IPA; 99.5 %) were purchased from Daejung Chemicals. All reagents were used as received without further purification.

5.2.2 Synthesis of Cu ion complex

The Cu ion complex was synthesized as follows. AMP (8.98 g) and octylamine (11.45 g) were mixed for 30 min in a 250 mL round bottom flask. Then, methyl alcohol (20 mL) and Cu (II) formate tetrahydrate (20 g) were added to the mixture. The color of the solution changed immediately to a transparent blue as soon as Cu (II) formate tetrahydrate was poured. The mixture was stirred for 1 h at room temperature. The solvent was removed under reduced pressure at 50°C using a rotary evaporator. Then the product was vacuum dried for 8 h at 50°C. The dry product was obtained as a dark blue, highly viscous, complex. To control the viscosity, the Cu ion complex and IPA in 1:9 (w:w) *via* sonication and vortex mixing.

5.2.3 Fabrication of expanded graphite

GCuO was fabricated by mixing pristine graphite and the IPA solution of the Cu ion complex in weight ratio of 1:2, 1:4, 1:8, and 1:16 using a homogenizer (AR 100, Thinky mixer) at 1000 rpm for 10 min. Each mixture was sintered for 8h at 400 ^{o}C. For comparison, reference powder

(Cu Oxide) was produced by sintering the Cu ion complex under the same condition.

5.2.4 Electrochemical test

To fabricate the electrode, a slurry was prepared by mixing a 6:3:1 weight ratio of GCuO, Super P (Timcal), and styrene butadiene rubber/carboxymethyl cellulose (SBR/CMC) in distillated water. Super P was used as a conducting agent and the rubber/cellulose was used as a binder. Graphite and Cu oxide slurries were prepared using the same proportions for comparison. The slurries were coated onto copper substrates (9 mm thick) using a Meyer rod. The electrodes were dried at 120 ^{o}C, and assembled into CR-2032 coin cells. The half-cells were composed of a working electrode (GCuO, graphite, or Cu oxide), a separator (PP membrane: Celgard 2500) soaked in liquid electrolyte (1 M LiPF6 in EC/DMC/DEC in a volume ratio of 1:1:1), and a reference electrode (Li foil; thickness: 150 μm). For the practical cell performance test, full-cells were fabricated, consisting of a cathode ($LiFePO_4$; LFP), a separator (PP membrane) soaked in liquid electrolyte (1M $LiPF_6$ in EC/DMC/DEC in a volume ratio of 1:1:1), and an anode (GCuO or graphite). The cathode

slurry was prepared by mixing LFP, Super P, and polyvinylidene fluoride (PVdF; Kynar HSV 900) in N-methyl-2-pyrrolidone in a weight ratio of 75:15:10. . The cathodes were coated and dried in the same way as the GCuO anodes. Cell assembly was performed under an argon atmosphere. The assembled cells were subjected to analysis of electrochemical reaction mechanism with cyclo-voltammogram analysis and specific capacity characteristics such as rate capability and reliability test by investigating the charging-discharging characteristics in battery cycler system (WBCS 3000L, WonATech). For the cell resistance measurements, AC impedance spectroscopy (CHI660E, CH Instruments) was conducted from 0.1 Hz to 1 MHz at room temperature.

5.3 Results and discussion

5.3.1 Preparation of expanded graphite/Copper oxide composite and reaction mechanism

Scheme 1 shows a schematic representation of the fabricated anode materials reaction mechanism. Thermal decomposition of Cu ion complex produced H_2 and CO_2.[27,28] (Scheme 1a) This causes expansion of the graphite interlayers and the formation of Cu oxide nanoparticles as a result of Cu ion reduction.[27] During Li intercalation process, the stress of the graphite layers in GCuO is significantly different from those in pristine graphite. (Scheme 1b) This stress is caused by the size of the solvated Li ions.[29-31] Therefore, the enlarged graphite interlayer distances in GCuO reduce stress and increase its stability during charge/discharge processes in LIBs. In addition, the formation of Cu oxide nanoparticles increases the capacity and energy density by conversion reaction. To identify these effects, materials and electrochemical analyses were performed.

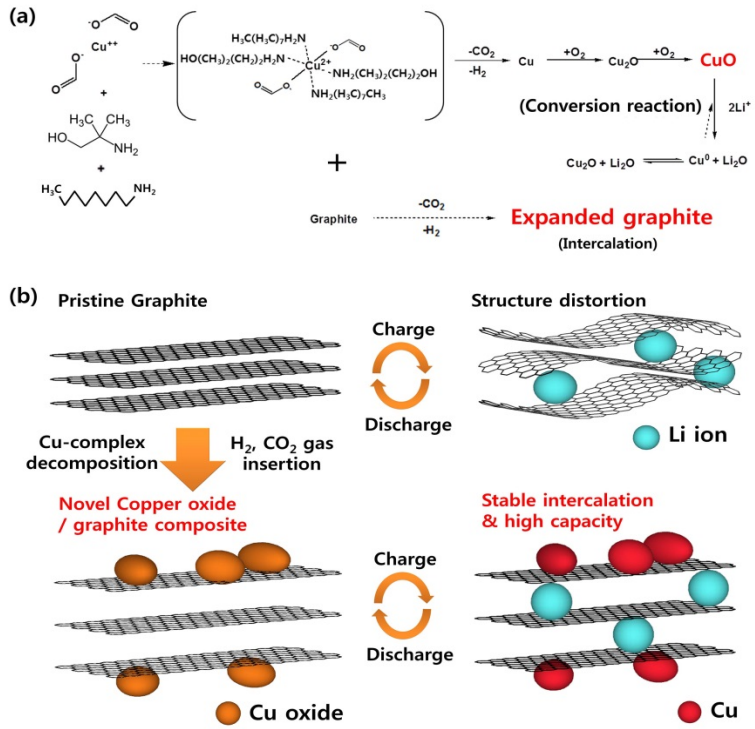

Scheme 5.1 Schematic illustration of (a) Cu ion complex chemical structure and formation mechanism of novel Cu oxide/graphite composite, (b) Metal ion (Li^+) intercalation mechanism of novel Cu oxide/graphite composite. Thermal decomposition of Cu ion complex generates H_2 and CO_2 gases, which induce the Cu oxide formation and graphite layer expansion. In the charging process, when Li ions insert to pristine graphite, the structure is strongly distorted. Otherwise, the novel Cu oxide/graphite composite show the stable Li ion intercalation by graphite layer expansion, and the enhanced high capacity by Cu oxide conversion reaction.

5.3.2 Analysis of expanded graphite/copper oxide composite

GCuO was analyzed to confirm the formation of expanded graphite and Cu oxide nanoparticles. Figure 5.1a and b show XRD patterns of the fabricated anodes and a high-resolution transmission electron microscopy (HR-TEM) image of GCuO, respectively. The XRD results confirmed the crystal structures of sintered GCuO, graphite, and Cu oxide. The graphite samples exhibited a typical graphite peak (JCPDS 41-1487). The Cu oxide sample exhibited Cu(I) oxide (JCPDS 05-0667), Cu(II) oxide (JCPDS 41-0254), and Cu (JCPDS 04-0836) peaks. The GCuO 1:4 and 1:16 samples exhibited graphite, Cu(I) oxide, and Cu(II) oxide peaks. TEM analysis of GCuO 1:16 properties demonstrated that Cu oxide nanoparticles were evenly distributed on the graphite surface, which mean the effective formation of Cu ion complex with graphite mixture. (Figure 5.1b) The elemental composition of the nanoparticles was determined using elemental mapping via scanning transmission electron microscopy (STEM)-energy dispersive spectroscopy (EDS) analysis (Figure 5.1c). Red and green regions were the elements of Cu and oxygen (O), respectively. Elemental

mapping verified that the nanoparticles on the surface of the graphite were Cu oxide crystals.

To evaluate the performance of the LIB anode materials, the oxide compositions of GCuO samples (1:2, 1:4, 1:8, and 1:16 weight ratios) were determined by thermogravimetric analysis (TGA) and X-ray photoelectron spectroscopy (XPS). Figure 5.1d shows the thermal decomposition of the pristine Cu ion complex (without dispersed IPA) under O_2. Weight loss was observed at temperatures of 100–200 °C. Inorganic residue comprised 16.8 wt% of the initial sample. These results were used to indirectly determine the Cu oxide contents of the graphite–Cu ion complexes. In addition, as objective evidence, XPS elemental analysis was conducted for the weight percent evaluation of Cu, O, and C in the GCuO samples (Table 5.1). In Figure 5.1e, the calculated Cu oxide content increased linearly with the proportion of Cu ion complex used in GCuO synthesis. Overall, the analyses shown in Figure 5.1 confirmed the formation of Cu oxide via decomposition of the Cu ion complex, the distribution of Cu oxide nanoparticles on the surface of the graphite, and the Cu oxide content of the fabricated anode materials.

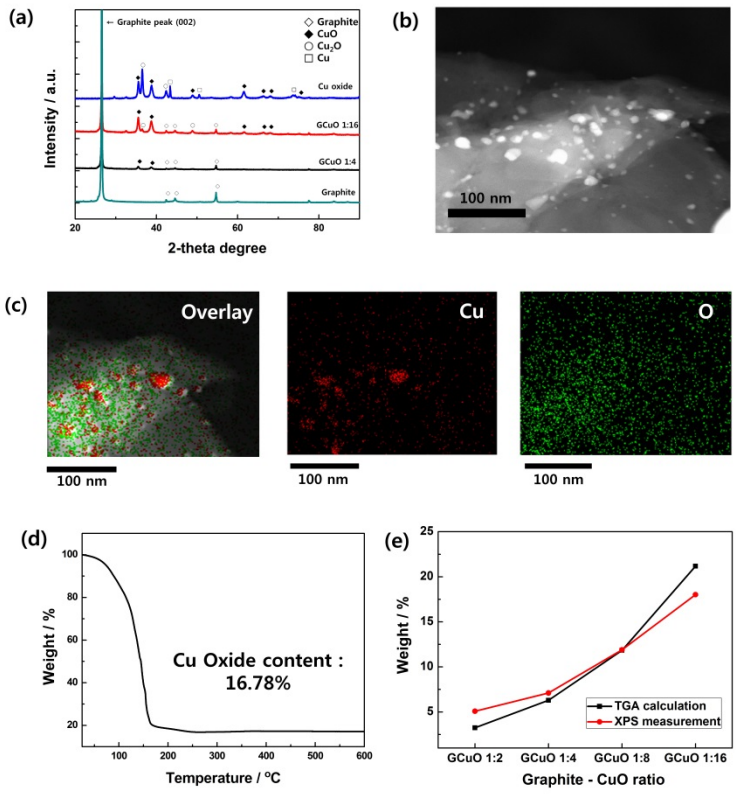

Figure 5.1 Characteristics of fabricated materials; (a) XRD patterns of Cu Oxide, graphite, GCuO1:4, and GCuO 1:16, (b) HR-TEM image of GCuO 1:16, (c) TEM-EDS image (d) TGA of pure Cu ion complex, and (e) Comparison of calculated Cu oxide content determined from TGA and XPS data.

Sample	TGA based calculation (wt %)	XPS measurement (wt %)
GCuO 1:2	3.25	5.08
GCuO 1:4	6.29	7.11
GCuO 1:8	11.84	11.9
GCuO 1:16	21.18	18.015

Table 5.1 Calculated element Cu oxide content (wt %) in GCuO samples, as determined by TGA analysis and XPS fitting.

To reveal the effect of expansion in the graphite interlayers, GCuO powder was analyzed by Raman spectroscopy and HR-TEM. Figure 5.2a and b show the Raman spectra of graphite, GCuO 1:4, and GCuO 1:16. The graphite spectrum exhibited two dominant peaks at 1345 and 1570 cm^{-1} (Figure 5.2a), corresponding to D and G bands, respectively. Compared with the graphite sample, the GCuO spectra exhibit positively shifted G bands and higher-intensity D bands. The positive G band shift (about 15 cm^{-1}) indicates the presence of covalent bonding between the graphite surface and Cu oxide nanoparticles (Cu–C). [32] The increased intensity of the D bands can be calculated as the intensity ratio (I_D/I_G) of the D and G bands, and is an expression of the level of disorder in the graphite. The intensity ratios of graphite, GCuO 1:4, and GCuO 1:16 were 0.13, 0.66, and 0.74, respectively. Increases in the I_D/I_G ratio are generally the result of increased exposure of the edge planes and misaligned AB stacking in graphite.[31] These results indicate that GCuO exhibits characteristics of expanded graphite, as a result of Cu ion complex decomposition. The expanded graphite exhibited a negatively shifted 2D band position, compared to that of graphite (Figure 5.2b). According to previous reports, the expansion of graphite can be confirmed by monitoring the negative shift in the peak

position.[34] The Raman spectra (G, D, and 2D band) are in good agreement with previously reported graphite expansion data.

HR-TEM was used to directly observe graphite and GCuO (Figure 5.2c and d). The graphite and GCuO were visible as alternating bright and dark regions. Graphite (Figure 5.2c) exhibited a layered structure with long-range order and parallel stacking. The interlayer distance was typical for graphite (0.34 nm).[15] On the other hand, GCuO in Figure 5.2d exhibited as expanded interlayer distance of 0.40 nm. This increased interlayer distance was also evident in the HR-TEM contrast profiles (Figure 5.2e, f). These profiles were plotted across five stacking layers at the locations indicated by the bars in Figure 5.2c and d. The contrast profiles and HR-TEM images corresponded well with the Raman spectral data.

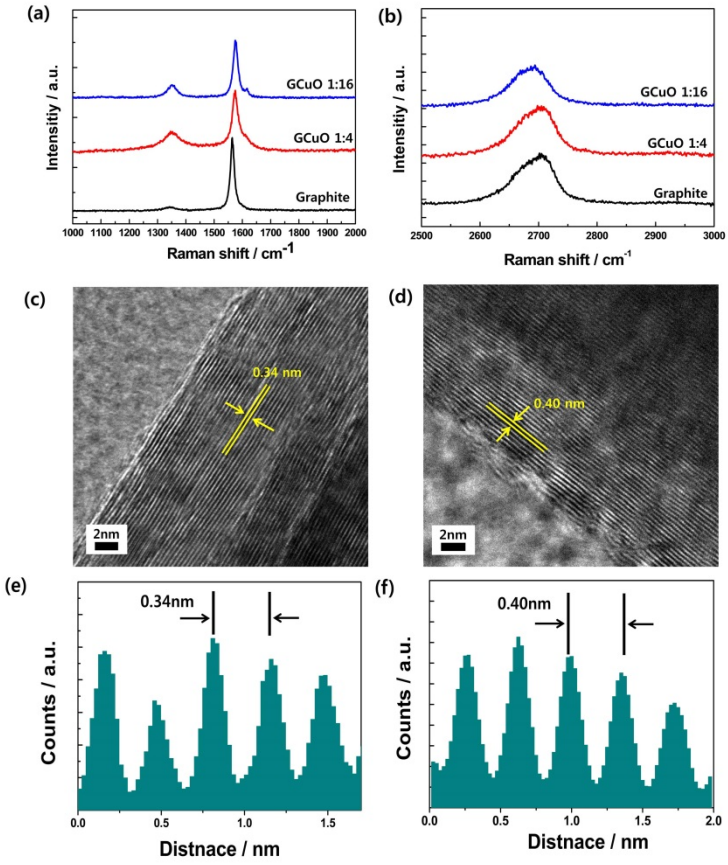

Figure 5.2 Raman spectra of GCuO and graphite; (a) D and G peak (b) 2D peak comparison of GCuO and graphite. HR-TEM images of graphite layers (c) graphite, and (d) expanded graphite in GCuO 1: 16. Contrast profiles along the yellow arrow, indicating carbon interlayer spacing of (e) graphite and (f) GCuO 1:16.

5.3.3 Electrochemical analysis of GCuO half-cell

Electrochemical analyses of fabricated GCuO anode were carried out to verify the LIBs performance. As shown in Figure 5.3a, cyclic-voltammogram analyses of GCuO, graphite, and Cu oxide anodes were conducted from 0.02 to 3 V at a scanning rate of 0.1 mV s^{-1} for 5 cycles. The three cathodic peaks of Cu oxide were located at 0.85, 1.5, and 2.17 V *vs* Li^+, respectively. Cathodic peaks in the discharge stage were caused by the reduction reaction of the following equilibrium: $CuO + 2\ Li^+ \rightarrow Cu^0 + Li_2O$. In the anodic scan, the broader oxidation potential ~2.5 V came from the formation of CuO ($Cu^0 + Li_2O \rightleftharpoons CuO + 2\ Li^+$).[35] In the graphite cyclic-voltammogram, the anodic and cathodic peaks were observed at 0.30 (intercalation) and 0.02 V (de-intercalation) *vs* Li/Li^+.[24] The cathodic and anodic peaks of the GCuO cell were similar to typical Cu oxide and graphite peaks. Specifically, the cathodic peaks at 0.85, 1.3, and 2.17 V were attributed to Cu oxide reduction, and the 0.26 V peak was attributed to graphite intercalation. The anode peaks at 0.016 and 2.5 V were founded, resulting from graphite de-intercalation and Cu oxidation, respectively. Interestingly, the intercalation and the de-intercalation current densities were increased by the addition of the Cu ion complex. This effect was

attributed to structural transitions of the graphite induced by the decomposition of the Cu ion complex. These transitions increased the exposure of the edge plane, enabling easier access for solvated Li ions. Moreover, the shifts in the intercalation and de-intercalation peaks of the GCuO anode were assumed by interactions between Cu oxide nanoparticles and the expanded graphite.[24] These structural features accounted for the differences between the specific capacities, rate capabilities, and voltage profiles of GCuO and graphite anodes.

Galvanostatic charge/discharge profiles of the GCuO 1:16 cells are shown in Figure 5.3b. The galvanostatic analyses were conducted between 0.02 and 3 V at a constant C-rate of 0.2 C. The theoretical capacities used for C-rate calculations are shown in Table 5.2, considering the expanded graphite with Cu oxide weight ratio. The first discharged capacity of solid electrolyte interface (SEI) film formation and the irreversible electrochemical reaction between Li^+ and Cu oxide exhibited a capacity of 580 mAh g^{-1}.[36] After the irreversible reaction of the first cycle, a specific capacity of 532 mAh g^{-1} was obtained from the voltage profiles, which exhibited stable cycling properties over the following 60 cycles. At the 20^{th} cycle, discharge plateaus (0.1, 0.85, and 1.35 V) and charge plateaus (0.26 and 2.5 V) were observed. Specifically, the 0.1 V discharge plateau and the 0.26 V charge

plateau came from the graphite intercalation and de-intercalation reactions, respectively, which was confirmed by comparison with the graphite voltage plateau shown in Figure 5.3c. The discharge plateaus at 1.35 and 0.85 V, and the charge plateau at 2.5 V were attributed to Cu oxide reactions. [37] These voltage plateaus correspond well with the cyclo-voltammogram results.

The high-rate capabilities of GCuO and graphite cells are shown in Figure 5.4a; the cells were tested for five cycles at C-rates of 0.2, 1, 5, and 10 C. The specific capacities of graphite and GCuO cells are summarized in Table 5.3. The capacities increased with increasing Cu ion complex loading, which corresponded with the current densities of the graphite oxidation peak from cyclo-voltammogram studies. These results indicate that the capacity differences between GCuO and graphite cells resulted from enhanced Li ion diffusion into the graphite layer and the high theoretical capacity of Cu oxide. The GCuO 1:16 cell exhibited the highest capacities, demonstrating a capacity of 532 mAh g^{-1} after 5 cycles at 0.2 C. Saturation of the capacity was observed between GCuO 1:16 and GCuO 1:8 cells, which was induced by compensation of Cu oxide capacity degradation and graphite interlayer expanding phenomenon. In addition, the capacities of the anodes were reduced with increasing C-rate; for example, GCuO 1:16

exhibited capacities of 339, 167, and 109 mA h g^{-1} at 1, 5, and 10 C, respectively. In contrast to the high gravimetric capacity, the volumetric capacity indicated 306.46 mAh cm^{-3}, which is lower than the commercialized graphite (400~430 mAh cm^{-3}).[6] However, the GCuO anode is considered to be of sufficient value because it is superior in terms of lithium storage stability.

Based on the rate capability results, the galvanostatic cycling performances of GCuO 1:16, graphite, and Cu oxide cells are shown in Figure 5.4b. The cycling properties and coulombic efficiencies were investigated at 0.2 C for the first 100 cycles. During this period, the GCuO cell demonstrated a capacity decay rate of less than 6%. In contrast, the Cu oxide and graphite anodes exhibited critical capacity fading of 60 and 37%, respectively, over the same voltage range (0.02～3 V). These significant capacity losses were induced by excessive strain in the graphite structure and anode degradation caused by Li-Cu oxide conversion reactions. [18] Figure 5.4c show the cycling stabilities of the GCuO 1:16 and graphite cells over 150 cycles at 1C, after 100 cycles at 0.2 C. The graphite cell capacity decreased rapidly to 57% of its initial value. The GCuO cell exhibited relatively stable cycling performance, with a capacity decay of 17%. In addition, the GCuO and graphite cells exhibited coulombic efficiencies

greater than 98%. The gravimetric energy density of the GCuO cell was verified to be 263 Wh kg^{-1}, which was 2.8 times as large as that of the graphite half-cell (93 Wh kg^{-1}).

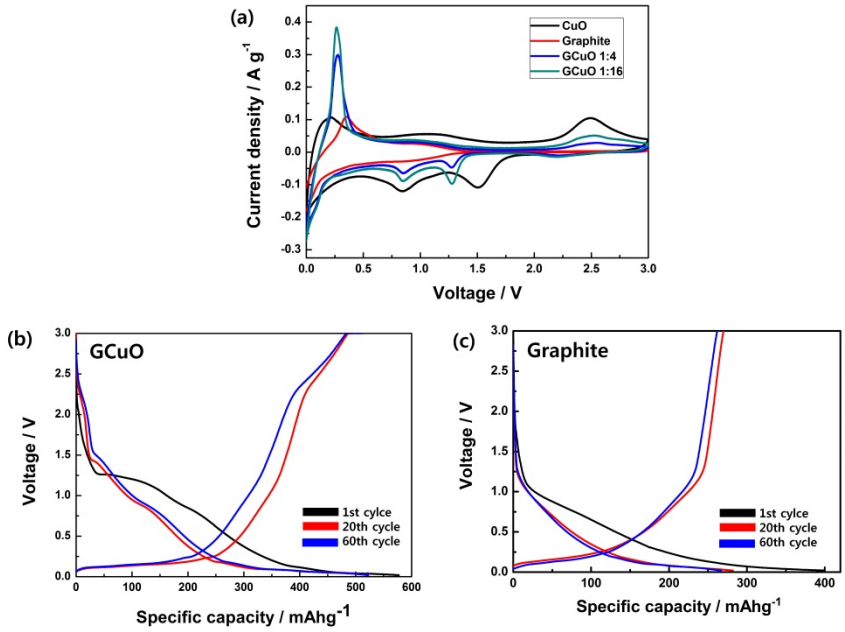

Figure 5.3 (a) Cyclo-voltammogram plots of Cu Oxide, graphite, and GCuOs, Voltage profiles of GCuO and graphite half-cell (electrode/Li metal) over 60 cycles at 0.2 C; (b) GCuO 1:16, (c) Graphite.

Sample	Cu oxide contents (wt %)	Theoretical capacity (mA h g^{-1})
Intrinsic graphite	0	372
GCuO 1:2	3.25	381.6
GCuO 1:4	6.29	390.74
GCuO 1:8	11.84	407.28
GCuO 1:16	21.18	435.11
Intrinsic Cu oxide	100	670

Table 5.2 Cu oxide content and theoretical capacities of GCuO samples for the C-rate confirmation of half-cells

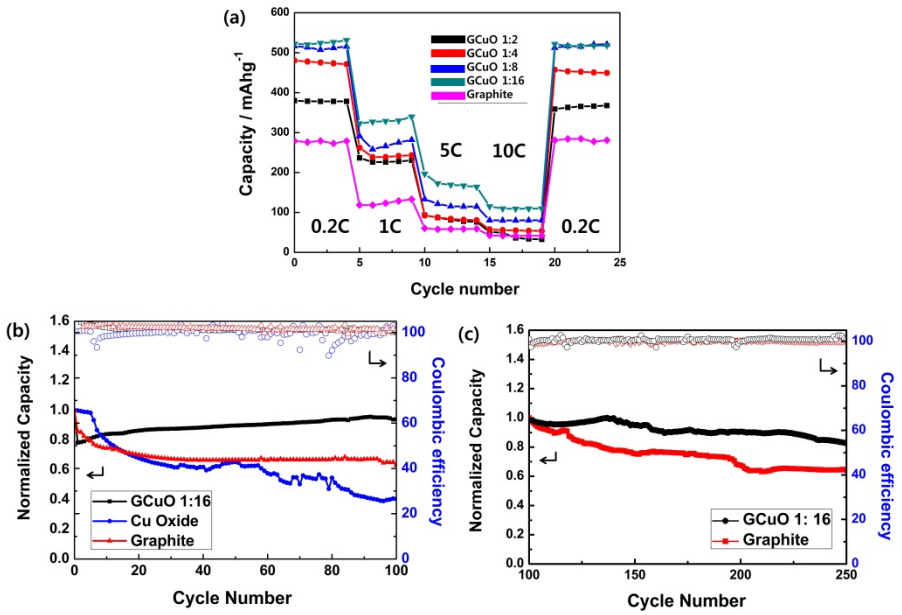

Figure 5.4 (a) Rate capabilities of graphite and GCuO samples at C-rate from 0.2 C to 10 C, and then back to 0.2 C. Cycling performance and coulombic efficiency of the half-cells; (b) o to 100 cycles at 0.2 C. (c) 100 to 250 cycles at 1 C.

Unit : mAh g^{-1}

	Intrinsic graphite	GCuO 1:2	GCuO 1:4	GCuO 1:8	GCuO 1:16
0.2 C	279.07	378.14	471.09	515.49	532
1 C	133.12	230.15	243.45	281.77	329.91
5 C	60.30	76.0	81.72	115.57	167.11
10 C	41.6	36.32	54.22	80.49	109.89

Table 5.3 High-rate capability of GCuO and graphite half-cells in different C-rates

5.3.4 Cycling test and impedance analysis of GCuO full-cell

The results shown in Figure 5.3 and Figure 5.4 were characterized from half-cells, composed of fabricated anode material and Li metal. However, to determine the suitability of GCuO anodes in practical applications, it was necessary to construct a full-cell containing a GCuO anode, an LFP cathode, and an electrolyte solution ($LiPF_6$ in EC/DMC/DEC). The voltage profile of the GCuO/LFP full-cell is shown in Figure 5.5a. Based on the half-cell voltage profile of GCuO and LFP, the full-cell charge/discharge cycles were conducted from 0.3 to 3 V at a rate of 0.2 C (calculated from the theoretical capacity of LFP = 175 mAh g^{-1}). Discharge voltage plateaus were observed between 2.5–1.5 V and 1.0–0.5 V, which were attributed to Li ion de-intercalation and conversion reactions between Cu oxide and Li ions, respectively. The voltage profiles of the charge process exhibited plateau regions at 1.9–2.1 V and 2.3–2.8 V, which corresponded to conversion reactions and Li ion intercalation, respectively. This GCuO full-cell voltage plateaus were verified by comparison with the graphite/LFP full-cell voltage plateaus (Figure 5.5b).

The cycling properties and columbic efficiencies of the GCuO and graphite full-cells are shown in Figure 5.6. After 30 charge/discharge cycles at 0.2 C, the capacity of the graphite cell had decreased from 66 to 28 mAh g^{-1}. The GCuO cell maintained an average capacity of 70 mAh g^{-1} after 30 cycles. The graphite/LFP full-cell has already been commercialized, and is known to be stable in the range of 2.5–3.5 V.[38] The stability of the proposed cells was tested over a wide voltage range of 0.3–3.5 V for the reaction of Cu oxide nanoparticles. However, increasing the operating voltage range adversely affects the stability of graphite, because excessive Li ion intercalation increases the stress on the graphite interlayers. Meanwhile, the expanded graphite of the GCuO cells exhibited stable capacity retention, because of alleviating intercalation stress. Wide operating voltage ranges are necessary for large-scale applications, and for the adoption of high-capacity metal and metal oxide anode materials (such as SnO and Mn_2O_3). The average columbic efficiencies (excluding the first cycle) of the graphite and GCuO cells were 92.2 and 99%, respectively. This high columbic efficiency of GCuO full-cell indicates its excellent stability when used as an anode material, comparing with graphite. Therefore, the excellent electrochemical characteristics of GCuO full-cells are confirmed by a stable cycling capacity and columbic efficiency.

To compare the resistances of GCuO and graphite cells, electrochemical impedance spectroscopy (EIS) measurements were conducted on the corresponding full-cells (Figure 5.7). Fresh graphite and GCuO cells showed similar bulk resistances (R_b = 2.6 and 1.9 Ω, respectively) and charge transfer resistances (R_{ct} = 8.7 and 9.5 Ω, respectively). However, after 30 charge/discharge cycles, the differences between the graphite and GCuO cells were more significant (R_b = 18.22 and 33.82 Ω for GCuO and graphite cells, respectively). These results indicate that the expanded graphite of the GCuO electrode exhibited lower stress from Li ion intercalation than the graphite electrode. Moreover, the high resistance retention of the GCuO cell results in increased cycling stability and rate capability.

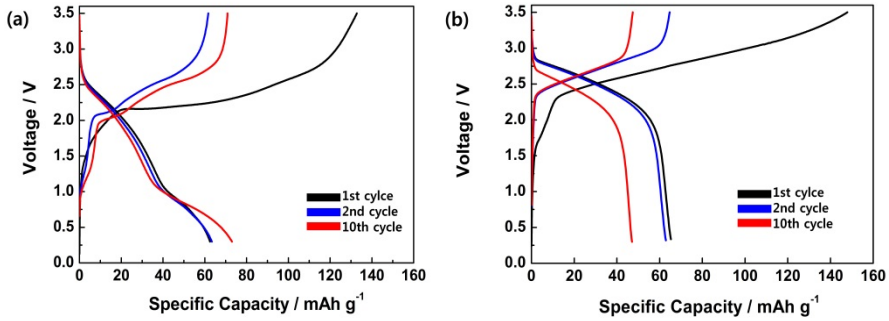

Figure 5.5. Electrochemical characterization of GCuO and graphite full-cells; Voltage profiles of (a) GCuO 1:16 and (b) graphite at C-rate of 0.2 C

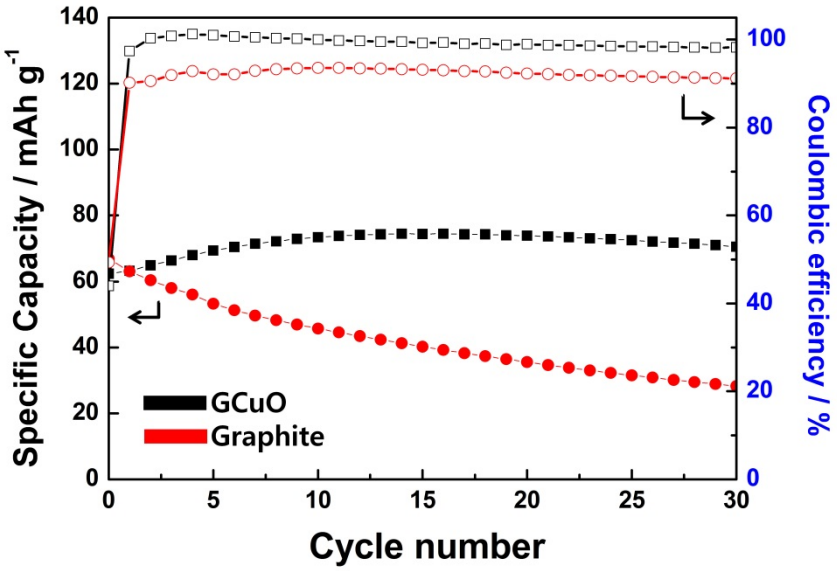

Figure 5.6 Cycling performance and columbic efficiency of graphite and GCuO 1:16 full-cells at 0.2 C

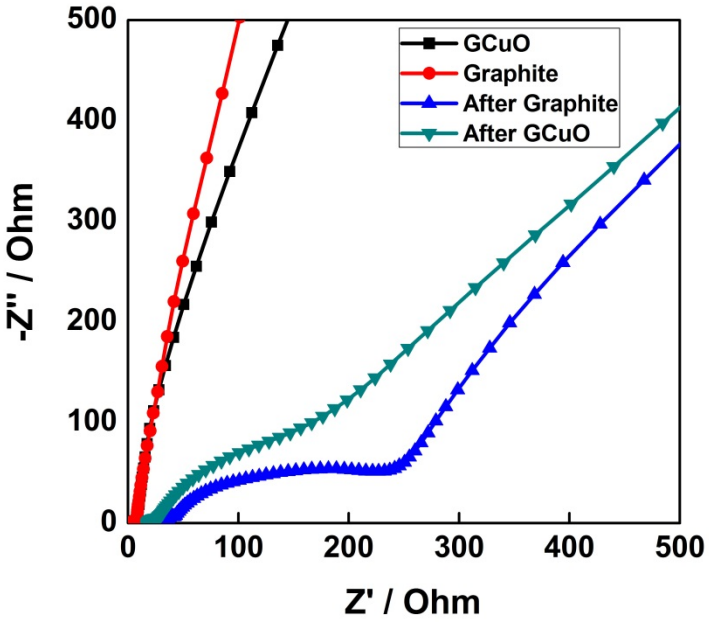

Figure 5.7 Nyquist plot analysis of GCuO and graphite full-cells. Comparison with fresh cells and after 30 charge-discharge cycles cells from 0.1 Hz to 1MHz.

5.4 Conclusion

In summary, a one-step synthesis of expanded graphite/Cu oxide nanoparticle composite (GCuO) is introduced to increase energy density and stability of lithium ion batteries. GCuO was prepared by thermal treat treatment of a Cu ion complex and graphite. In this process, gases (H_2 and CO_2) generated from the thermal decomposition of the Cu ion complex decomposition, which induced Cu oxide nanoparticle formation and graphite interlayer expansion (from 0.34 to 0.40 nm), which has good potential for effective Li or Na ion intercalation into anodes for next generation batteries. The electrochemical properties of GCuO were determined using Li ion cells. GCuO cells exhibited a high energy density (263 Wh kg^{-1}), power density (248 W/kg), discharging capacity (532 mA h g^{-1} at 0.2 C), rate retention capability (from 0.2 to 10 C), and stable long-term cycle-ability (83% capacity retention after 250 cycles). The expansion of graphite interlayer increased the stability and rate capability, because the larger interlayer distance alleviated Li ion intercalation stress during charge/discharge processes. The high energy density and discharging capacity were induced by redox reactions of Cu oxide nanoparticles. The suitability of GCuO in practical applications was studied using a full-cell

composed of GCuO and $LiFePO_4$. In this system, GCuO full-cells demonstrated high charge/discharge stability and coulombic efficiency. Based on these results, the proposed GCuO anode fabrication method will be an effective and simple approach for high-capacity LIB and SIB applications.

References

[1] Tarascon, J. M.; Armand, M. *Nature,* 2001, **414**, 359.

[2] Scrosati, B.; Hassoun, J.; Sun, Y. K. *Energ. Environ. Sci.,* 2011, **4**, 3287.

[3] Bruce, P. G.; Scrosati, B.; Tarascon, J. M. *Angew. Chem. Int. Edit.,* 2008, **47**, 2930-2946.

[4] Winter, M.; Brodd, R. J. *Chem. Rev.* 2004, **104**, 4245.

[5] Thackeray, M. M.; Wolverton, C.; Isaacs, E. D. *Energ. Environ. Sci.,* 2012, **5,** 7854.

[6] Nitta, N.; Yushin, G. *Part. Part. Syst. Char.,* 2014, **31**, 317.

[7] Derrien, G.; Hassoun, J.; Panero, S.; Scrosati, B. *Adv. Mater.,* 2007, **19**, 2336.

[8] Etacheri, V.; Marom, R.; Elazari, R.; Salitra, G.; Aurbach, D. *Energ. Environ. Sci.,* 2011, **4**, 3243.

[9] Later, M. D.; Kim, D.; Lee, E.; Johnson, C. S. *Adv. Funct. Mater.,* 2013, **23**, 947.

[10] Roberts, A. D.; Li, X.; Zhang, H. F. *Chem. Soc. Rev.,* 2014, **43**, 4341.

[11] Cao, Y. L.; Xiao, L. F.; Sushko, M. L.; Wang, W.; Schwenzer, B.; Xiao, J.; Nie, Z. M.; Saraf, L. V.; Yang, Z. G.; Liu, J. *Nano Lett.,* 2012, **12**, 3783.

[12] Lin, Y. X.; Huang, Z. H.; Yu, X. L.; Shen, W. C.; Zheng, Y. P.; Kang, F. Y. *Electrochim. Acta.,* 2014, **116**, 170.

[13] Guo, P.; Song, H. H.; Chen, X. H. *Electrochem. Commun.,* 2009, **11**, 1320.

[14] Lian, P. C.; Zhu, X. F.; Liang, S. Z.; Li, Z.; Yang, W. S.; Wang, H. H. *Electrochim. Acta,* 2010, **55**, 3909.

[15] Wen, Y.; He, K.; Zhu, Y. J.; Han, F. D.; Xu, Y. H.; Matsuda, I.; Ishii, Y.; Cumings, J.; Wang, C. S. *Nat. Commun.,* 2014, **5**, 4033.

[16] Song, T.; Xia, J. L.; Lee, J. H.; Lee, D. H.; Kwon, M. S.; Choi, J. M.;

Wu, J.; Doo, S. K.; Chang, H.; Il Park, W.; Zang, D. S.; Kim, H.; Huang, Y. G.; Hwang, K. C.; Rogers, J. A.; Paik, U. *Nano Lett.*, 2010, **10**, 1710.

[17] Stevens, D. A.; Dahn, J. R. *J. Electrochem. Soc.*, 2001, **148**, A803.

[18] Reddy, M. V.; Rao, G. V. S.; Chowdari, B. V. R. *Chem. Rev.*, 2013, **113,** 5364.

[19] Yoon, S.; Lee, S.; Kim, S.; Park, K. W.; Cho, D.; Jeong, Y. *J. Power Sources*, 2015, **279,** 495.

[20] Goriparti, S.; Miele, E.; De Angelis, F.; Di Fabrizio, E.; Zaccaria, R. P.; Capiglia, C. *J. Power Sources*, 2014, **257**, 421.

[21] Zhu, X. J.; Zhu, Y. W.; Murali, S.; Stollers, M. D.; Ruoff, R. S. *Acs Nano*, 2011, **5**, 3333.

[22] Zhang, C. F.; Peng, X.; Guo, Z. P.; Cai, C. B.; Chen, Z. X.; Wexler, D.; Li, S.; Liu, H. K. *Carbon*, 2012, **50,** 1897.

[23] Gu, D.; Li, W.; Wang, F.; Bongard, H.; Spliethoff, B.; Schmidt, W.; Weidenthaler, C.; Xia, Y. Y.; Zhao, D. Y.; Schuth, F. *Angew. Chem. Int. Edit.*, 2015, **54**, 7060.

[24] Park, H. Y.; Kim, M. S.; Bae, T. S.; Yuan, J. L.; Yu, J. S. *Langmuir*, 2016, **32**, 4415.

[25] Agostini, M.; Brutti, S.; Hassoun, J. *Acs Appl. Mater. Inter*., 2016, **8,** 10850.

[26] Arora, P.; White, R. E.; Doyle, M. *J. Electrochem. Soc.*, 1998, **145,** 3647-3667.

[27] Shin, D. H.; Woo, S.; Yem, H.; Cha, M.; Cho, S.; Kang, M.; Jeong, S.; Kim, Y.; Kang, K.; Piao, Y. *Acs. Appl. Mater. Inter.*, 2014, **6**, 3312.

[28] Cho, S.; Yin, Z.; Ahn, Y. K.; Piao, Y.; Yoo, J.; Kim, Y. S. *J. Mater. Chem. C*, 2016, **4,** 10740.

[29] Xu, K.; von Cresce, A. *J. Mater. Chem.*, 2011, **21**, 9849.

[30] Yamada, Y.; Iriyama, Y.; Abe, T.; Ogumi, Z. *Langmuir*, 2009, **25,** 12766.

[31] Funabiki, A.; Inaba, M.; Ogumi, Z. *J. Power Sources*, 1997, **68,** 227.

[32] Gopiraman, M.; Deng, D.; Babu, S. G.; Hayashi, T.; Karvembu, R.; Kim, I. S. *Acs Sustain. Chem. Eng.*, 2015, **3,** 2478.

[33] Xiang, H. F.; Li, Z. D.; Xie, K.; Jiang, J. Z.; Chen, J. J.; Lian, P. C.; Wu, J. S.; Yu, Y.; Wang, H. H. *Rsc Adv.*, 2012, **2,** 6792.

[34] Shin, K. Y.; Hong, J. Y.; Lee, S.; Jang, J. *J. Mater. Chem.*, 2012, ***22,*** 23404.

[35] Zhu, C. R.; Chao, D. L.; Sun, J.; Bacho, I. M.; Fan, Z. X.; Ng, C. F.; Xia, X. H.; Huang, H.; Zhang, H.; Shen, Z. X.; Ding, G. Q.; Fan, H. J. *Adv. Mater. Inte.*,. 2015, **2**, *1400499*.

[36] Grugeon, S.; Laruelle, S.; Herrera-Urbina, R.; Dupont, L.; Poizot, P.; Tarascon, J. M. *J. Electrochem. Soc.*, 2001, **148,** A285.

[37] Sahay, R.; Kumar, P. S.; Aravindan, V.; Sundaramurthy, J.; Ling, W. C.; Mhaisalkar, S. G.; Ramakrishna, S.; Madhavi, S. *J. Phys. Chem. C*, 2012, **116**, 18087.

[38] Jiang, J. C.; Shi, W.; Zheng, J. M.; Zuo, P. J.; Xiao, J.; Chen, X. L.; Xu, W.; Zhang, J. G. *J. Electrochem. Soc.*, 2014, **161**, A336.

Chapter 6. Conclusion

The development of new Cu-based nanomaterial synthesis is an important issue for various applications such as conductive electrode and lithium ion battery anodes. However, several limitations, such as complex manufacturing process and difficulty in synthesizing desired composition material, have hindered in the synthesis and application of Cu-based nanomaterial, and therefore research into simple and low cost synthetic method and their applications has been required in various fields. In this dissertation, the research has primarily focused on simple synthetic method and suitable application of Cu-based nanomaterial. These designed Cu-based nanomaterials achieve the remarkable electrical conductivity, oxidation-resistance, and electrochemical property, which are considered as promising high conductivity electrode and lithium ion battery anodes with high energy density and stability.

First, the Cu_3Sn alloy nanoparticles were introduced as good oxidation-resistance materials and conductive electrode using pressure-assisted fabrication method at room temperature. In particular, the Cu_3Sn nanoparticles did not show appreciable oxide impurities even when left in contact with air for 4 weeks under ambient conditions (RH 50%, 25 ^{o}C).

The electrical resistivity of the pressed Cu_3Sn nanoparticles layer also showed little change after 4 weeks. This oxidation-resistance confirmed that the Cu_3Sn nanoparticles could easily be used for electrode materials without needing any cumbersome storage conditions. In addition, the Cu_3Sn nanoparticles electrode by pressure-assisted fabrication method had suitable electrical resistivity for a conductive line. The electrical resistivity of the pressed Cu_3Sn nanoparticles electrode was 19.8 μΩ·cm at 131.3 MPa. Consequently, the pressure considerably helped connect the Cu_3Sn nanoparticles at room temperature and effectively induced low electrical resistivity in Cu_3Sn nanoparticle electrodes.

Second, novel self-reducible Cu-inks, composed by formate, alkanolamine groups, and poly alcohols, were introduced for the air sinterable fabrication of Cu electrode films. The proposed Cu-ink had a good self-reducible activity induced by the decomposition of Cu-ink ligand and the reduction assistance effect of the polyol solvents. This self-reducible ability of Cu-ink ensured the sintering of conductive Cu electrode film under air condition. To verify the reduction assistance effect of the polyol solvents, the reduction characteristics and the specific resistivity of the sintered Cu electrode films were investigated using various kinds of polyol solvent added Cu-ink. Based on the analysis of the resistivity measurements,

glycerol was confirmed to be the most suitable polyol solvent to act as a reduction assistance material. The sintered Cu electrode films made using gCu-ink were investigated as the function of the sintering temperature and glycerol content. The optimized properties of the sintered Cu electrode film made using 3 wt% gCu-ink showed a resistivity of 17 μΩ • cm at a 350 ^{o}C air sintering temperature. In addition, the potential of Cu electrode films in industrial application and for the fabrication of future devices was studied through adhesion, long-term storage, and flexibility. The adhesion tests, conducted using 3M tape peel-off, showed that the Cu electrode film made using gCu-ink with 1 wt% APTES had good adhesion properties. In the case of the storage tests, the gCu-ink revealed outstanding storage stabilities for up to 4 weeks. Furthermore, the flexibility test demonstrated that Cu electrode film made on flexible substrates had robust resistivity retention characteristics (R/R_0 <1.2) after 2000 cycles bending tests conducted using a 20 mm bending radius. On the basis of these results, the proposed novel self-reducible Cu-ink for air condition sintering is a promising material to be used in practical printing electronics.

Finally, synthesis of expanded graphite/Cu oxide nanoparticle composite (GCuO) was introduced to increase energy density and stability of lithium ion batteries. GCuO was prepared by thermal treat treatment of a Cu ion

complex and graphite. In this process, gasses (H_2 and CO_2) generated from the thermal decomposition of the Cu ion complex decomposition, which induced Cu oxide nanoparticle formation and graphite interlayer expansion (from 0.34 to 0.40 nm), which has good potential for effective Li or Na ion intercalation into anodes for next generation batteries. The electrochemical properties of GCuO were determined using Li ion cells. GCuO cells exhibited a high energy density (263 Wh kg^{-1}), discharging capacity (532 mA h g^{-1} at 0.2 C), rate retention capability (from 0.2 to 10 C), and stable long-term cycle-ability (83% capacity retention after 250 cycles). The expansion of graphite interlayer increased the stability and rate capability, because the larger interlayer distance alleviated Li ion intercalation stress during charge/discharge processes. The high energy density and discharging capacity were induced by redox reactions of Cu oxide nanoparticles. As a result, the proposed GCuO anode fabrication method is an effective and simple approach for high-capacity LIB anode.

These new designed Cu-based nanomaterials showed the simple synthesis for high conductivity electrode and enhanced performance lithium ion batteries. In addition, in the near future, the Cu-based nanomaterial development will have great potential for various academic and industrial fields.

Bibliography

1. International Publications

1) **Sanghun Cho**, Keon-Hee Lim, Si Yun Park, Zhenxing Yin, Jeeyoung Yoo, Youn Sang Kim,
"Pressure-assisted electrode fabrication using simply synthesized Cu_3Sn alloy nanoparticles",
Journal of Materials Chemistry C, **2015**, *3*, 2773-2777.

2) **Sanghun Cho**, Dong-Hun Shin, Zhenxing Yin, Chaedong Lee, Si Yun Park, Jeeyoung Yoo, Yuanzhe Piao, Youn Sang Kim,
"Synthesis of Cu_3Sn Alloy Nanocrystals through Sequential Reduction Induced by Gradual Increase of the Reaction Temperature",
Chemistry–A European Journal, **2015**, *21*, 6690-6694.

3) **Sanghun Cho**, Zhenxing Yin, Yong-keon Ahn, Yuanzhe Piao, Jeeyoung Yoo, Youn Sang Kim,
"Self-reducible copper ion complex ink for air sinter-able conductive electrodes",
Journal of Materials Chemistry C, **2016**, *4*, 10740-10746.

4) **Sanghun Cho**, Yong-keon Ahn, Zhenxing Yin, Duck-Jae You, Hyunjin Kim, Yuanzhe Piao, Jeeyoung Yoo,Youn Sang Kim
"One-step synthesis of expanded graphite/Copper oxide anodes for high capacity secondary batteries", *Submitted*

5) Dong-Hun Shin, Seunghee Woo, Hyesuk Yem, Minjeong Cha, **Sanghun Cho**, Mingyu Kang, Sooncheol Jeong, Yoonhyun Kim, Kyungtae Kang, Yuanzhe Piao,
"A self-reducible and alcohol-soluble copper-based metal–organic decomposition ink for printed electronics",
ACS applied materials & interfaces, **2014**, *6*, 3312-3319.

6) Zhenxing Yin, Chaedong Lee, **Sanghun Cho**, Jeeyoung Yoo, Yuanzhe Piao, Youn Sang Kim,
"Facile Synthesis of Oxidation-Resistant Copper Nanowires toward Solution-Processable, Flexible, Foldable, and Free-Standing Electrodes",
Small, **2014**, *10*, 5047-5052.

7) Zhenxing Yin, Seung Keun Song, Duck-Jae You, Yeongun Ko, **Sanghun Cho**, Jeeyoung Yoo, Si Yun Park, Yuanzhe Piao, Suk Tai Chang, Youn Sang Kim,
"Novel synthesis, coating, and networking of curved copper nanowires for flexible transparent conductive electrodes",
Small, **2015**, *11*, 4576-4583.

8) Yong-keon Ahn, Junwoo Park, Dalwoo Shin, **Sanghun Cho**, Si Yun Park, Hyunjin Kim, Yuanzhe Piao, Jeeyoung Yoo, Youn Sang Kim,
"Enhanced electrochemical capabilities of lithium ion batteries by structurally ideal AAO separator",
Journal of Materials Chemistry A, **2015**, *3*, 10715-10719.

9) Yong-keon Ahn, Bokyung Kim, Jieun Ko, Duck-Jea You, Zhenxing Yin, Hyunjin Kim, Dalwoo Shin, **Sanghun Cho**, Jeeyoung Yoo, Youn Sang Kim,
"All solid state flexible supercapacitors operating at 4 V with a cross-

linked polymer–ionic liquid electrolyte",
Journal of Materials Chemistry A, **2016**, *4*, 4386-4391.

10) Zhenxing Yin, Seung Keun Song, Sanghun Cho, Duck-Jae You, Suk Tai Chang, Youn Sang Kim,
"Curved Copper Nanowires-based Robust Flexible Transparent Electrodes via All-Solution Approach",
Nanoresearch, **2017**, *DOI: 10.1007/s12274-017-1523-5*.

11) Duck-Jae You, Zhenxing Yin, Yong-keon Ahn, Sanghun Cho, Hyunjin Kim, Jeeyoung Yoo, Dalwoo Shin, Youn Sang Kim,
"A High-Performance Polymer Composite Electrolyte Embedded with Ionic Liquid for All Solid Li-Batteries Operating at Ambient Temperature",
Journal of Industrial and Engineering Chemistry, accepted

12) Zhenxing Yin, Seung Keun Song, Sanghun Cho, Duck-Jae You, Suk Tai Chang, Youn Sang Kim,
""Copper Nanowire/Multi-Walled CNT Composites as All-Nanowire Electrode for Fast Charging/discharging Lithium-Ion Battery",
Nanoresearch, under review.

2. International Conference

1) **Sanghun Choi**, Zhenxig Yin, Youn Sang Kim,
"Cu-Sn nanocrystals formation mechanism analysis and synthesis using a hot injection method", *Oral presentation*
2013 E-MRS fall meeting, Warsaw, Poland, September 16-20, 2015.

2) **Sanghun Cho**, Keon-Hee Lim, Jeeyoung Yoo, Youn Sang Kim
"Oxidative stable Cu_3Sn nanoparticles for Novel electrode fabrication using pressure under ambient condition",
2014 ECS and SMEQ Joint international meeting, The electrochemical Society, Cancun, Mexico, October 5-9, 2014.

3) **Sanghun Cho**, Jeeyoung Yoo, Yong-keon Ahn, Duk-jae Yoo, Sungyun Chung, Youn Sang Kim
"Exfoliated Graphite and Copper oxide hybrid anode for high capacity and stable Li ion battery", *Oral presentation*
PRiME 2016, The electrochemical Society, Honolulu, Hawaii, USA, October 2-7, 2016.

4) Zhenxing Yin**,** **Sanghun Cho**, Jeeyoung Yoo, Soo Jeong Lee, Jae Min Myung, Youn Sang Kim
"Synthesis of Oxidation-Free Copper Nanowires toward Solution-processed Flexible and Foldable Electrodes",
World Innovation Conference & Expo, Tech Connect, Washington DC, USA, June 15-18, 2014.

5) Zhenxing Yin, **Sanghun Cho,** Jeeyoung Yoo, Youn Sang Kim, Jae Min Myung
"Synthesis of oxidation stable Cu nanowires with high performances for future electrodes",
247th American Chemical Society National Meeting & Exposition, American Chemical Society, Dallas, Texas, USA, March 16-20, 2014.

6) Zhenxing Yin, Sanghun Cho, Jieun Ko, Sung Yun Chung, Youn Sang Kim

"Synthesis of High Conductive and Oxidation-Free Copper Nanowires for Flexible and Foldable Electrodes",
2014 MRS spring meeting & exhibit, Material research society, San Francisco, California, USA, April 21-25, 2014.

7) Jeeyoung Yoo, Yong Keon Ahn, Si Yun Park, **Sanghun Cho,** Youn Sang Kim
"Characteristics of Anodic Aluminum Oxide as Separator for Li Ion Battery",
2014 ECS and SMEQ Joint international meeting, The electrochemical Society, Cancun, Mexico, October 5-9, 2014.

8) Zhenxing Yin, **Sanghun Cho**, Dukjae You, Youg-keon Ahn, Youngjun Yang, Jeeyoung Yoo, Youn Sang Kim*
"Fabrication of flexible transparent conductive electrode using curved copper nanowires",
2015 International Chemical Congress of Pacific Basin Societies, PacificChem, Honolulu, Hawaii, USA, December 15-20, 2015.

9) Jeeyoung Yoo, Hyunjin Kim, Dukjae You, Bokeong Kim, Youg-keon Ahn, **Sanghun Cho**, Zhenxing Yin, Youn Sang Kim
"4V operating voltage, flexible quasi solid state electrolyte with EMITFSI/cross-linked P4VPh/aramid composite for supercapacitor",
2015 International Chemical Congress of Pacific Basin Societies, PacificChem, Honolulu, Hawaii, USA, December 15-20, 2015.

10) Youg-keon Ahn, Youngjun Yang, Zhenxing Yin, Hyunjin Kim, **Sanghun Cho**, Jeeyoung Yoo, Youn Sang Kim
"Study of structural effects via anodic aluminum oxide as a novel inorganic separator for lithium ion batteries.",

2015 International Chemical Congress of Pacific Basin Societies, PacificChem, Honolulu, Hawaii, USA, December 15-20, 2015.

11) Duck-Jae You, Jeeyoung Yoo, Yong-keon Ahn, **Sanghun Cho**, Sung Yun Chung, Youn Sang Kim
"Solid Polymer Electrolyte Embedded with Ionic Liquid for Lithium-Ion Battery Operating at Ambient Temperature",
PRiME 2016, The electrochemical Society, Honolulu, Hawaii, USA, October 2-7, 2016.

12) Yong-keon Ahn, Ji-Sang Yu, Sang-Gil Woo, Jeeyoung Yoo, **Sanghun Cho**, Duck-Jae You, Youn Sang Kim, Ki Jae Kim
"The Composite of Aluminum Oxide/Pvdf-HFP Membrane for Advanced Li-S Batteries",
PRiME 2016, The electrochemical Society, Honolulu, Hawaii, USA, October 2-7, 2016.

3. Domestic Conferences

1) **Sanghun Cho**, Zhenxing Yin, Si Yun Park, Youn Sang Kim
"New Intermetallic phase Cu/Sn nanoparticles characteristic analysis and synthesis using a hot injection method",
2013, Spring KSIEC Meeting, The Korean Society of Industrial and Engineering Chemistry, Jeju, Korea, May 1-3, 2013.

2) **Sanghun Cho**, Youn Sang Kim,
"Air sinter-able Cu electrode fabrication by self-reducible Cu ion complex ink and polyol solvent",

2016, Spring KSIEC Meeting, The Korean Society of Industrial and Engineering Chemistry, Yeosu, Korea, May 2-4, 2016.

4. Patents

1) 김연상, **조상훈**, 윤진성, “공기중 열처리가 가능한 금속 유기 전구체 및 다가 알코올을 포함하는 전도성 잉크 조성물 및 이를 이용한 금속배선 형성방법”, 출원번호: 10-2016-0053914.

2) 김연상, 윤진성, **조상훈,** “구리 나노선의 합성방법”, 출원번호: 10-2014-0029879. (등록)

3) 김연상, 윤진성, **조상훈,** 유덕재, “휘어진 구리 나노선의 합성방법”, 출원번호: 10-2015-0018622. (등록)

국 문 초 록

지난 반세기동안 나노재료의 조성, 크기, 구조의 제어에 대한 많은 연구가 진행되고 있다. 특히 구리 기반 나노 물질은 우수한 전기적, 물리적, 화학적, 광학적 성질을 가진 물질로서 많은 연구가 진행되었다. 최근에는 고전도도의 전극과 고성능의 리튬이온 배터리에 효율적인 응용을 위해 구리 기반 나노 물질에 대한 연구가 많은 관심을 받고 있다. 그러나 현재 사용되는 구리 기반 나노 물질들은 합성의 복잡성, 구리 특유의 산화특성, 구조적 한계로 인하여 다양한 활용에 대한 요구를 충족시키지 못하고 있다. 따라서 이를 해결하기 위해 단순한 합성법 과 높은 산화 안정성, 용량, 안정성을 가진 구리 기반 나노 물질에 대한 개발이 요구된다.

본 학위 논문에서는 구리를 기반으로 한 나노재료를 간편하게 제조하고 이를 고전도성 전극과 이차전지 음극재에 응용하는 연구에 대해 기술하였다. 첫째로, 구리 - 주석 이종금속 나노입자를 한 번의 공정으로 합성할 수 있는 방법을 개발하고 실온에서 고전도성의 전극을 만들 수 있는 방법을 제안하였다. 실제로 합성된 물질은 4주간의 산화 안정성 테스트에서 높은 전도도 (20 $\mu\Omega$• cm) 와 고유의 결정 구조를 유지하였다.

두번째로, 구리 이온 복합체와 다가 알코올의 혼합물을 이용하여 공기중에서도 소성이 가능한 고전도성의 전극을 형성할 수 있는 방법을 개발하였다. 이는 구리 이온 복합체가 분해 할 때 나오는 수소 가스와 다가 알코올의 환원 특성이 복합적으로 작용하여 나타나는 현상으로서 낮은 비저항 (17 $\mu\Omega$• cm) 이 나오는 것을 확인하였다.

마지막으로, 산화 구리 나노 입자와 층간 간격이 넓어진 흑연의 합성법을 개발하였다. 구리 이온 복합체와 흑연의 열처리로서 얻을 수 있었다. 이러한 층간 간격이 넓어진 흑연과 산화 구리 나노 입자는 배터리 충방전시 안정성과 높은 용량 나타내었다.

다양한 방법을 통해 구리를 기반으로한 나노재료의 합성으로 이를 고전도성 전극과 리튬 이차전지 전극재로 적용하였을 때 기존 대비 저렴하고 단순한 방법으로 성능 향상을 확인할 수 있었다.

주요어: 구리 기반 나노물질, 구리 합금, 산화 구리, 나노물질 합성, 전도성 전극, 리튬이온 배터리 음극.

학 번: 2012-22452